Neutrino beam simulations of an extended target in T2K and neutrino interactions in BabyMIND

Lai Hin Lam

Submitted in fulfilment of the requirements for the
Degree of Master by Research

School of Physics and Astronomy
College of Science and Engineering
University of Glasgow

September 2022

Abstract

This thesis describes two independent studies performed in the context of the T2K neutrino oscillation experiment: a simulated study of an upgraded extended target for the T2K neutrino beam, and a study of neutrino interactions in the BabyMIND near detector in T2K. In the first study, a simulation of a potential upgrade to the T2K secondary beamline by inserting an extra target at the downstream end of the first magnetic horn was carried out. Different choices of materials are tested with density modification on some of the materials. Simulated results show that titanium provides the best improvement to the ratio of right-sign and wrong-sign neutrino fluxes, but other material properties suggest that silicon carbide is the optimal material out of all the tested materials. Results also show that the materials used on the support structure for the extra target should be minimized.

Another study performed in this thesis is the Monte-Carlo simulation of muon neutrino interactions inside BabyMIND. The momenta of the muons from the simulated results are reconstructed by measuring the range of the muons using the Bethe-Bloch formula. A migration matrix is extracted from the correlation between true and reconstructed muon momenta. An unfolding method based on Bayes' theorem is used, in combination with the extracted migration matrix, to extract the momenta from data collected during run 10 and run 11 of the T2K experiment, to measure the ratio of antineutrinos to neutrinos observed in the forward-horn-current configuration of T2K. The reconstruction of the data and the unfolding of the data gives the wrong-sign ratios of 3.73% and 3.86% respectively between 0 and 2000 $\mathrm{MeV/c}$.

Contents

List of Tables

List of Figures

Acknowledgements

I would like to thank my supervisor Paul Soler, Phillip Litchfield and fellow researcher John Nugent for helping on the code modifications, providing insights on the physics involved in this thesis and the feedback on the writing of this thesis.

Declaration

With the exception of chapters 1 and 2, which contain introductory material, all work in this thesis was carried out by the author unless otherwise explicitly stated.

Chapter 1

Introduction and Theory

1.1 Introduction

Discovery of Beyond Standard Model (BSM) physics has been one of the main goals in modern particle physics, and neutrino physics is one of the aspects in particle physics that could show evidence for BSM physics. As a result, properties of the neutrino and its interaction with other particles are currently under study. This thesis aims to simulate the T2K neutrino beam with an extended graphite target and to measure neutrino interactions in iron in the Baby Magnetized Iron Neutrino Detector (BabyMIND) at the Tokai-to-Kamioka (T2K) experiment.

BabyMIND is a magnetized detector that is installed behind the WAter Grid And SCIntillator (WAGASCI) detector at JPARC, the Japanese Proton Accelerator Research Centre in Tokai (Japan), and it aims to measure the charge and momentum of charged particles generated from neutrino interactions, either in WAGASCI or BabyMIND itself. The BabyMIND is composed of alternating scintillator plates and magnetized iron plates, that allows to track muons, from charged current neutrino interactions, passing through BabyMIND to be bent by the horizontal magnetic field. Through the magnetic field generated inside BabyMIND by coils around the iron plates, particles with positive or negative charge will bend either upward or downward, due to the Lorentz force,

$$\vec{F} = q\vec{v} \times \vec{B}, \tag{1.1}$$

where $\vec{v}$ is the velocity of the particle, q its charge and $\vec{B}$ the magnetic field, which is oriented horizontally. Thus, this can be used to determine the charge and momentum of the particle. The momentum can be determined by measuring the range of the particle in the detector, but also by measuring its radius of curvature R, and using:

$$p = qBR. \tag{1.2}$$

Since the curvature of the bent tracks can be used to determine the charge and momentum of the particle, analyzing the muons recorded can give us information about the energy of the

neutrino, investigating the kinematics of the neutrino interaction, to perform a measurement of neutrino scattering as a function of neutrino energy.

The main near detector of T2K is ND280 (Near Detector at 280 m), located on a different location with respect to WAGASCI-BabyMIND, and thus the two detectors have different off-axis angles that affect the mean energy of the neutrino flux passing through each of these two detectors. The ND280 detector is located at a 2.5 degree off-axis angle from the beam, whilst WAGASCI-BabyMIND has a 1.5 degree off-axis angle. As a result, the mean energy of the beam passing ND280 is $\sim$600 MeV and the mean energy of the neutrino beam passing WAGASCI-BabyMIND is $\sim$800 MeV.

This thesis will also include simulations of neutrinos from the beam at 280 m, the distance that the ND280 and WAGASCI-BabyMIND detectors are located from the beam source, at off-axis angles of 2.5 and 1.5 degrees respectively, to mimic the settings of ND280 and WAGASCI-BabyMIND as much as possible. A comparison of the ND280 simulations to the official T2K simulations of the ND280 flux will allow to benchmark the simulation programme, and will allow to validate the new results at WAGASCI-BabyMIND.

Another simulation that will be included in this thesis is the simulation of the graphite neutrino target inside the first beam horn at the upstream section of the T2K neutrino beam. As there is a desire to upgrade the whole system of T2K in order to improve the production of neutrino interaction and neutrino oscillation research, one direction of the desired upgrade is the beam generation. There is interest on modifying the target region and the first beam horn in order to reduce the wrong-sign contamination of beam generation in T2K, thus improving the accuracy of the system. This thesis also reports simulations of modifications to the T2K target inside the first horn, in order to determine the potential benefits of such modifications for future upgrades to the T2K neutrino target and horn system.

1.2 Standard Model

The Standard Model is a model that combines the electromagnetic, strong nuclear and weak nuclear forces, and has successfully predicted most of the experimental results in particle physics, since its publication. The neutrino is a fundamental particle, constructed by the Standard Model to have zero particle mass, neutral charge and has a left-handed helicity. Although there is a large number of neutrinos existing in the universe (the second most abundant particle in the universe after the photon), neutrinos only interact through weak interactions and gravity, causing them to be difficult to detect. While the Standard Model accomodates the existence of all the particles observed so far, such as quarks, leptons, gauge bosons and the Higgs particle, there are a few important contradictions between the Standard Model and experimental data. As a result, a model beyond the Standard Model must exist in order to explain such contradictions, hence different studies on beyond the Standard Model and experiments, such as the T2K experiment,

aim to investigate these contradictions.

1.2.1 Quantum Field Theory (QFT)

Quantum Field Theory (QFT) is the theory that best explains microscopical physics to date. It is a unification of classical field theory and quantum mechanics. While classical field theory describes the dynamics of different types of fields, and is able to describe relativistic particles, the classical field theory is not compatible with objects at an atomic scale, where properties such as quantized energy, uncertainty principle and particles as wave functions are now necessary to be taken into consideration. QFT is a theory that unifies relativistic classical field theory and quantum mechanics, to provide explanations of the different interactions between different particles, interactions between particles and fields, and also the different properties of particles at this quantum scale. While QFT fails to include general relativity, which is significant only with massive objects, and thus fails to explain the gravitational forces within the same framework as the other three basic forces in the universe, it is currently the best theory that unifies electromagnetism, the weak nuclear force and the strong nuclear force.

Instead of expressing potential energy V and the kinetic energy T of a given system or object separately, the energy can be express in terms of the Lagrangian L, defined as follows,

$$L = T - V. \tag{1.3}$$

In general, for any given Lagrangian L, there exists a Lagrangian density $\mathscr{L}$ that, when integrating the Lagrangian density over all volume, gives back the Lagrangian itself,

$$L = \int d^3x \mathscr{L} \tag{1.4}$$

and if the Lagrangian density is integrated not only over space, but also over a specific time period, the integrated value over space-time is defined as an action S. For a field ϕ and its first derivative $\partial_\mu \phi$ that forms a Lagrangian density, the change of the density over the four-dimensional space-time is as follows,

$$S \equiv \int d^4x \mathscr{L}(\phi, \partial_\mu \phi). \tag{1.5}$$

The integration of the Lagrangian density over space-time results in a scalar. A visualization of the action between two space-time points could be different curves that connect two positions on the field, and the field moves from one position to another one over a specific period of time. While there are possibly an infinite number of paths for such an action, the principle of least action must be obeyed in order to obtain a physically possible situation. Such a condition leads to the field equation of motion.

The principle of least action states that for small variations of action between two positions

q_1 and q_2, whilst there is an infinite number of curves connecting the two positions, only the curve with the least action is physically preferred. In other words, if we specify the curve with the least action to be $S(t)$, then a curve with small variation with respect to $S(t)$ is $S'(t)$ and will have the following expression:

$$S'(t) = S(t) + \delta S(t). \tag{1.6}$$

To minimize the action, $\delta S(t)$ should vanish. As a result,

$$\delta S(t) = \int d^4x \delta \mathscr{L} = \int d^4x \left(\frac{\partial \mathscr{L}}{\partial \phi} \delta\phi + \frac{\partial \mathscr{L}}{\partial(\partial_\mu \phi)} \delta(\partial_\mu \phi) \right) = 0 \tag{1.7}$$

and after integration by parts and simplification,

$$\delta S(t) = \int d^4x \left(\frac{\partial \mathscr{L}}{\partial \phi} - \partial_\mu \frac{\partial \mathscr{L}}{\partial(\partial_\mu \phi)} \right) \delta\phi = 0 \tag{1.8}$$

and thus, the Euler-Lagrange equation for the fields is obtained,

$$\frac{\partial \mathscr{L}}{\partial \phi} - \partial_\mu \frac{\partial \mathscr{L}}{\partial(\partial_\mu \dot{\phi})} = 0. \tag{1.9}$$

The Euler-Lagrange equation describes the geodesic flow of the field, which means the Euler-Lagrange equation is a representation of the flow, and the dynamics of the field physically. As a result, the fundamental idea for QFT is to determine the proper Lagrangian density, which then can be used to determine the equation of motion and therefore understand quantum interactions and particles. As the above equations describe fields, it is possible now to incorporate electromagnetic interactions and quantum mechanics in order to obtain the key features leading to the Standard Model, where the neutrino, the focus of this thesis, is constructed. To incorporate these areas into field theories, the idea of gauge theory, Lie group and symmetry has to be introduced.

1.2.2 Particle and forces

To understand different particles and forces in the Standard Model, the study of Lie groups and gauge theories is necessary. Symmetry is crucial to understand field theories, as the existence of any symmetry immediately imposes a specific type of conservation law. Continuous symmetries can be expressed as special matrix groups called Lie groups. The Lie group is also a differential manifold that maps the Euclidian space. The reason Lie groups are important is that it is a representation of symmetries, which means that it also represents different conservation laws [1]. Lie groups can be expressed with matrix notations with a form of $LG(n)$, where LG can be different notations describing the specialty of this group, and n is the dimension of the matrix in this Lie group. For example, $SU(2)$ represents a special (S) unitary (U) matrix, showing that the

matrix that represents the group has a determinant of 1 (special), has the property $U^\dagger U = UU^\dagger = I$ (unitary), and has a dimension of 2×2. When a Lagrangian undergoes a transform under one of these Lie groups, it is defined as undergoing a gauge transformation. Gauge theories describe such transformations. The gauge theory, when quantized, creates gauge bosons, which mathematically form some of the familiar particles in the Standard Model.

One of the main gauge theories in QFT is quantum electrodynamics (QED), with a Lie group of $U(1)$. QED is a quantum version of electromagnetism that is Abelian, that is, meaning that the order of the elements inside the Lie group $U(1)$ are position-invariant when doing operations between such elements. The gauge boson of QED is the photon which mediates the electromagnetic forces. QED provides the mechanism to calculate phenomena such as Compton scattering or the probability amplitude of electrons and positrons in an electromagnetic interaction. However, QED is often combined with another gauge theory with a Lie group of $SU(2)$ that represents the weak interaction via a Yang-Mills theory. The result is a $SU(2) \times U(1)$ gauge group that merges the two interactions together to form the electroweak interaction. This new group produces a total of four gauge bosons by spontaneous symmetry breaking. On top of the photons from the QED gauge group, the vector bosons W^+, W^- and Z^0 are also produced from the $SU(2)$ group that mediates the weak force. The electroweak interaction couples to the weak charges and weak isospins of fermions, which when combined create charges in particles. It also describes all known interactions of leptons. Here we denote the Lagragian density of the electroweak force as $\mathscr{L}_{EW}$.

Another gauge theory in QFT is quantum chromodynamics (QCD) that is a $SU(3)$ non-Abelian Lie group. QCD is the theory of strong interactions between quarks and gluons, the mediators of the strong force. It describes properties for particles such as their colour and their chirality. Colour is a concept introduced to match the charge from electroweak interactions. The colour is introduced to define a local symmetry, creating the $SU(3)$ group through a Yang-Mills theory. The gauge bosons for QCD are the gluons, responsible for mediating the strong nuclear forces. Gluons also contain the colour charge, so they can interact with each other and with quarks, which explains the short range of the strong force, and the fact that only colour-neutral combinations of quarks and antiquarks (mesons) or three quarks and three antiquarks (baryons) exist as stable configurations. Here we denote the QCD Lagrangian density as $\mathscr{L}_{QCD}$.

Chirality is a concept used to determine the relationship between the spin of a particle and its momentum. When the spin of the particle has the same direction compared to the direction of motion, then the particle is right-handed. On the other hand, if the two directions are opposite to each other, the particle is said to be left-handed. This handedness, or helicity, is not exactly the same as chirality as helicity can vary with different reference frames. However, they are equivalent in massless particles and in most cases they are related. This chirality introduces a symmetry called parity. The $SU(2)$ Lie group that represents the electroweak interaction only affects left-handed particles. It has been found that parity is conserved in electromagnetic and

strong interactions, but it is violated in the weak interactions.

The Higgs mechanism is another crucial part of the Standard Model that explains the mass of different particles. When the Higgs field interacts with the $SU(2) \times U(1)$ group, it spontaneously breaks the symmetry, giving masses for the W and Z bosons, undergoing the Higgs mechanism. Since the electromagnetic field does not interact with the Higgs field, photons are massless. For the fermions, the interaction between the Higgs field and fermions also breaks the spontaneous symmetry of the fermion fields, providing fermions with different masses. This is known as the Yukawa interaction and provides fermions with mass. As a result, there should be an extra term for the Lagrangian including this Yukawa interaction. The Lagrangian density of the Higgs field, and the Yukawa interaction are denoted as $\mathscr{L}_{Higgs} + \mathscr{L}_{Yukawa}$.

The Standard Model is the combination of the gauge theories above. When adding the Lagrangian densities introduced previously together, the Lagrangian for the Standard Model is obtained:

$$\mathscr{L}_{SM} = \mathscr{L}_{QCD} + \mathscr{L}_{EW} + \mathscr{L}_{Higgs} + \mathscr{L}_{Yukawa} \tag{1.10}$$

The Standard Model unifies the electromagnetic, weak and strong nuclear fields together to provide a mostly accurate theoretical framework for the microscopic part of physics. As a result, the Standard Model belongs to the $SU(3) \times SU(2)_L \times U(1)$ Lie group. Figure 1.1 shows every fundamental particle constructed by the Standard Model, except for the Higgs. The up, down, charm, strange, top and bottom quarks undergo strong interactions. These quarks, when combined together, form different new baryons, which are fermions such as protons (up, up, down) and neutrons (up, down, down) or mesons, which are bosons such as the charged pions (up, anti-down or anti-up, down). There are three pairs of leptons, the negatively charged lepton, and their corresponding neutrinos with no charges. For each fermion in the model, there also exists a corresponding antiparticle that has the opposite charge. In this thesis, we will study muon-neutrino interactions with nucleons that produce muons in the target detector. The electroweak theory predicts that interacting neutrinos should always have a left-handed chirality, and the opposite for antineutrinos. The theory also postulates that the neutrinos have zero mass.

While electromagnetic, weak and strong forces are explained and included in QFT, the last of the four basic forces, gravity, has not been included in QFT since the effect of gravity is negligible at the atomic scale. While general relativity explains gravity with the concept of test masses following the curvature of spacetime created by massive objects, there lacks an established connection between QFT and general relativity. Since the four basic forces coexist in the universe, there must be a model, beyond the Standard Model, that can unify QFT and general relativity. In order to find such model, it is desirable to investigate phenomena that the Standard Model failed to explain within the model. Two of such phenomena is neutrino oscillation and charge-parity (CP) violation.

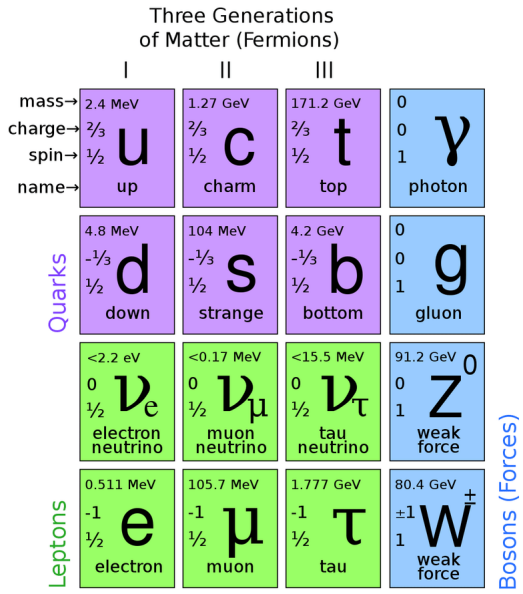

Figure 1.1: A demonstration of the Standard Model and all the fundamental particles predicted (except for the Higgs particle), with masses, charges and spins included [2].

1.2.3 Charge, Parity and Charge-Parity (CP) symmetry

The idea of charge conjugation symmetry is brought up by electromagnetism, where the theory should be invariant to particles having opposite charge such as electromagnetic interactions being the same for electrons and positrons, with negative and positive electric charge respectively. The idea of parity symmetry comes from simple classical physics, if the sign of all spatial coordinate are changed, the same rules of physics should be obeyed. These symmetries, and the combination of the two, the charge-parity conversion holds true for all interactions except weak interactions.

Charge and parity in electromagnetic and strong interactions are conserved. A parity transformation can be seen as a change in spatial coordinates, which implies a change in the helicity of the particle (the direction of the spin vector changes with respect to the direction of motion), so the particle changes from left-handed to right-handed helicity or vice-versa. The amount of matter and anti-matter in the universe may be related to the effect of charge and parity (CP) transformations not being conserved in weak interactions, as was discussed by Sakharov [3]. However, observation shows that the abundance of matter is higher than antimatter, which suggests that there is some asymmetry in the universe.

In order to study such asymmetry, Lee and Yang postulated that parity is not conserved in weak interactions [4]. One experiment about beta decay on polarized Cobalt-60 [5] in 1957 showed that weak interactions do not conserve the parity symmetry. When the polarized Cobalt-60 undergoes beta decay, it is expected, if parity symmetry were true in all cases, that the directions of the emitted electrons with respect to the direction of the polarized nucleus should be symmetric. However, the experiment showed that the beta particles from the beta decay

favoured the direction that is opposite to the spin of the polarized nucleus. This means that the parity transformation is not invariant when weak interactions are applied. However, the question still remained on the overall conservation of charge conjugation and parity transformation (CP).

In 1964, an experiment about kaon decay showed that weak interactions may not obey CP conservation [6]. This experiment showed that neutral kaons decayed after a long distance (K_L) to two-pions (even parity) with a fraction of $\sim 2 \times 10^{-3}$, when it was expected that they should only decay to three pions (odd parity). While the amount of two-pion decay is small (45 out of 22700) it implies that there must be CP violation. While CP violation is proven by this experiment, there are more experiments trying to discover more about CP violation in different scenarios.

1.3 Neutrinos

1.3.1 Neutrinos, postulation and discovery

Neutrinos were first postulated by Pauli to conserve energy, momentum and angular momentum in beta decay. Pauli postulated a neutral charged, massless particles that is emitted from the nucleon when undergoing beta decay [7]. The neutrino was first discovered in the Cowan-Reines experiment in 1956, where antineutrinos were produced from beta decay inside a nuclear reactor. The antineutrinos then interact with protons to generate positrons that annihilate with electrons to create gamma rays that are detectable [8]. To this date, detecting the product of neutrino interactions is still the method to detect and study neutrinos, due to the extremely small mass and neutral charge of the neutrino.

Muon neutrinos were discovered soon after the electron neutrino in 1962, by generating a muon-neutrino beam from pion decay and shooting the neutrino beam through a 13.5 m iron wall [9]. The muons were then detected in an aluminium spark chamber behind the iron wall. Most of the main ideas used in this experiment are still used in modern muon neutrino experiments. The idea of generating muon neutrinos from pion decay and using iron as an absorber to filter out everything else are both used in the T2K experiment, especially the near detectors.

The tau neutrino was discovered in 2000, by the DONUT experiment in Fermilab [10]. The tau-neutrino beam was generated using a 800 GeV proton beam generated by the Tevatron accelerator interacting with a Tungsten dump, through the decay of strange D_s mesons to tau and tau antineutrinos. The taus then decay again into tau neutrinos. Four events out of 203 events met the criteria of tau decays without any extra leptons, which was enough to supply evidence for the discovery of the tau neutrino.

As mentioned previously, neutrinos always have a left-handed chirality and the antineutrinos have right-handed chirality. Neutrinos have leptonic flavors of electron, muon and tau, each being the corresponding pair to the electron, muon and tau neutrinos. They all have neutral

charge and have a spin of $\frac{1}{2}$. Although it was postulated in the Standard Model that neutrinos are massless, experimental results show otherwise. It is currently determined that neutrinos may be the only possible Majorana particles since it is not known if the neutrino is its own antiparticle. Since the neutrino and antineutrino are both neutral, it is not possible to identify whether the neutrino and antineutrino are distinguishable, only based on neutrino interactions. The most promising way of determining the Majorana nature of the neutrino is by the possible observation of neutrinoless double beta decay [11]. No evidence for this process has been obtained so far.

The mass of the neutrino is non-zero, as shown by neutrino oscillation experiments (see section 1.3.2), which demonstrate neutrino mixing that can only occur if neutrinos have mass. The existence of a non-zero neutrino mass is evidence that suggested the Standard Model is flawed. Neutrino oscillation experiments only give the difference between neutrino masses but not the absolute value of their masses. Current research conducted by the KATRIN experiment has set an upper limit on the electron neutrino mass of 0.8 eV, with 90% confidence level [12].

1.3.2 Neutrino oscillation

While the Standard Model predicted that the neutrino has no mass, the existence of neutrino oscillation proves otherwise. The idea of neutrino oscillation was introduced by B. Pontecorvo in 1957 [13]. It is predicted that the mass eigenstate of the neutrino $|\nu_i\rangle$ $(i = 1,2,3)$ and the flavor eigenstate $|\nu_\alpha\rangle$ $(\alpha = e,\mu,\tau)$ are different. Maki, Nakagawa and Sakata [14] then proposed the idea of neutrino mixing, stating that a mass eigenstate of neutrino can be expressed as the mixture of multiple flavor eigenstates. In a simpler case where only two mass and two flavor eigenstates are involved, the linear combination is as follows:

$$\begin{aligned} \nu_e &= \cos\theta\nu_1 - \sin\theta\nu_2, \\ \nu_\mu &= \sin\theta\nu_1 + \cos\theta\nu_2. \end{aligned} \tag{1.11}$$

As shown in Eqn. 1.11, a flavor eigenstate is a mixture of the two mass eigenstates, each having a trigonometric term in front. The angle θ is therefore named the mixing angle. Moreover, if neutrinos are massless as stated in the Standard Model, then the states ν_1 and ν_2 are indistinguishable and there is no need for the mixing in Eqn. 1.11. As a result, for neutrino mixing to exist, neutrinos must have a mass, violating the Standard Model. In a more complex and realistic case, where there are three masses and three flavor eigenstates, the relationship between mass and flavor engenstates is as follow [15, 16]:

$$|\nu_i\rangle = \sum_{i=1}^{3} U_{\alpha i}^{*} |\nu_\alpha\rangle. \tag{1.12}$$

The $U_{\alpha i}$ in the equation is a component of the matrix U, the Pontecorvo-Maki-Nakagawa-Sakata (PMNS) matrix. The PMNS matrix is a modern parametrization of the relationship proposed by

Maki, Nakagawa and Sakata [15, 14, 16], which has the following form:

$$
\begin{aligned}
U &= \begin{pmatrix} U_{e1} & U_{e2} & U_{e3} \\ U_{\mu 1} & U_{\mu 2} & U_{\mu 3} \\ U_{\tau 1} & U_{\tau 2} & U_{\tau 3} \end{pmatrix} \\
&= \begin{pmatrix} 1 & 0 & 0 \\ 0 & c_{23} & s_{23} \\ 0 & -s_{23} & c_{23} \end{pmatrix} \begin{pmatrix} c_{13} & 0 & s_{13}e^{-i\delta_{CP}} \\ 0 & 1 & 0 \\ -s_{13}e^{i\delta_{CP}} & 0 & c_{13} \end{pmatrix} \begin{pmatrix} c_{12} & s_{12} & 0 \\ -s_{12} & c_{12} & 0 \\ 0 & 0 & 1 \end{pmatrix} \begin{pmatrix} 1 & 0 & 0 \\ 0 & e^{i\alpha_{21}/2} & 0 \\ 0 & 0 & e^{i\alpha_{31}/2} \end{pmatrix}.
\end{aligned}
\tag{1.13}
$$

Here the notation s_{ij} and c_{ij} represents $\sin\theta_{ij}$ and $\cos\theta_{ij}$ respectively, and δ_{CP} represents the Dirac CP-violation phase that goes to 0 when there is no CP-violation. The last matrix multiplication with a component of α_{ij} is the Majorana term, where the α_{ij} is non-zero only if the neutrino is a Majorana particle, having the anti-particle the same as the particle itself. Now let us consider the time evolution of the mass eigenstate of the neutrino:

$$|\nu_i(t)\rangle = e^{i(p_i x - E_i t)}|\nu_i(0)\rangle. \tag{1.14}$$

Thus for a neutrino state of flavor α:

$$|\nu_\alpha(t)\rangle = \sum_i U_{\alpha i} e^{i(p_i x - E_i t)}|\nu_i(0)\rangle. \tag{1.15}$$

A neutrino that originates with flavor α that oscillates into flavor β from time 0 to time t has a time-dependent probability amplitude:

$$A(\nu_\alpha \to \nu_\beta) = \langle \nu_\beta | \nu_\alpha(t)\rangle. \tag{1.16}$$

Since, as shown above in Eqn. 1.12, the flavor eigenstate is the superposition of all the mass eigenstates multiplying the corresponding components in PMNS matrix, the above equation can be expanded as:

$$
\begin{aligned}
A(\nu_\alpha \to \nu_\beta) &= \sum_j \sum_i U^*_{\beta j} U_{\alpha i} e^{i(p_i x - E_i t)} \langle \nu_j | \nu_i \rangle \\
&= \sum_i U_{\alpha i} U^*_{\beta i} e^{i(p_i x - E_i t)}.
\end{aligned}
\tag{1.17}
$$

To further simplify Eqn. 1.17, a few assumptions are made. If assuming the fact that the energy E of the neutrino is significantly higher than the mass, the momentum of a neutrino in a specific eigenstate can be expressed as follows:

$$p_i = \sqrt{E^2 - m_i^2} \approx E - \frac{m_i^2}{2E}. \tag{1.18}$$

A further assumption is made that $x = t \simeq L$ can be made using natural units, which helps Eqn. 1.17 to share a similar form with a classical oscillation. Assuming energies in different mass eigenstates are the same, when the neutrino has travelled for a distance L, effectively travelling from a node of oscillation to another, Eqn. 1.17 can then be expressed as:

$$A(\nu_\alpha \to \nu_\beta)(L) = \sum_i U_{\alpha i} U^*_{\beta i} e^{-i\frac{m_i^2 L}{2E}}. \tag{1.19}$$

As a result, the probability of the transition $\nu_\alpha \to \nu_\beta$, which is the square of $A(\nu_\alpha \to \nu_\beta)$, can be expressed as [14, 16]:

$$P(\nu_\alpha \to \nu_\beta)(L) = \sum_{i,j} U_{\alpha i} U^*_{\beta i} U^*_{\alpha j} U_{\beta j} e^{\frac{\Delta m^2_{ji} L}{2E}}, \tag{1.20}$$

where $\Delta m^2_{ji} = |m_i^2 - m_j^2|$. This expression of the neutrino oscillation probability can be separated into sinusodial functions:

$$\begin{aligned} P(\nu_\alpha \to \nu_\beta)(L) =& \delta_{\alpha\beta} - 4\sum_{i<j} Re[U_{\alpha i} U^*_{\beta i} U^*_{\alpha j} U_{\beta j}] \sin^2 \frac{\Delta m^2_{ji} L}{4E} \\ &+ 2\sum_{i<j} Im[U_{\alpha i} U^*_{\beta i} U^*_{\alpha j} U_{\beta j}] \sin \frac{\Delta m^2_{ji} L}{2E}. \end{aligned} \tag{1.21}$$

Eqn. 1.21 shows that the probability of a neutrino switching flavor behaves as the sum of sinusoidal functions, with the period determined by the length of travel L, the square of mass difference Δm^2_{ji} and the neutrino energy E. This probability shown above is similar to a standing wave oscillation, hence this switching of flavors is named neutrino oscillation. Similarly, the probability of antineutrino oscillation from flavor α to β is:

$$\begin{aligned} P(\bar{\nu_\alpha} \to \bar{\nu_\beta})(L) =& \delta_{\alpha\beta} - 4\sum_{i<j} Re[U_{\alpha i} U^*_{\beta i} U^*_{\alpha j} U_{\beta j}] \sin^2 \frac{\Delta m^2_{ji} L}{4E} \\ &- 2\sum_{i<j} Im[U_{\alpha i} U^*_{\beta i} U^*_{\alpha j} U_{\beta j}] \sin \frac{\Delta m^2_{ji} L}{2E}. \end{aligned} \tag{1.22}$$

As shown in Eqn. 1.21 and 1.22, the variables that determine the probability of any oscillation are the mixing angles that make up the different components in the PMNS matrix. When $\alpha = \beta$, meaning that there is no change in flavor, the multiplication of PMNS matrix components becomes $U_{\alpha i} U^*_{\alpha i} U^*_{\alpha j} U_{\alpha j}$, and thus becomes a real number. It is when $\alpha \neq \beta$ that the probability of neutrino oscillation differs between neutrino and antineutrino, allowing one to calculate the CP-violating phase. As a result, the CP-violation can only be accessed by comparing oscillations between neutrinos and antineutrinos [16]. For the purpose of this thesis and T2K, the main oscillation channel used to investigate CP-violation is the $\nu_\mu \to \nu_e$ oscillation and its antineutrino

counterpart. With the assumption that $\Delta m^2_{21} << \Delta m^2_{32}$ and $\frac{\Delta m^2_{21} L}{E} << 1$, the probability of the oscillation from Eqn. 1.21 can be simplified into the following expression [16]:

$$P(\nu_\mu \rightarrow \nu_e) \approx \sin^2\theta_{23} \sin^2\theta_{13} \sin^2\left(\frac{1.267\Delta m^2_{32} L}{E}\right) + P_{CP}, \tag{1.23}$$

with P_{CP} the leading term that includes δ_{CP}, the CP-violation phase difference. Since the value of θ_{23} and $|\Delta m^2_{23}|$ have been measured experimentally, it is possible to retrieve one of the remaining variables in the PMNS matrix, θ_{13}, by measuring the probability of such neutrino oscillation, and also to extract δ_{CP}. Hence the T2K experiment is built, to measure θ_{13} and ultimately measure δ_{CP} experimentally.

1.3.3 Experimental results for neutrino oscillation

The first hint of neutrino oscillations was due to measurements of neutrinos from the sun, where the solar neutrinos were captured in a detector that utilizes the reaction of ν_e with ^{37}Cl. While the standard solar model should have a flux of $(9.3 \pm 1.3) \times 10^{-36}$ s^{-1} per ^{37}Cl atom, the Homestake experiment measured $(2.56 \pm 0.16) \times 10^{-36}$ s^{-1} per ^{37}Cl atom [17]. The lower bound of the theoretical calculations on the solar neutrino flux is about 3.6 times higher than the measured solar neutrino flux, which forms the solar neutrino problem that was solved in 2001, where the Sudbury Neutrino Observatory discovered the flavor oscillation of solar neutrinos, by discovering that electron neutrinos from the sun converted to other types of neutrinos (muon and tau neutrinos) in the sun [18]. This oscillation is caused by the MSW effect that describes neutrino oscillation in matter [19, 20].

The atmospheric neutrinos are neutrinos created in interactions of cosmic rays with the atmosphere, in which neutrino oscillations were discovered for the first time. Oscillations of atmospheric neutrinos were observed by the Super-Kamiokande (Super-K) experiment in 1998 [21], where the data from collecting atmospheric neutrinos in Super-K revealed that there is a dependency of the zenith angle on the deficit of muon-neutrinos. As a result, the experiment concluded that there is disappearance of muon neutrinos, which is interpreted as $\nu_\mu \rightarrow \nu_\tau$ oscillations, with a mixing angle $\sin^2 2\theta > 0.82$ and $5 \times 10^{-4} < \Delta m^2 < 6 \times 10^{-3}\,\mathrm{eV}^2/\mathrm{c}^4$ with a 90% confidence level.

Since the Cowan and Reines experiment in 1958, reactor neutrinos from beta decay have been observed through the neutrino interaction, producing positrons that annihilate to produce photons, followed by neutron capture [8]. The Daya-Bay experiment, that was built around the Daya-Bay nuclear plant, used a similar method to that used by Cowan, and measured a new type of neutrino oscillation, in which electron antineutrinos disappear, giving the neutrino mixing angle $\sin^2 2\theta_{13} = 0.092 \pm 0.021$ with a 5.2σ confidence level [22]. Within the same year, the RENO experiment also confirmed the discovery of θ_{13}, with $\sin^2 2\theta_{13} = 0.113 \pm 0.023$ with

4.9σ, which further supported the discovery made by the Daya-Bay experiment [23].

As stated in section 1.3.2, the values of θ_{23}, and $|\Delta m_{32}|$ have been measured experimentally. The most recent analysis on the latest data, published in 2020, obtained the following results, $\sin^2\theta_{23} = 0.51^{+0.06}_{-0.07}$ and $|\Delta m^2_{32}| = 2.47^{+0.08}_{-0.09} \times 10^{-3}\,\mathrm{eV}^2/\mathrm{c}^4$ for neutrino oscillation, and $\sin^2\theta_{23} = 0.43^{+0.21}_{-0.05}$ and $|\Delta m^2_{32}| = 2.50^{+0.18}_{-0.13} \times 10^{-3}\,\mathrm{eV}^2/\mathrm{c}^4$ for antineutrino oscillation, to a 90% confidence level [24]. The results from analysing T2K data sets are also being analysed alongside results from other long baselineline experiments such as the NOνA [25], the MINOS [26] and the K2K experiments [27], and a global analysis is performed to obtain neutrino oscillation parameters through a global fit. For the global fit, $\sin^2\theta_{23} = 0.541 - 0.599$ and $|\Delta m^2_{32}| = (2.39 - 2.50) \times 10^{-3}\,\mathrm{eV}^2/\mathrm{c}^4$, to a 90% confidence level [28]. These analyses marginally favor that neutrino mass eigenstates have a normal ordering, that is the mass eigenstates are ordered with masses $m_1 < m_2 < m_3$. The constraints of the oscillation parameters are shrinking as new updates of current experiment sites and new research facilities constantly improve the precision and resolution of neutrino oscillation experiments.

The analysis of the latest batch of data retrieved from T2K has shown a total of 15 $\bar{\nu}_e$ detected from a $\bar{\nu}_\mu$ beam in the latest run. The expected value for the $\bar{\nu}_e$ from background is 9.3 events. This result rejects the null hypothesis that no $\bar{\nu}_e$ is produced from a $\bar{\nu}_\mu$ beam (no neutrino oscillation) with a confidence interval of 2.40σ [29]. While the confidence interval is not large enough to claim a discovery (5σ), this result is still a hint for the existence of antineutrino oscillations.

1.3.4 Neutrino interactions

The neutrino interacts only by the weak interaction, where the neutrino interacts with particles with the mediation of $W^\pm$ and Z^0 bosons. Depending on the boson included in the interaction, a neutrino interaction can be defined in two categories, charged current and neutral current. In charged current interactions the $W^\pm$ are involved in mediating the interaction between particles, and thus providing a change of charge in the interaction. Meanwhile the neutral current interaction involves the Z^0 boson and thus no charges are exchanged. Since the cross-sections of charged current interactions are around four times larger than that of the neutral current, and the fact that charged current interactions contain charge transfer that is easier to be detected, only charged current interactions will be further introduced below.

Charged current quasi-elastic (CCQE) interactions

Charged current quasi-elastic (CCQE) interactions occur when the incident particle has a relatively low energy (less than 1 GeV). In this case, a lepton (anti)neutrino interacts with a nucleon, producing a corresponding lepton and changing the charge of the nucleon as shown in the fol-

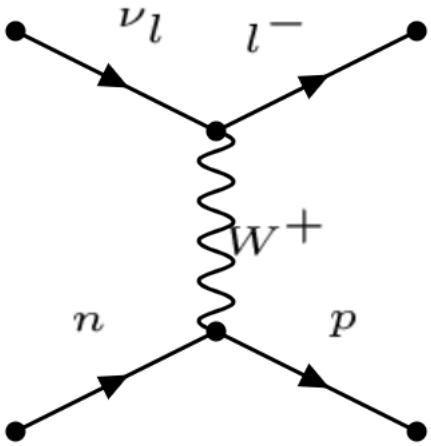

Figure 1.2: The Feynman diagram of a typical CCQE interaction.

lowing equations,

$$\begin{aligned} \nu_l + n &\rightarrow l^- + p, \\ \bar{\nu}_l + p &\rightarrow l^+ + n. \end{aligned} \tag{1.24}$$

The lepton is represented by l, and can be either electron or muon. A lepton neutrino interacts with a neutron and the anti-neutrino interacts with a proton, in order to conserve the charge before and after the interaction. As shown in Eqn. 1.23, the neutrino oscillation peaks when $\sin^2\left(\frac{1.27\Delta m^2_{23}L}{4E}\right) = 1$. As a result, it is necessary to design the length of the path that the neutrino travels and the energy of the beam such that $\frac{1.27\Delta m^2 L}{4E} = \pi, 3\pi, 5\pi$ etc. to obtain the highest oscillation possibility. Therefore, T2K has decided to use a neutrino travel length $L = 295\,\text{km}$ and $E = 0.6\,\text{MeV}$ for the neutrino oscillation experiment. Under such neutrino beam energy, most of the interactions will be CCQE interactions. Therefore, the CCQE interaction will be the main interaction focused in this thesis. There are two sets of near detectors at T2K, the ND280 detector which is at 2.5° from the neutrino beam, peaking at an energy of $E = 0.6$ GeV, and the WAGASCI/BabyMIND detector complex which is at 1.5°, with a peak energy of $E = 0.8$ GeV. Therefore, the main neutrino interactions of focus in this thesis will be those at these energies.

Since the main focus of T2K is the neutrino oscillation from ν_μ to ν_e as a function of energy, it is useful, for the purpose of this thesis, to demonstrate how one extracts the energy of the neutrino interaction, through the expression for the neutrino energy for muon neutrinos under the CCQE interaction as follows (see Appendix A for proof):

$$E_\nu^{CCQE} = \frac{m_P^2 - m_\mu^2 - E_N^2 + 2E_\mu E_N - 2\mathbf{p}_\mu \cdot \mathbf{p}_N + |\mathbf{p}_N|^2}{2(E_N - E_\mu + |\mathbf{p}_\mu|\cos\theta_\mu - |\mathbf{p}_N|\cos\theta_N)}. \tag{1.25}$$

The equation above represents the neutrino energy for a CCQE interaction shown in Fig. 1.2, where E_μ, $\vec{p}_\mu$ and m_μ are the energy, momentum and mass for the outgoing muon, with E_P, $\vec{p}_P$ and m_P the corresponding properties of the proton, and E_N, $\vec{p}_N$ and m_N those for the neutron. The angles θ_μ and θ_N are the angles between the motion of the respective particle and the incoming neutrino (see Appendix A for more details). Assuming that the neutrino interaction follows the relativistic Fermi gas model, then we can assume that the neutron is at rest before the interaction and $E_N = m_N - \varepsilon$ can be used as a simplification, where ε is the neutrino binding energy for the relativistic Fermi gas model and m_N is the mass of neutron. After all the assumptions, the equation can be simplified as:

$$E_\nu^{CCQE} = \frac{m_P^2 - m_\mu^2 - m_N^2 + 2m_N\varepsilon - \varepsilon^2 + 2E_\mu m_N - 2E_\mu\varepsilon}{2(m_N - \varepsilon - E_\mu + |\mathbf{p}_\mu| cos\theta_\mu)}. \tag{1.26}$$

Since Eqn. 1.26 contains known variables such as the mass of the proton, muon and neutrino, and the value of ε (given by nuclear models, such as the nuclear Fermi-gas model), the only unknown that should be retrieved from simulation are the absolute momentum of the muon, the angle of the muon with respect to the neutrino and the energy of the muon, which can all be retrieved from a muon track. Such an expression can be used to extract the energy of the incoming neutrino based on data obtained from the reconstructed muon track. The probability of a CCQE interaction occuring depends on the cross-section area of the CCQE interaction. This interaction is usually expressed using a format developed by Llewellyn-Smith [30]. The expression includes different Lorentz-invariant parameters, parameters that stay the same under any Lorentz transformation, that are functions of Q^2, where Q is the four-momentum transfer. The expression, for the differential cross section for any CCQE interactions, is the following [30, 31]:

$$\frac{d\sigma}{dQ^2} = \frac{G_F^2 M_N^2 \cos^2\theta_c}{8\pi E_\nu^2}\left[A + B\frac{(s-u)}{M_N^2} + C\frac{(s-u)^2}{M_N^4}\right]. \tag{1.27}$$

This expression of the differential cross section includes multiple constants and variables that need to be further explained. The constant G_F is the Fermi coupling constant, and θ_c is the Cabbibo angle. The variable M_N is the mass of the nucleon and E_ν is the energy of the neutrino. The expression $(s-u) = 4M_N E_\nu - Q^2 - m^2$ where m is the mass of muon. The coefficients A, B and C are functions that depend on the vector, axial-vector and pseudo-scalar form factors. These form factors represent the respective hadronic current for the CCQE interaction. There are vector form factors F_1 and F_2, the axial-vector form factor F_A and the pseudo-scalar form factor F_P involved in the coefficients A, B and C [31, 30]:

$$\begin{aligned} A = &\frac{m^2+Q^2}{M_N^2}\left[(1+\tau)F_A^2 - (1-\tau)F_1^2 + (1-\tau)F_2^2 + 4\tau F_1 F_2\right. \\ &\left. - \frac{m^2}{4M_N^2}\left((F_1+F_2)^2 + (F_A+2F_P)^2 - \left(\frac{Q^2}{M_N^2}+4\right)F_P^2\right)\right]. \end{aligned} \tag{1.28}$$

Since in the case of the muon neutrino CCQE interaction that this thesis is interested, $\frac{m^2}{M_N^2} \ll 1$,

$$A = \frac{m^2+Q^2}{M_N^2}\left[(1+\tau)F_A^2 - (1-\tau)F_1^2 + (1-\tau)F_2^2 + 4\tau F_1 F_2\right], \tag{1.29}$$

$$B = \frac{Q^2}{M_N^2} F_A(F_1+F_2), \tag{1.30}$$

$$C = \frac{1}{4}(F_A^2 + F_1^2 + \tau F_2^2). \tag{1.31}$$

These three factors, once simplified, are functions of F_1, F_2, F_A, and $\tau = \frac{Q^2}{4M_N^2}$. These form factors are composed of different constants that are retrieved experimentally and are therefore constants based on experimental values. The values of the vector form factors can be extracted by electron scattering, but the axial-vector form factor F_A is retrieved mainly from neutrino scattering. Thus experiments that measure neutrino CCQE interactions such as at the T2K near detector can help provide more data on F_A for a more accurate calculation of the CCQE cross-section. The expression for F_A is usually approximated with the formula:

$$F_A(Q^2) = \frac{g_A}{\left(1+\frac{Q^2}{m_A^2}\right)^2}. \tag{1.32}$$

In the axial-vector form factor, g_A and m_A are all constants where $g_A = -1.267$ [32, 33] is the best value retrieved from various experiments, and $m_A = 1.21 \pm 0.20\,\mathrm{GeV/c^2}$ [34] is the value used in NEUT, the neutrino generation package in used by T2K, that averages different values extracted from various experiments. These constants can be improved with more precise experiments.

Charged Current Resonant (CCRES) interactions

When the energy of the neutrino is above $0.6\,\mathrm{GeV}$, there may be enough energy for the nucleons to be excited by the (anti)neutrino. The nucleon gets excited to a Δ resonance, which further decays to a nucleon and a pion. The charge of the Δ resonance depends on whether the neutrino or the antineutrino was interacting with the nucleon, and the type of nucleon and pion from the

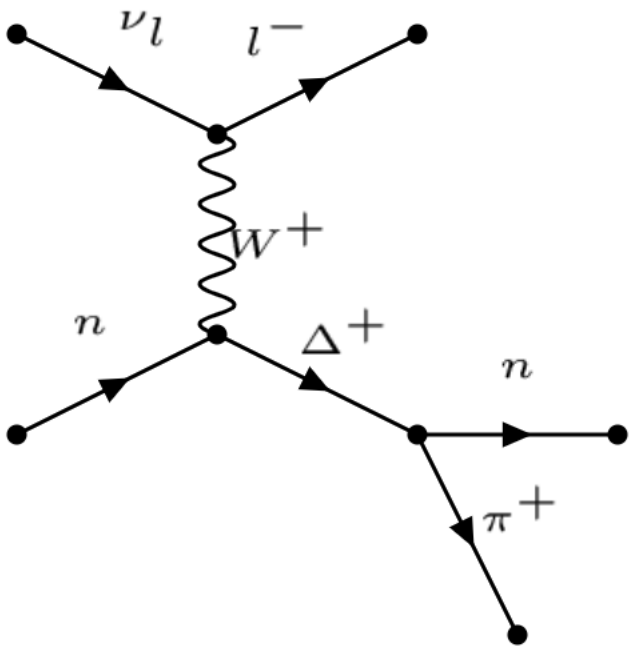

Figure 1.3: The Feynman diagram of one of the typical CCRES interactions.

resonance decay depends on the type of Δ particle created as follows:

$$\begin{aligned}
&\nu_l + n \to l^- + p + \pi^0(\Delta^+),\\
&\nu_l + n \to l^- + n + \pi^+(\Delta^+),\\
&\nu_l + p \to l^- + p + \pi^+(\Delta^{++}),\\
&\bar{\nu}_l + p \to l^+ + n + \pi^0(\Delta^0),\\
&\bar{\nu}_l + p \to l^+ + p + \pi^-(\Delta^0),\\
&\bar{\nu}_l + n \to l^+ + n + \pi^-(\Delta^-).
\end{aligned} \tag{1.33}$$

An example of a CCRES interaction is shown in figure 1.3. Such interactions are defined as the charged current resonant elastic scattering (CCRES) interactions, or pion production. Since the flux of the beam used in T2K peaks at 0.8 GeV for WAGASCI-BabyMIND, some CCRES interactions will be produced and some pion production is expected to be detected. However, since the peak of the flux is just at the threshold of CCRES interactions, it is not expected for the T2K experiment to observe a high yield of pion production from CCRES interactions. As a result, for convenience, CCRES can be ignored from the simulation as an approximation.

CCDIS

If the energy of the neutrino exceeds around 5 GeV, there is enough energy from the neutrino to break up the nucleon, causing a deep inelastic scattering (CCDIS) interaction. During CCDIS, the nucleon is broken up into quarks by the high energy neutrino, which form a variety of hadrons from the collision. Since the threshold energy for CCDIS to occur is above the majority of the neutrinos produced by the T2K beam, the fraction of CCDIS interactions is very low, and is assumed to be negligible in this thesis.

1.3.5 Experimental results on neutrino interactions

Neutrino interactions are necessary to determine the cross-section of each interaction in different energy ranges. The cross-sections of CCQE neutrino interactions are obtained from different research projects such as NOMAD [35] and MiniBooNE [36], as shown in Fig. 1.4 and 1.5. However, the data from MiniBooNE has cross-sections at low energies that are higher than the expectation from the Fermi-gas model, alongside calculations using the impulse approximation. This leads us to believe that neutrino interactions are more than free particle interactions, and it is necessary to include the nucleon-nucleon correlations and two-body exchange currents.

For antineutrinos, there is currently a lack of data for low energies (< 1 GeV), and it is now a high priority to take more data with antineutrinos. The study of neutrino and antineutrino cross-sections, especially at low energies, is essential for neutrino oscillation experiments since most of the experiments on neutrino oscillations use relatively low energy beams that have a peak energy in the CCQE energy region. Similar experiments on cross-sections were also conducted for pion productions (CCRES) to obtain a relationship between the pion production cross-sections and neutrino energies [37]. Such experiments provide the foundation for neutrino oscillation experiments, such as the T2K experiment that this thesis concerns.

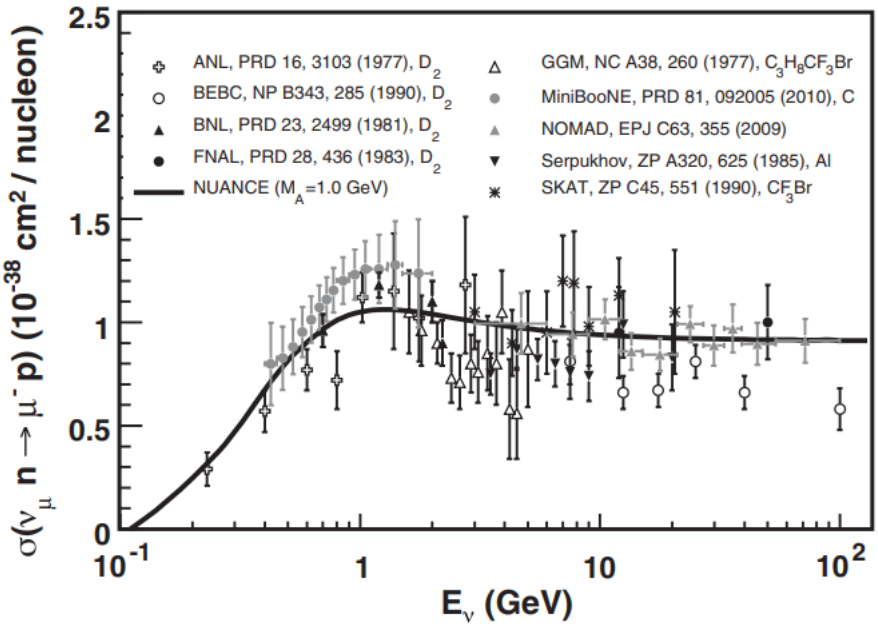

Figure 1.4: Measurements of muon neutrino CCQE cross-sections with respect to the neutrino energies. Data points from different laboratories are included and the solid line is the prediction of a neutrino Monte Carlo simulation [37].

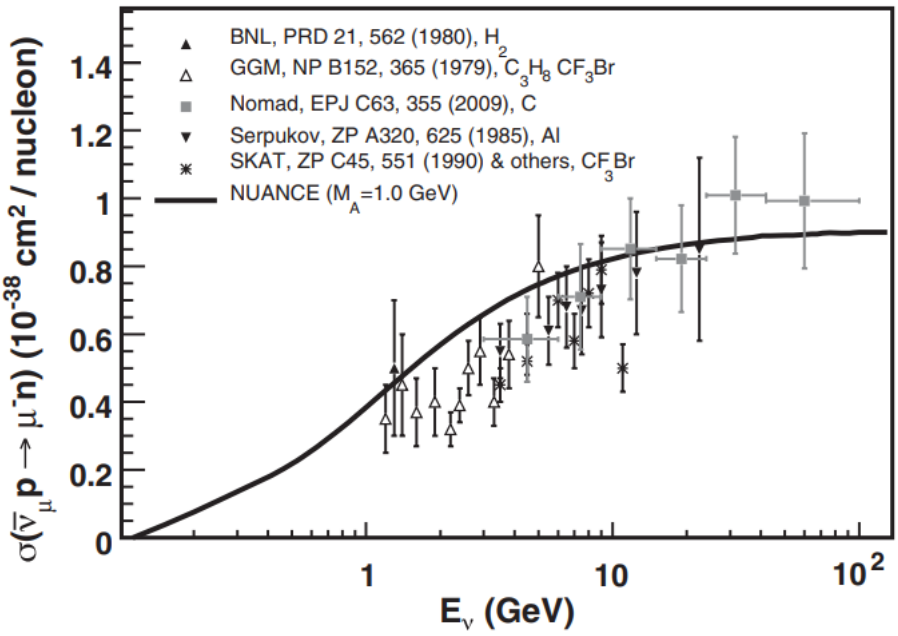

Figure 1.5: Measurements of muon antineutrino CCQE cross-sections with respect to the neutrino energies. Data points from different laboratories are included and the solid line is the prediction of a neutrino Monte Carlo simulation [37].

Chapter 2

T2K, WAGASCI and BabyMIND

2.1 T2K experiment and goals

The Tokai-to-Kamioka (T2K) experiment is a neutrino oscillation experiment utilizing the particle accelerator that is located in the J-PARC complex in the village of Tokai, on the east coast of Japan, which is used to generate a neutrino beam pointed at the Super-Kamiokande far detector in Kamioka. The experiment is composed of different types of near detectors at Tokai and a far detector named Super-Kamiokande (Super-K) located at Kamioka, 295 km from Tokai. These near detectors near the beam line are 280 m from the start of the beam, hence the complex is named ND280. The ND280 detector is located at a 2.5° off-axis angle with respect to the decay pipe of the beamline, which generates a neutrino beam reaching the detector with a peak energy flux of 0.6 GeV. This peak value minimizes background and maximizes the possibility of neutrino oscillation events at 295 km [38].

One of the main purposes of the T2K experiment was to discover the $\nu_\mu \rightarrow \nu_e$ oscillation and to measure the mixing angle θ_{13}, the last mixing angle in the lepton sector [39]. From here, the goal is to measure CP violation in neutrinos and to find a value of δ_{CP} that is not consistent with CP conservation.

2.2 JPARC accelerator complex and neutrino beam

2.2.1 The J-PARC accelerator

The beamline used in T2K is generated from the J-PARC accelerator complex, which is composed of three accelerators. The linear accelerator (LINAC) accelerates H^- beams to 400 MeV in order to pass the beam into the second part of the accelerator. The accelerated beam then enters the rapid-cycling synchrotron (RCS) that accelerates the beam to an energy of 3 GeV, while converting the H^- beam into a H^+ beam by charge-stripping foils at injection. About 5% of the beamline from the RCS is injected into the main ring synchrotron (MR), accelerated up

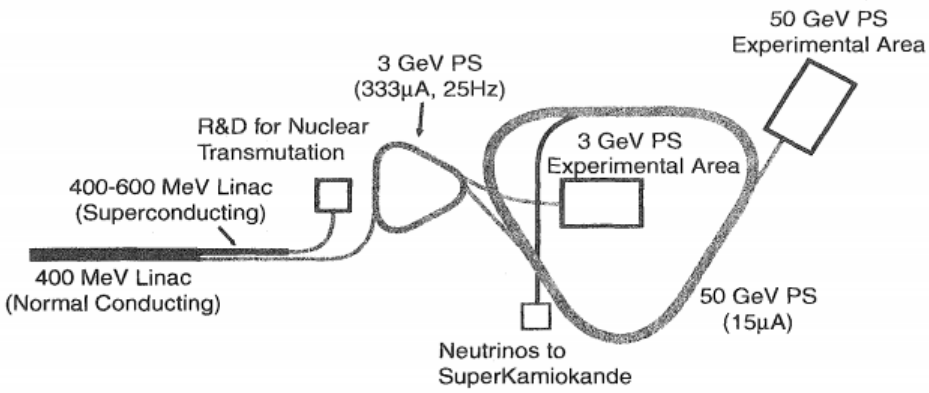

Figure 2.1: A diagram of the J-PARC accelerator complex with the LINAC on the left, RCS in the middle (3 GeV proton synchoron, PS) and the MR on the right (labelled as 50 GeV PS since it was originally designed for 50 GeV but was redesigned for 30 GeV) [40].

to 30 GeV in the MR. The diagram of the J-PARC accelerator is shown in Fig. 2.1 [38, 40, 41].

The proton beam accelerated by J-PARC is passed into the T2K neutrino beamline, which is composed of a primary beamline and a secondary beamline, as shown in Fig. 2.3. The primary beamline transports the proton beam to a direction pointing towards Super-K, and causes the beam to impinge on a carbon target, which generates secondary pions and kaons. Magnetic horns focus these into the secondary beamline. The first magnetic horn surrounds the graphite target to focus the pions of the correct polarity, with two other magnetic horns downstream of the first horn. After the magnetic horns, the pions and kaons are allowed to decay into different neutrinos in a 96 m decay pipe.

2.2.2 Neutrino beam

Primary beamline

The primary beamline consists of 11 normal conducting magnets in the preparing section, 14 doublets of superconducting combined function magnets in the arc section, and 10 normal conducting magnets in the focusing section, as shown in Fig. 2.3. The preparing section ensures that the beam is accepted in the arc section. The arc section then bends the beamline 80.7° from the direction of the preparation section towards Kamioka. The final focusing section focuses the beam towards the graphite target in the secondary beamline, tilting the beam 3.673° downwards from horizontal.

Neutrinos from the beamline reach the ND280 detector complex with a 2.5° off-axis angle, and reach the WAGASCI-BabyMIND detector complex with a 1.5° off-axis angle. The off-axis angles modify the neutrinos from the beam to have different energy spectra detected by each detector complex. For the neutrinos detected by ND280, the peak energy flux (the energy

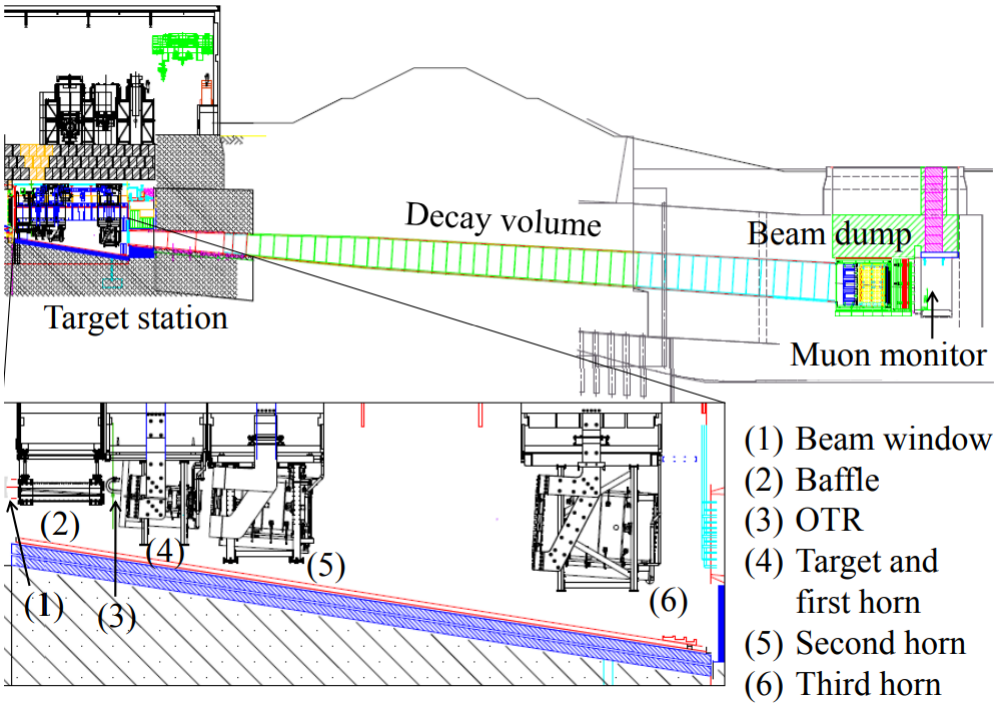

Figure 2.2: The side view of the secondary beamline [38].

flux where the neutrino has the highest probability to have an interaction) is around 600 MeV whereas for the neutrinos, seen from a different angle, detected by WAGASCI, the peak flux is around 800 MeV. Alongside the beamline there are devices monitoring the beam intensity, location, profile and loss. These monitors are to make sure the parameters of the primary beam are optimal for the next stage.

Neutrino target and secondary beamline

The secondary beamline is composed of three different sections as shown in Fig. 2.3 and with more detail in Fig. 2.2. The target part of the beamline, as shown in the zoomed-in portion of Fig. 2.2, consists of a beam window separating the primary and secondary beamline, a baffle protecting the magnetic horns, an optical transition radiator monitor (OTR), and three magnetic horns with a graphite target inside the first horn.

The whole target station is surrounded by a helium vessel filled with helium gas, with a shield made with iron and concrete above the horns that blocks the radiation produced inside the horn. A water cooling channel (the plate coil) is also installed above the surface of the helium vessel. The plate coil is filled with 30° C water that cools the vessel to maintain a lower temperature and to prevent thermal deformation. There is also a graphite block with a hole of 30 mm diameter in the middle as a baffle between the beam stop and the target-horn structure that is cooled by the water cooling system running through the baffle. The OTR serves the purpose of detecting the proton beam passing through the OTR by reflecting the visible light generated near the proton beam when the beam enters and exits an aluminium foil 45° from the incident beam. The visible

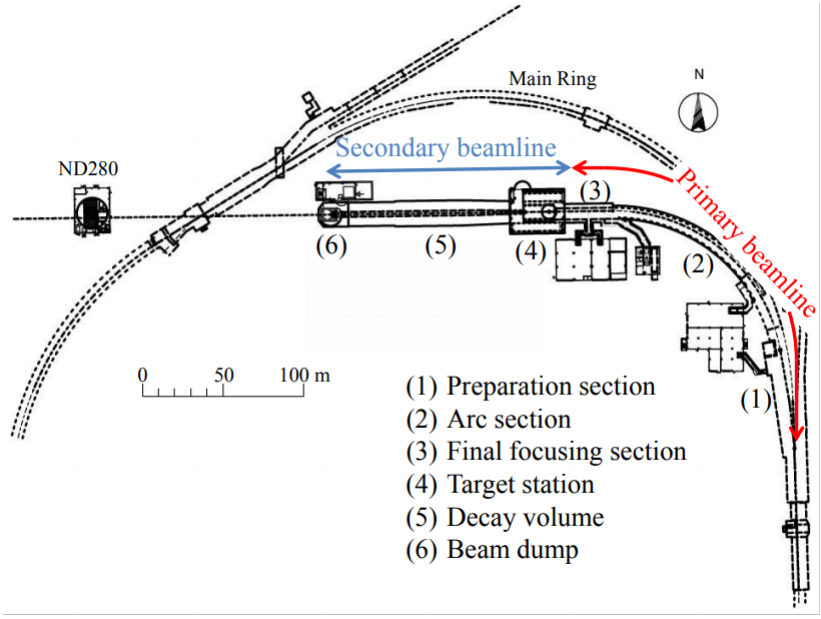

Figure 2.3: A diagram of the T2K neutrino beamline [38].

light is reflected at 90° to the beam by the foil and transported to a camera away from the beam to observe the image of the proton beam.

The three magnetic horns, made with an aluminium alloy, each consist of an inner and outer coaxial conductor that covers the surface of the horns. By running a current of 250 kA on the thin conductor surrounding the horn, a torodial magnetic field is generated in the three magnetic horns [38, 42, 43]. As stated in the Lorentz equation,

$$\vec{F} = q \cdot \vec{v} \times \vec{B}, \tag{2.1}$$

a charged particle, when going through a magnetic field perpendicular to the direction of motion, experiences a force perpendicular to the direction of the field and the direction of the charged particle. Depending on the direction of the current running through the conductor surrounding the horn, the magnetic field in the volume enclosed by the conductor can be clockwise or anti-clockwise as seen from the pion's perspective. If the magnetic field is clockwise, a particle with positive charge, π^+, that passes through the magnetized region will be bent inward to the horn, while a π^- will be bent outwards. As a result, a clockwise magnetic field in the horn focuses the π^+ beam while defocusing the π^- in this case. The same holds true for anti-clockwise magnetic fields, in which the π^- is focused and the π^+ is defocused. Fig. 2.4 demonstrates such a focusing function of the magnetic horn. The current where it creates the clockwise magnetic field is defined as the forward-horn current (FHC) and the opposite is defined as the reverse-horn current (RHC). The maximum field strength, if running the current at 320 kA, is 2.1 T and increases the neutrino flux arriving at Super-K by 16 times at the peak energy flux of 0.6 GeV in the flux spectrum.

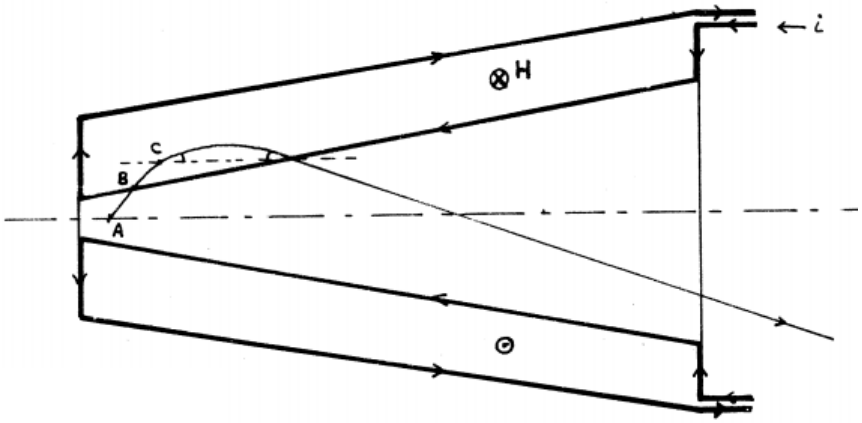

Figure 2.4: A diagram of how an anti-clockwise magnetic horn focuses the π^-. The particle starts from A, enters the magnetic field region at B, and then gets bent at C towards D [43].

A graphite target with 91.4 cm length and 2.6 cm in diameter [38] is installed at the start of the first horn as shown in Fig. 2.5. The target is surrounded by a titanium sheath with helium gas flowing in between as a coolant. This target is supported by a cantilever at the front of the first horn, securing the position of the target. When the beam enters the target, secondary pions are produced, increasing the overall yield of desired pions with the help of the magnetic horn. Although in theory it should be best to have a target as long as the horn, the effect of gravity may prevent such long target to remain a desirable form and shape. Graphite was also chosen, due to the radiation hardness of the material, in addition to graphite's ability to withstand heat generated in the experiment.

One of the goals of this thesis is to investigate improvements on such a horn-target system by providing a simulation on different scenarios with an extra target at the other end of the first horn. A more in-depth discussion will be held in section 3.

The decay volume, approximately 96 m long [38], is a stainless steel tube that allows the pion to perform the following decay,

$$\pi^+ \rightarrow \mu^+ + \nu_\mu \tag{2.2}$$

$$\pi^- \rightarrow \mu^- + \bar{\nu}_\mu. \tag{2.3}$$

As a result, a FHC magnetic horn increases the yield of ν_μ while a RHC magnetic horn increases the yield on $\bar{\nu}_\mu$. By switching the direction of the current, different experimental ratios of ν_μ and $\bar{\nu}_\mu$ can be satisfied with the same horn.

The beam dump, at the end of the secondary beamline, has a core made of 75 tons of graphite, a helium vessel surrounding the core, 2 iron plates inside the vessel and 15 iron plates outside the vessel. This dump filters out all the particles except muons with energy > 5 GeV and neutrinos

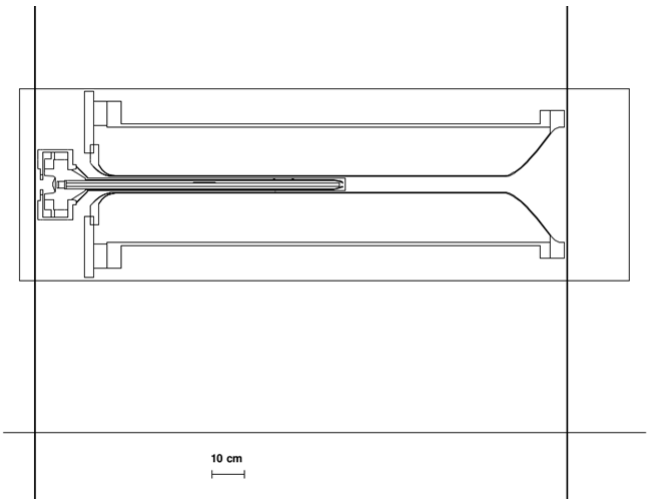

Figure 2.5: A side view of the first horn with a graphite target generated by JNUBeam [44], the simulation package written for T2K beam simulation

[38]. At the end of the beam dump there is a muon monitor installed to record the muon flux from the pion decay in Eqn. 2.2 and 2.3 in order to identify the number of muons that are detected in the detector downstream of the neutrino beamline.

2.3 ND280 near detector complex

The ND280 detector complex, located 280 m away from the start of the beamline, consists of the off-axis detector 2.5° from the beamline on the top of the ND280 complex and the INGRID on-axis detector at the bottom of the complex. The ND280 detector is composed of a pi-zero detector (P0D) and a tracker downstream of the pi-zero detector. The P0D is made by alternating plastic scintillation bars, as the detector that records particle hits, and either a water target or foils made out of brass or lead. The tracker is made of three time projection chambers (TPC) and two fine grained detectors (FGD). These detectors are inside a dipole magnetic field, with an electromagnetic calorimeter (ECAL) surrounding them and scintillators inserted in the iron flux return slots, making up the side muon ranger (SMRD) [38]. The Hamamatsu Multi-Pixel Photon Counters (MPPC) are used as sensors to read out the light signals of the ND280 detectors, with a gain of $0.5 - 1.5 \times 10^6$, and with 667 pixels per sensor.

Scintillators are composed of several plastic bars with identical dimensions, with MPPC detectors built-in. When stacked together, horizontally or vertically, each bar provides information of whether the target particle hits through this particular bar in the scintillator plane, thus retrieving the x or y position on the plane with an accuracy of $1/\sqrt{12}$ of the width of the bar. The z position is determined by whether a hit is detected in any of the bars in the plane. As a result, the accuracy of a scintillator plane is determined by the width and the depth of a single bar, and a scintillator plane can only retrieve information of either x or y, but not both.

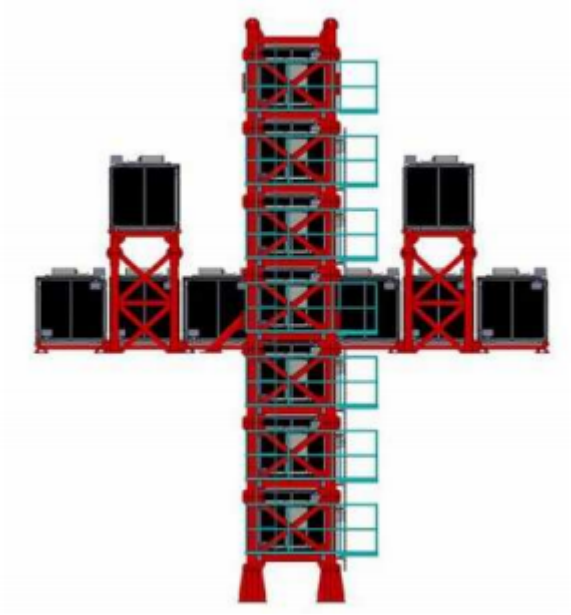

Figure 2.6: The layout of the 16 modules of the INGRID detector. Two of the modules are stacked along the axis in the center of INGRID (into the page at center), thus a total of 16 modules [38].

The ND280 off-axis detector is able to detect and record the ν_μ at the near detector of the T2K complex, providing information to determine the flux of ν_μ in Super-K. The ND280 is also made to detect ν_e passing through, determining the background from intrinsic ν_e in the beam, before oscillation [38].

2.3.1 INGRID on-axis detector

The INGRID on-axis detector is a detector complex that consists of 16 identical detector modules as shown in Fig. 2.6. Each module is made from 9 iron plates and 11 scintillator planes, surrounded by veto scintillator planes. The INGRID on-axis detector aims to detect and monitor the direction and intensity of the neutrino beam from the beamline. The direction of the beam to the two modules at the center of INGRID is defined as the 0° direction from the beamline. There is also an extra proton module installed in INGRID, only made out of scintillator planes, which aims to detect the muons and protons created in INGRID. The goal of this proton module is to identify quasi-elastic neutrino interactions to compare with Monte Carlo simulated data.

To record and veto the tracks from outside the modules, there are 3-4 veto plates per module, each made out of 22 scintillator bars combined into planes. This whole structure is enclosed by a box formed by aluminium frames and plastic plates. The readout boards are attached at the outside of the box.

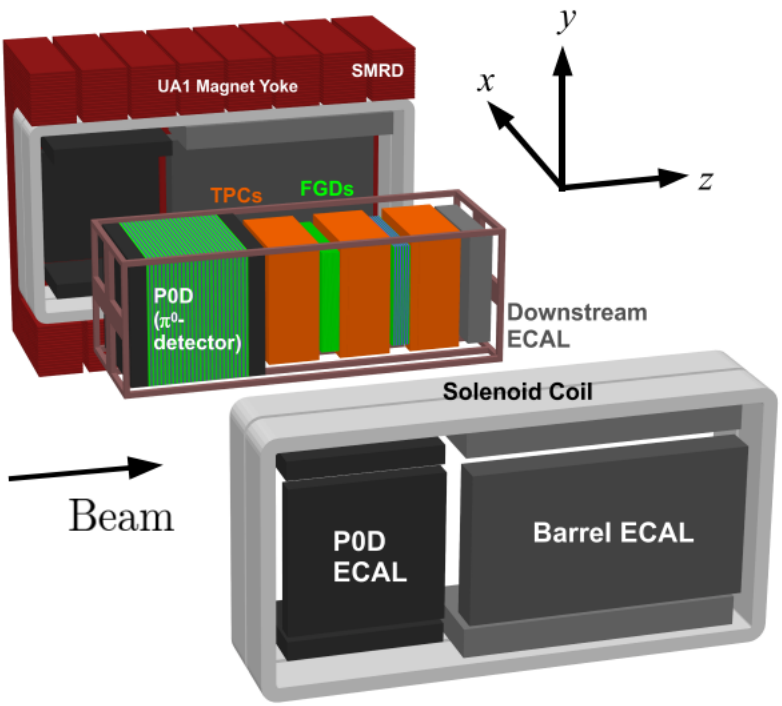

Figure 2.7: The layout of ND280 and its components [38].

2.3.2 ND280 off-axis detector

The off-axis detector, located above INGRID, serves to measure parameters of the neutrino beam at a near distance in comparison to when the beam reaches Super-K, in order to determine neutrino interactions in the near detector, the flux of neutrinos and to determine how many neutrinos have changed flavor in the far detector, to determine oscillations. The off-axis angle of 2.5° is the same as the off-axis angle of Super-Kamiokande with respect to the neutrino beam. The detailed structure of ND280 is demonstrated in figure 2.7.

UA1 magnet

The magnet around the detector structure originated from the old UA1 detector and recycled by the NOMAD experiment at CERN, is a $2\,\mathrm{m} \times 2\,\mathrm{m} \times 1\,\mathrm{m}$ structure that provides a dipole magnet of 0.2 T to measure the momenta and the charge of the particle created in the neutrino interaction. This magnet is composed of two symmetrical coils that splits further to halves, supported but electrically insulated by two magnet yokes that allow the two pieces of magnet to move to open and close positions freely. The power supply used for the induced magnet is designed and made by Bruker to provide a DC nominal current of 2900 A with a voltage drop of 155 V. There is also a cooling system, consisting of two demineralized water circuits to keep the induced magnet at

a low temperature. A magnet safety system ensures the magnet can be turned on when none of the components is faulty, and turn off the magnet immediately once a component fails. This power supply is controlled by the magnet control system that processes and analyzes the data input from the magnetic components [38].

Pi-0 Detector

The Pi-0 Detector (P0D) is a detector designed mainly to detect the neutral current process producing pions, $\nu_\mu + N \rightarrow \nu_\mu + N + \pi^0 + X$ that reacts with the H_2O, and compares the data collected with the data collected at Super-K. The P0D mainly consists of layers of scintillators, with a water target bag attached to each of the scintillators, providing the ability to choose whether water is filled in between each scintillator.

The center two modules of the P0D detector, the upper and central water targets, use scintillators with water and brass sheets in between scintillators. Meanwhile, the upstream and central calorimeters, located upstream and downstream of the water targets, consist of scintillators without water, and lead sheets between scintillators.The calorimeters act as a veto region for the water targets. There are a total of 40 scintillator modules in the P0D (P0Dules), with each P0Dule made of 134 vertical scintillator bars and 126 horizontal bars, forming a plate with an area of 2200 mm $\times$ 2340 mm. These scintillator bars are the same as what is described in Sec. 2.3. Each of the calorimeters are formed by seven of such P0Dules with seven 4 mm lead sheets attached right after each P0Dule. The upper water target consists of 13 P0dules, with 13 water bag layers that are 28 mm thick and 13 brass sheets with a thickness of 1.5 mm attached behind each P0Dules. The central water target will be similar to the upper water target, but the number of P0dules, water bags and brass sheets are 12 instead of 13 [38].

Time-project chambers

The time-project chambers (TPC) are chambers made with two copper boxes, with one inner box filled with argon gases, and one outer box filled with CO_2 gas. The inner box connects with a cathode and creates an electric field that has a direction that is the same as the magnetic field induced by the near detector magnets. When charged particles pass through the TPC, ionization electrons are produced and will be bent towards one of the receivers. Thus, the TPC is used to observe the track of charged particles inside the chamber. Due to the existence of the magnetic field, it is also possible for the TPC to determine the momentum of the traversed particles through the curvature of the track from the magnetic field, and, from the ionization of the particles in the gas, the identification of the particles traversing the TPC can also be made [38].

Fine grained detectors

There are two fine grained detectors (FGD) that are constructed from bars of scintillators. The goal of the two FGDs is to act as a target for neutrino interactions, and also to track charged particle tracks. The first FGD is purely composed of 5,760 scintillator bars, with a total of 30 layers that alternate vertically and horizontally, providing position information for tracks passing through. The second FGD is a combination of scintillator plates and water chambers. This provides an opportunity to compare neutrino interactions between the first and second FGDs, and thus study the cross-section of neutrino interactions in scintillator and water [38].

Electromagnetic Calorimeter

The electromagnetic calorimeters (ECal) are scintillator layers with lead absorber sheets in between. These ECals surround the inner part of ND280, including the P0D, TPC and FGDs. There are 6 P0D-ECals that surrounds the $x-z$ and $y-z$ planes of the P0D, a downstream ECal that is assembled at the downstream of the volume, and six barrel-ECals that surround the four sides of the tracker volume parallel to the z-axis. These ECals are made to measure the energy of the particles and also to provide a method to detect and measure the energy of photons from interactions in the P0D. ECals can also help to identify tracks from interactions and veto interactions from external particles, such as cosmic rays [38].

Side muon range detectors

The side muon range detectors (SMRDs) are scintillators that are inserted between air gaps and steel plates. These steel plates and air gaps form the UA1 magnet flux return yokes. These yokes are made of plates of iron that surround the inner detectors of ND280, retaining the magnetic flux return inside the iron. These SMRDs on the side allows the detection of tracks that escape from the side of the inner detectors. The SMRDs are also capable of recording cosmic radiations from the atmosphere that reach ND280 perpendicular to the z-axis which the detectors inside the volume are not capable of capturing [38].

2.4 Super-Kamiokande

The Super-Kamiokande (Super-K) detector is a large water Cherenkov detector located 295 km away from the start of the beamline, filled with 50 kt of pure water, in a cavern underground inside the Kamioka mine. The Super-K is a combination of an inner detector (ID) and an outer detector (OD), separated by stainless steel scaffolds that support the photomultiplier tubes. The ID is composed of 11,128 photomultiplier tubes (PMTs) facing inwards, with 40% photo-cathode area coverage, providing sufficient resolution for detecting neutrino interactions. The charged particles from neutrino interactions often create Cherenkov photon cones as they travel through

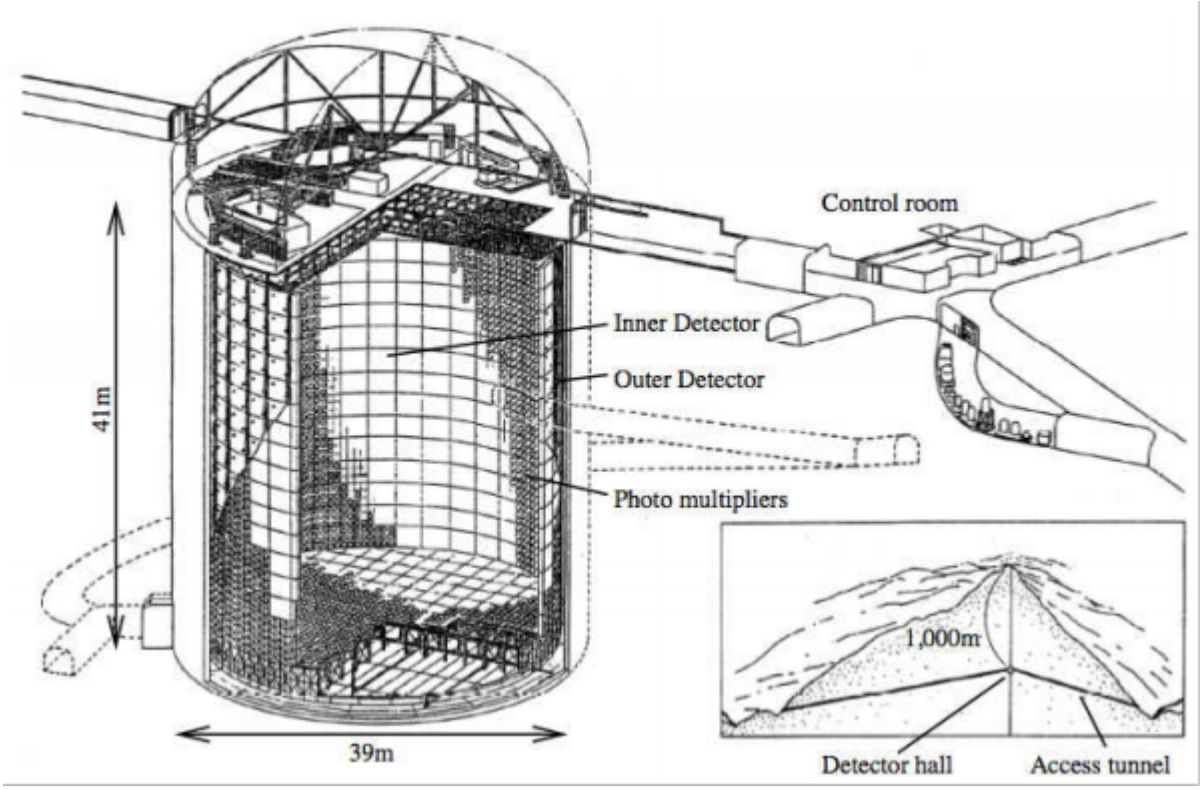

Figure 2.8: A diagram of the structure of Super-K [38].

water above an energy threshold. Thus by detecting the photons using the PMTs, the information of the charged particle, and thus the information of neutrino interactions can be retrieved. The OD, with PMTs facing outward, serves as a veto that tags almost 100% of the cosmic rays. The OD can also select neutrino-induced events from the background. The structure of Super-K is also shown in Fig. 2.8.

Super-K, combined with ND280, detects neutrino oscillations by counting the number of ν_μ and ν_e through the detection of muons and electrons from the respective CCQE interactions. Since muons are heavier than electrons, and they only lose momentum by ionization, the Cherenkov photon cones created by muons will be more well defined, providing a sharper edge on the Cherenkov cone. The Cherenkov cones from electrons, on the other hand, create a fuzzy ring, due to energy loss and electron scattering in the water. Through these signatures, the incoming flux of neutrinos is determined, and is compared with what is detected in ND280. The goal is to measure the neutrino oscillation $\nu_\mu \rightarrow \nu_e$ by recording electron hits in Super-K that are not due to the intrinsic ν_e from the original beam [38].

2.5 WAGASCI

The Water-Grid-Scintillator-Detector (WAGASCI) is a detector built in the same site of ND280, with an angle of 1.5° from the beamline. The main goal of WAGASCI is to improve the accuracy

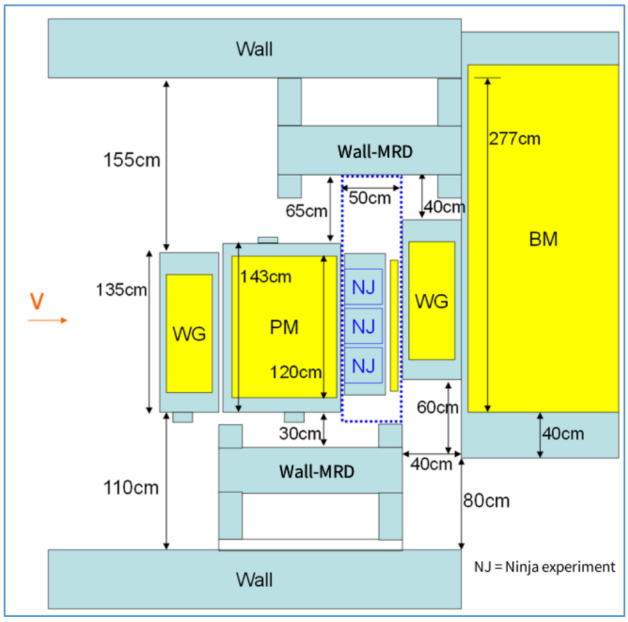

Figure 2.9: A diagram of the WAGASCI complex. The detector denoted NJ is the NINJA detector, which is a nuclear emulsion detector that is not part of the WAGASCI-BabyMIND project [46, 47]. The other detectors are WG (the two WAGASCI modules), the PM (proton module), Wall-MRD (muon-range detectors near the walls) and BM (BabyMIND).

of neutrino interactions in water and carbon, in order to constrain the systematic errors of the neutrino oscillations. The WAGASCI apparatus is made of a core part, that consists of the WAGASCI module and the proton module, and the two wall muon-range detectors (WallMRDs) surrounding the core. A layout of the WAGASCI complex is shown in Fig. 2.9. Unlike the ND280, the flux of ν_μ passing WAGASCI peaks at around 800 MeV due to the smaller angle to the neutrino beamline [45]. With WAGASCI, it is possible to study neutrino interactions with a different flux distribution on two different target materials (water and scintillator), and therefore study the neutrino cross-section with an off-axis angle of 1.5°, and compare the result obtained with results from ND280.

2.5.1 The WAGASCI module

The main difference between WAGASCI and other near detectors in the site, such as ND280, is the implementation of the water grid. Fig. 2.10 shows the structure of a WAGASCI module on the left. While there is a dimension shown in Fig. 2.10, there is a small difference between the diagram and what is used in the Monte-Carlo simulations developed by T2K researchers. In this thesis the values in the simulations are used to ensure the geometries of detectors in WAGASCI and BabyMIND are up to date.

The WAGASCI module has dimensions of 127.6 cm × 120.4 cm × 51 cm, with a water tank of 125.2 cm × 117.2 cm × 48.2 cm in the center as shown in Fig. 2.10. The plastic scintillators

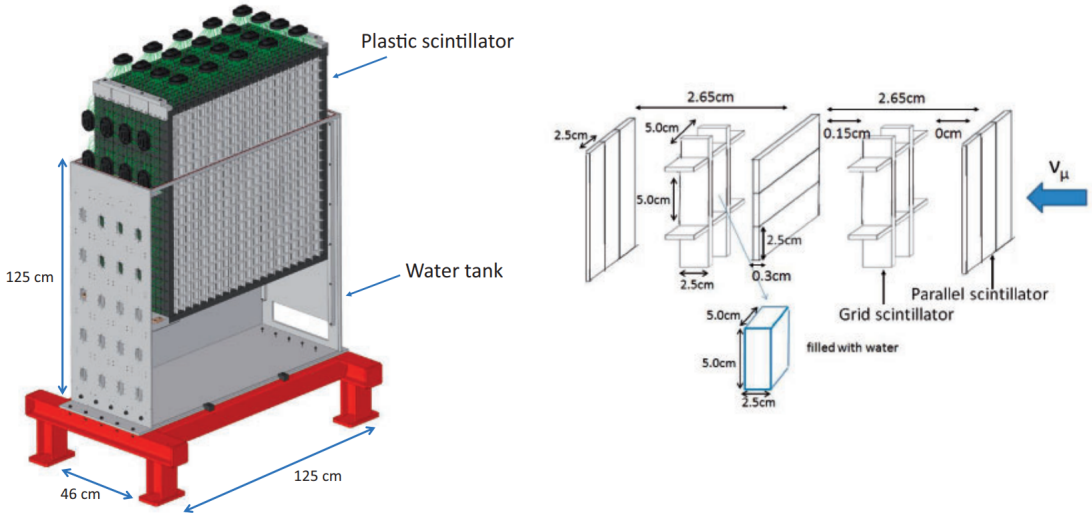

Figure 2.10: A diagram of the WAGASCI scintillator module inside the water tank on the left, and a diagram of the grid structure of scintillators (made out of hydrocarbons) and water on the right [48].

used in the WAGASCI module have dimensions of 102 cm × 2.5 cm × 0.3 cm, and a scintillator plate is combined with 40 of such scintillator bars. The WAGASCI module consists of eight of these scintillator plates, alongside with two segments of water grid targets. The same scintillator bars are used in constructing the water grid, with each grid being 5.0 cm × 5.0 cm × 2.5 cm. To assemble the grids, cuts of a depth of 0.13 cm and a thickness of 3.23 cm are performed. For each water grid module, a total of 80 slots are present, with a total of two water grid module in the whole WAGASCI module. In between the water grid and the scintillator plates, there are 0.65 cm gaps that separate each of them. These scintillator plates exist as tracking planes in between the water targets, and a total of eight plates are placed inside a WAGASCI module. The grid scintillator is placed inside the water tank, with the water occupying 80% of the total volume of the WAGASCI module, with the remaining 20% being hydrocarbon from scintillators. There are two WAGASCI water modules in total, one upstream and one downstream of the proton module that acts as the hydrocarbon target.

2.5.2 The proton module

The proton module, originally used in INGRID, is a hydrocarbon target consisting of 22 scintillator plates, with five of them acting as veto planes. Fig. 2.11 shows the layout of the proton module, with dimensions of 141.8 cm × 141.8 cm × 91.9 cm. The top, bottom, left, right and front side of the proton module have veto scintillator plates. For the bottom, left and front veto plates, the scintillator bars used have dimensions of 120.3 cm × 5.0 cm × 1.0 cm, while the top and right veto plates use longer scintillator bars with a length of 125 cm. These veto plates detect charged particles from outside of the proton module, to veto out such tracks in analysis if

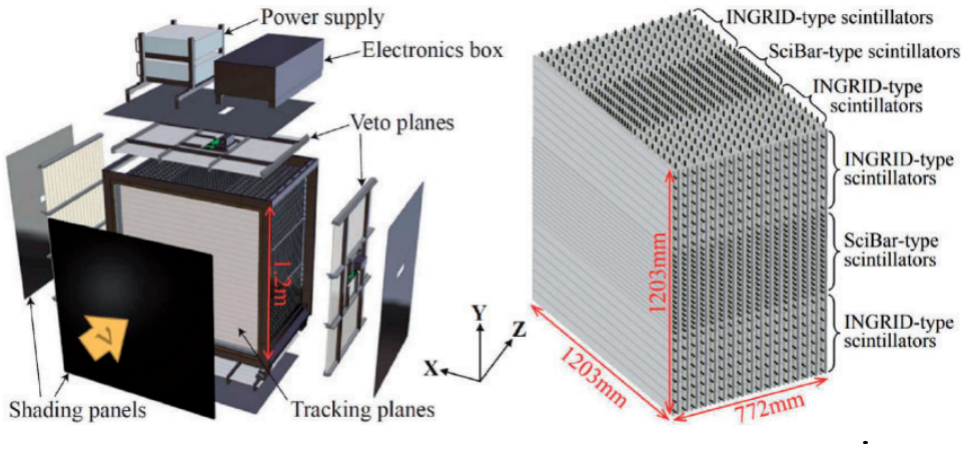

Figure 2.11: A diagram of the proton module on the left, and the structure of the two types of scintillators inside the proton module on the right [49].

needed.

For the tracking planes of the proton module, two types of scintillator bars, the INGRID-type scintillators and the SciBar-type scintillators are used together, as shown at the right of Fig. 2.11. Each of the tracking scintillator plates is composed of a horizontal and a vertical part to create a three dimensional image of the tracks. Each of the plates are assembled from 16 INGRID-type and 16 SciBar-type scintillator bars, with eight of each type in one direction. The SciBar-type scintillators are placed in the inner portion of the tracking plates, with dimensions of 120.3 cm $\times$ 2.5 cm $\times$ 1.3 cm. The INGRID-type scintillators have the same dimension as the shorter veto scintillator bars [49].

2.5.3 The wall side muon detectors

The wall side muon detectors (Wall-MRDs) are identical to the SMRDs explained in section 2.3.2, and the BabyMIND that will be further explained. The Wall-MRDs act as side detectors for muon tracks that escape from the WAGASCI and proton modules to the side walls. With dimensions of 205 cm $\times$ 163 cm $\times$ 46 cm, each Wall-MRD is made of 10 scintillator plates and 13 iron plates, with two of the iron plates at the two sides and two of the plates at front and rear, forming a frame for the Wall-MRD. The scintillator bars are 180 cm $\times$ 20 cm $\times$ 0.7 cm, and eight of them form a scintillator plate. Each of the side iron plates have dimensions of 190 cm $\times$ 46 cm $\times$ 1 cm, the front and rear plates have dimensions of 205 cm $\times$ 163 cm $\times$ 46 cm, and the rest of the iron plates inside the frame have dimensions of 180 cm $\times$ 161 cm $\times$ 3 cm. Each iron plate not on the sides has a 1.3 cm gap in between, enough to fit the scintillator plates inside. The iron and scintillator plates alternate to provide a good record of the tracks passing through the Wall-MRDs.

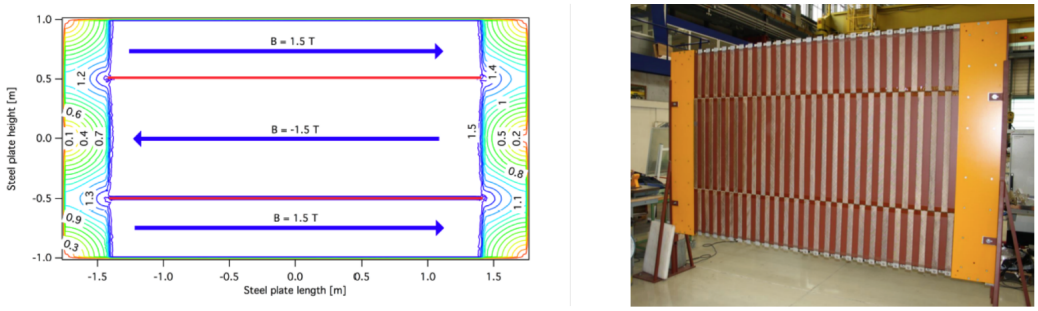

Figure 2.12: A diagram of the magnetic field distribution of a iron plate in BabyMIND (left), and a picture of the front of BabyMIND, showcasing the three sections of iron plates and the aluminium coils around the three sections in real life (right) [50].

2.6 BabyMIND

The Baby-Magnetized Iron Neutrino Detector (BabyMIND) is a detector built downstream of WAGASCI. The BabyMIND consists of 18 scintillator planes and 33 magnetized iron plates, in which the side view ($y-z$ plane) and top view ($x-z$ plane) is demonstrated in figures 2.13 and 2.14 respectively. The iron plates, denoted with orange colour in figures 2.13 and 2.14, have dimensions of $3.5\,\text{m} \times 2\,\text{m} \times 0.03\,\text{m}$, and each plate is divided into three sections. There are two slots cut into the iron plates at a height of -0.5 m and 0.5 m along the y-axis with respect to the center of the iron plates. For each section, aluminium coils are wrapped around the iron plates through the slots to form solenoids around the three sections of the iron plates. A current of 140 A goes through the solenoids with alternating direction between the top, middle and bottom sections. As a result, alternating magnetic fields are formed, with the top and bottom section having a magnetic field in the $+x$ direction and the middle part having a field in the $-x$ direction. All the iron plates in BabyMIND are magnetized to have a magnetic field strength of 1.5 T inside the plates and below 10 mT outside the iron plates. The magnetic field map inside the iron plates, and the picture of the front of BabyMIND with the iron plates are shown in Fig. 2.12.

The reason for the iron plates to be magnetized is to identify the charge of the muons in BabyMIND, and hence determine whether the neutrinos that generate these specific muons are ν_μ or $\bar{\nu}_\mu$. Due to the magnetic field being horizontal, and the muon entering BabyMIND roughly along the z-axis, due to the Lorentz equation $\vec{F} = q \cdot \vec{v} \times \vec{B}$, assuming the direction of the magnetic field in the middle of the iron plates is into the page in Fig 2.13, a μ^+ entering BabyMIND bends upward while a μ^- bends downward, until the muon reaches the upper and lower section of the iron plate, where the magnetic field is now having the opposite direction. The muon will then also bend towards the center of BabyMIND, confining more muon tracks for detection.

The scintillator planes are composed of vertical scintillator bars with dimensions of $1950\,\text{mm} \times 210.6\,\text{mm} \times 7.5\,\text{mm}$ and horizontal scintillator bars with dimensions of $2880\,\text{mm} \times 31.3\,\text{mm} \times 7.5\,\text{mm}$. Each of the horizontal and vertical scintillator planes are composed of 95 horizontal

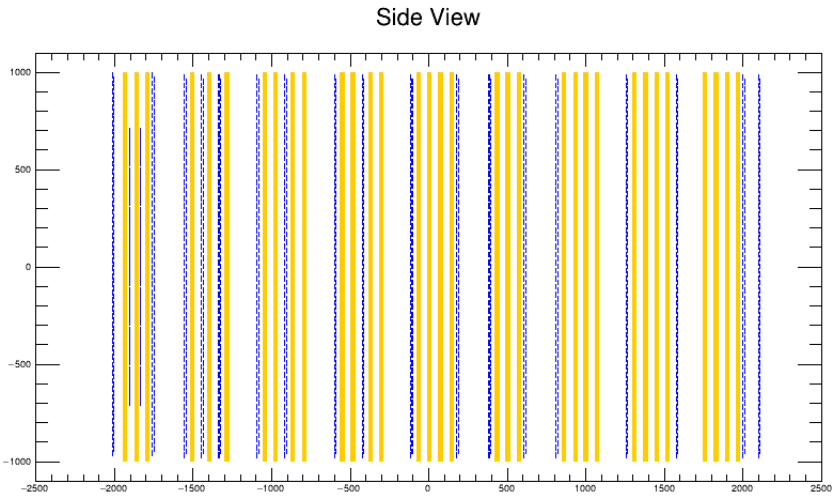

Figure 2.13: A side view of BabyMIND. The blue bars denote scintillators and the orange bars represent iron plates.

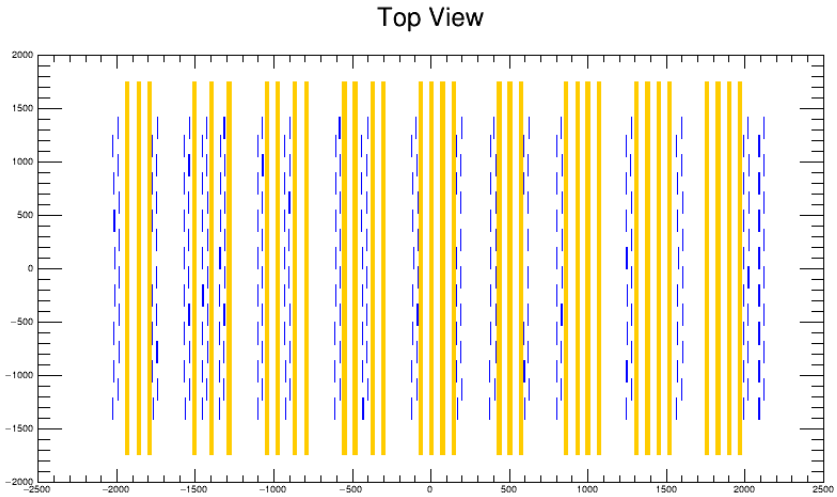

Figure 2.14: A top view of BabyMIND. The blue bars denote scintillators and the orange bars represent iron plates.

bars and 16 vertical bars respectively. The horizontal and vertical scintillator plane is shown in figures 2.13 and 2.14 respectively, denoted with blue bars. The resolution of data collected from the scintillator is determined by the width of the scintillator bar, as hits that are on any given location on a scintillator bar are all considered to have the same position value. Hits recorded in the horizontal bars, give the coordinates along the y-axis, giving the coordinates of the hits in the bending $y-z$ plane perpendicular to the magnetic field, while hits recorded in the vertical bars, give hits on the x-axis, so should follow a straight line along the $x-z$ plane. With such design, the x and y position of the hits are recorded separately using MPPCs at either end of the bars [51], and the hits recorded by the MPPCs are digitised in front-end electronics boards, and recorded by the data acquisition system.

The reason for narrower horizontal bars and the increase in number of horizontal plates is due to the need for higher resolution in the y-direction. As stated previously, the muon track after interaction will bend upwards or downwards along y-axis depending on the charge of the muon. As a result, it is expected that the change of y-position of the track is more important. Therefore a narrower bar provides higher resolution, and improves the precision of the data collected in the y-direction. Each complete scintillator plate is assembled into a module from two of each of the horizontal and vertical plates, with the two horizontal plates at the center of the module. To further increase the resolution of the complete scintillator plate, the horizontal and vertical plates are aligned such that the center of a bar in the plate overlays on top of the edge of the bar with the same direction, forming a zigzag pattern shown in figures 2.13 and 2.14. This can further improve the resolution by a factor of 2.

The MPPC, a type of silicon photomultiplier, is used in BabyMIND and is the same as the MPPC described in section 2.3 with dimensions of $2.625\,\text{mm} \times 2.1\,\text{mm} \times 0.85\,\text{mm}$ and with a photosensitive area of $1.3\,\text{mm} \times 1.3\,\text{mm}$ [52, 53]. The S13660 series is chosen for the experiment due to its high photon detection efficiency, low crosstalk and low dark current. These MPPCs are glued at the end of each scintillator bar, connected with the wavelength-shifting (WLS) optical fibres inside each of the scintillator bars. For the horizontal scintillator bars, the WLS fibres are inserted into narrow tubes that travel across the scintillator bars, detecting photons emitted when muons hit scintillators. For the vertical scintillator bars, the narrow tubes form a U-shape, starting and ending at the same side. This allows the WLS fibers to cover more of the wider vertical scintillator bars. The photon signals detected are transfered into the CITIROC readout system, which is a fully analogue ASIC designed for photosensors such as MPPC. The CITIROC reads in analog signals, and sends the signals to the analog-to-digital converters (ADCs) [52]. These readout systems are located at the end of scintillator bars, at the side of BabyMIND. The digital signals converted by ADCs are stored and analyzed.

There are also two extra scintillators inside the first iron module, one in between the first and second iron plates and one between the second and third iron plates. Each of the two scintillators are composed of 7 horizontal scintillator bars with a height of 20 mm. These extra scintillators

Scintillator position			
Scintillator index	z-position (mm)	Scintillator index	z-position (mm)
1	-2021.5	9	-429
yasu1	-1900	10	-122
yasu2	-1830	11	171
2	-1767	12	377
3	-1563	13	601
4	-1453	14	805
5	-1343	15	1250
6	-1101	16	1570
7	-923	17	1994
8	-608	18	2094

Table 2.1: Table of the z-position of the scintillators relative to the center of BabyMIND, where yasu1 and yasu2 are the two Yasu trackers. The z-positions given are at the center of the scintillator modules that consist of two horizontal and two vertical scintillator planes.

Iron position					
Iron index	z-position (mm)	Iron index	z-position (mm)	Iron index	z-position (mm)
1	-1930	12	-481	23	937
2	-1858	13	-369	24	1004
3	-1790	14	-300	25	1074
4	-1503	15	-62	26	1313
5	-1393	16	8	27	1383
6	-1283	17	78	28	1454
7	-1041	18	148	29	1521
8	-971	19	437	30	1760
9	-863	20	506	31	1833
10	-790	21	578	32	1902
11	-548	22	865	33	1971

Table 2.2: Table of the z-position of the center of the iron plates relative to the center of BabyMIND.

are called the Yasu trackers. The Yasu trackers are added inside the first iron module in order to obtain a better resolution for tracks with low momentum by allowing extra data points to be recorded between iron plates in the first module. The current layout is shown in Fig. 2.13 and 2.14. The relative positions of the scintillator and iron plates, as they were constructed and laid out in the B2 floor at J-PARC are described in tables 2.1 and 2.2.

Since BabyMIND is relatively new as a detector, there are limited simulation results focusing on BabyMIND. A main goal of this thesis is to simulate and reconstruct the neutrino interactions and the muon tracks formed by CCQE interactions inside BabyMIND. Due to the structure of BabyMIND, the magnetic field is not uniform in z and drops to zero inside the air gaps between plates, which makes the reconstruction not trivial. An aim of this thesis is to successfully reconstruct tracks in BabyMIND and calculate the reconstructed event yield via simulation, and then compare simulated results to experiment.

Chapter 3

Neutrino Beam Simulations of extended target

3.1 Neutrino beam Monte Carlo simulation

3.1.1 T2K standard neutrino beam simulation

T2K has already produced world-leading results, with the first observation of ν_e appearance in a long baseline experiment [54] and first hints of CP violation in neutrino oscillations [29]. Improvements in the physics programme of T2K rely on upgrades to both the beam and the detector systems in ND280. One possible upgrade being considered is an extension of the neutrino target inside the first horn, to increase the muon neutrino flux and decrease the contamination in the beam from antineutrinos in forward-horn current (FHC) or increase the antineutrino flux and decrease the neutrino flux in the reverse-horn current (RHC) configuration. Such a reduction of the "wrong sign" flux is particularly important when hunting for CP violation as it makes the observable signal stronger. This chapter is dedicated to the study of such modifications to the neutrino target, to quantitatively determine the potential benefits to the experiment of such an upgrade.

The JNUBeam package [44], developed by the T2K researchers, is a neutrino beam simulation package that reads input files generated by FLUKA (a simulation package that calculates the transport and interaction of particles with matter) [55], and uses the information in the files to generate neutrino fluxes from different proton beam settings. With JNUBeam it is also possible to generate neutrinos from hadron decays produced by the GCALOR hadron package embedded in the JNUBeam package. It is tuned for the T2K secondary beamline settings, and multiple options, such as the momentum of the proton beam and the direction of the current for the horn, are available for change.

This thesis utilizes the JNUBeam package alongside the official FLUKA input files generated by T2K researchers to simulate the flux of neutrinos and antineutrinos. The JNUBeam pro-

gramme is written based on the GEANT3 Monte-Carlo simulation package, an interaction event generator written in 1987 to study detectors, to develop reconstruction programmes and to interpret experimental data [56]. To reduce the uncertainties of the flux generated from JNUBeam, the NA61/SHINE data is used to reweight and constraint the neutrino flux uncertainties. The application of the NA61/SHINE data in 2009 reduced the flux uncertainties to 5%, from 10% for the previous runs [57].

There are different ideas on how to improve the performance of the T2K experiment, and one direction is to improve the target and the magnetic horn located at the secondary beamline. As demonstrated in Fig. 2.4, the 91.4 cm graphite rod is inserted into the upstream section of the first magnetic horn at the secondary beamline as a target. As the neutrino yield is related to the number of target nucleons, a target with higher volume increases the number of neutrinos produced. While the optimal case would be to have a target with a length matching the inner part of the first magnetic horn, it is physically impossible, as the long target will be bent due to gravity. While it is possible to improve this design, it would be necessary for the beamline to be shut down. Since any upgrade to the beamline will be costly and will require careful engineering, especially in a high radiation area, it is imperative to understand the physics benefits of upgrading the neutrino target. As a result, it is necessary to simulate the effect of every potential target upgrade design on the performance of the T2K experiment. As there is a need to improve the performance of the beam, simulations of the beam with different settings are performed in this thesis, and suggestions based on the simulation results are given to researchers building the upgrade for the target horn in the beam.

3.1.2 Results from simulations at 2.5 degrees

A simulation of the well-studied ND280 neutrino beam flux can be the basis for other simulations that are less well understood. If the simulation is working as intended, it is expected that a muon-neutrino flux should peak at 600 MeV, as shown at the left of Fig. 3.1. The JNUBeam generated neutrino flux result shows a similar result compared to the T2K official release, which is as expected and shows that the JNUBeam code works as intended.

This result is generated with the following settings that can be modified freely. Using GCALOR to generate the interaction parameters, the position of the beam is at the center of the horn. The beam energy used in all the following plots and data is 30 GeV, and the distance between the horn and the detectors is 280 m. Most of these variables are global, regardless of the beam off-axis angle. The beam is set to emit protons at the center of the baffle, which is at the upstream of the target.

The muon-neutrino flux generated by the JNUBeam package uses the forward horn current (FHC) setting, which means that the current-induced magnetic field in the first magnetic horn is clockwise, favoring the production of neutrino flux over antineutrino flux. The favored type of neutrino flux is defined as the right-sign (RS) neutrino flux, where the other type of neutrino

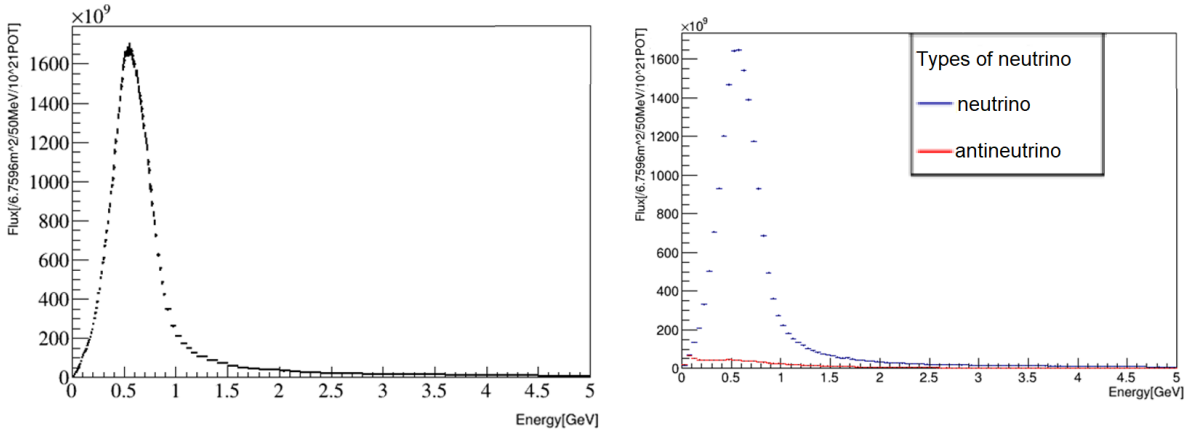

Figure 3.1: A comparison of the forward horn current neutrino flux between the official release from T2K and the flux plot generated by JNUBeam code run by the author for this thesis, with the official release at the left and the JNUBeam generated flux plot at the right.

flux is the wrong-sign (WS) neutrino flux. The wrong-sign ratio (WSR) between the two types of neutrino fluxes is as follows:

$$WSR = \frac{\int \nu_{\mathrm{WS}}(E)dE}{\int \nu_{\mathrm{RS}}(E)dE}, \tag{3.1}$$

where $\nu_{WS}(E)$ is the wrong-sign neutrino flux and $\nu_{RS}(E)$ is the right-sign neutrino flux. The wrong-sign flux is also known as the wrong-sign contamination. As a result, the WSR is a necessary value that demonstrates the percentage of wrong-sign contamination, and also provides a common ground for comparisons between different configurations of the horn on the performance of the beam. Therefore, in a perfect case the WSR is 0, and an upgrade of T2K should minimize WSR as the goal is to have as little wrong-sign flux as possible. The 'flux' here is $\frac{N}{AbPOT}$, where N is the number of neutrinos, A is the area of the detector ($6.7596\,\mathrm{m}^2$ for ND280), b is the bin size chosen (50 MeV in this thesis), and POT is the number of protons-on-target (in units of 10^{21} POTs). Since the WSR is determined by two integrals of flux, the WSR is dependent on the range of the energy selected.

For future calculations of WSR, the range of energy is chosen to be $0.2-1.5\,\mathrm{GeV}$, as this is a region where most of the neutrino interactions occur in ND280 and WAGASCI. The FHC neutrino and antineutrino fluxes within such a region is demonstrated in Fig. 3.2. The neutrino flux is the right-sign flux (blue) and the antineutrino is the wrong-sign flux (red) on the left of Fig. 3.2. The wrong-sign ratio plot for the flux distribution on the right of Fig. 3.2 also demonstrates that the FHC produces a neutrino beam that has the least wrong-sign contamination at 600 MeV, which is the peak distribution for the beam with a beam off-axis angle of 2.5°. Within this region, the neutrino flux in Fig. 3.1 has a $WSR = 0.0453$. If a reverse horn current (RHC) is present instead, as shown in Fig. 3.3, then the $WSR = 0.0669$. Table 3.1 shows the fluxes and the wrong-sign ratio for the neutrino beam with a beam off-axis angle of 2.5°.

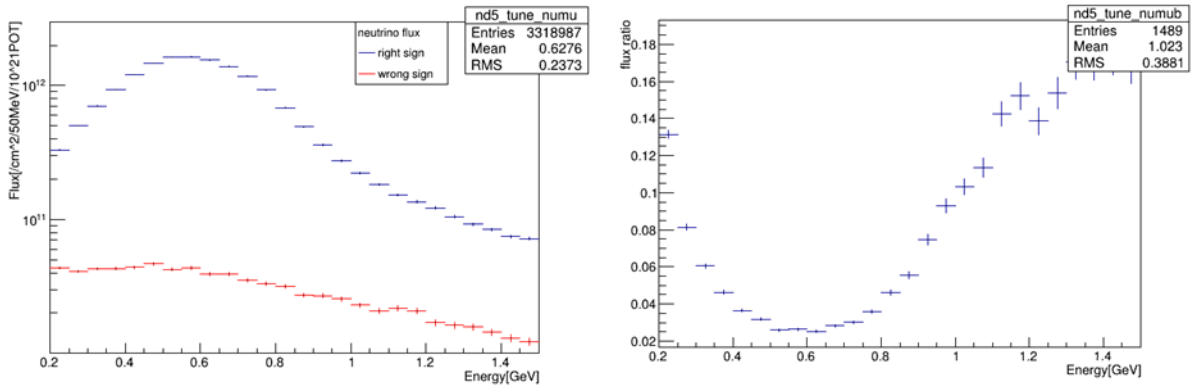

Figure 3.2: The neutrino and antineutrino flux for FHC between $0.2-1.5\,\text{GeV}$ is demonstrated on the left, with a logarithmic scale on the y-axis, and on the right is the ratio of the antineutrino flux bins (wrong-sign) over the neutrino flux bins (right-sign), thus a plot of WSR is produced.

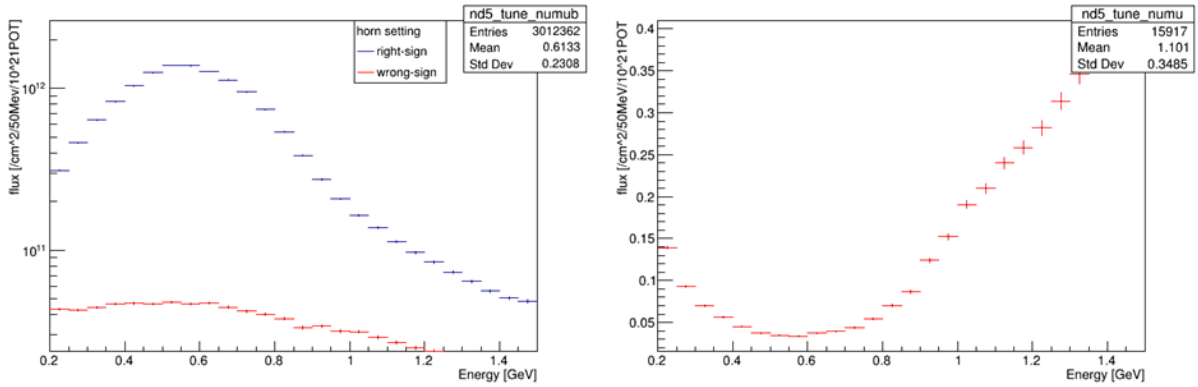

Figure 3.3: The neutrino and antineutrino flux for RHC between $0.2-1.5\,\text{GeV}$ is demonstrated on the left, with a logarithmic scale on the y-axis, and on the right is the ratio of the neutrino flux bins (wrong-sign) over the antineutrino flux bins (right-sign).

Parameters and results for current T2K horn setting			
	right-sign flux $(/6.7596\,\text{m}^2/10^{21}\,\text{POT})$	wrong-sign flux $(/6.7596\,\text{m}^2/10^{21}\,\text{POT})$	wrong-sign ratio
FHC	1.661×10^{13}	7.523×10^{11}	0.0453
RHC	1.370×10^{13}	9.162×10^{11}	0.0669

Table 3.1: Table of the right-sign and wrong-sign flux for FHC and RHC neutrino beam with a 2.5° angle, with the wrong-sign ratio on the right.

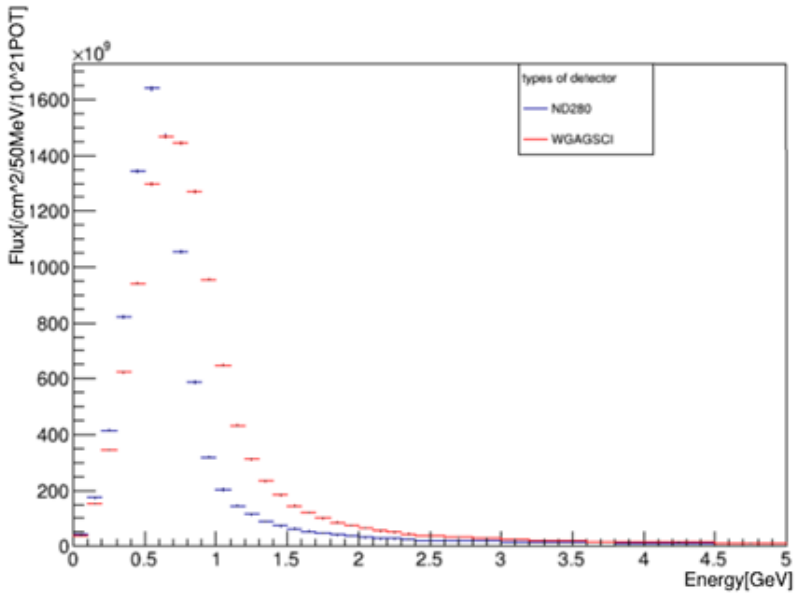

Figure 3.4: A comparison of the forward horn current muon-neutrino flux generated by JNUBeam with the flux distribution for ND280 denoted blue (2.5°) and the flux distribution for WAGASCI denoted red (1.5°).

As shown in table 3.1, the RHC generates neutrino beams with a lower right-sign flux yield, a higher wrong-sign yield and a higher WSR, which shows that the performance of FHC is better than RHC in the current T2K horn settings. This means the production of muon-neutrinos through FHC is more efficient than the production of muon-antineutrinos. Such a relationship is expected, given that positive protons incident on a target are more likely to produce positive pions, and should remain when the geometry of the first magnetic horn is modified in the simulation.

3.1.3 Results from simulations at 1.5 degrees

While ND280 has a beam off-axis angle of 2.5°, the WAGASCI-BabyMIND has a different beam off-axis angle of 1.5°, causing the flux to have different peak. It is expected that the peak for a beam off-axis angle of 1.5° is around 800 MeV. To compare the difference of the flux distribution due to the beam off-axis angle, two simulations are performed, with neutrinos in one of the simulation aiming toward ND280 (2.5°) and neutrinos in the other simulation aiming towards WAGASCI (1.5°). Fig. 3.4 demonstrates the flux distribution of these two settings. It is shown that the flux distribution for 1.5° has a lower peak flux distribution, as well as a wider spread that peaks at 800 MeV. This means that the muon-neutrino beam passing through WAGASCI and BabyMIND has a higher energy on average, and we should expect that most of the muon-neutrinos interacting in WAGASCI and BabyMIND have an energy around 800 MeV, higher than that of the neutrinos interacting in ND280.

For the remainder of the chapter, the effect of the change of flux due to modifications of the neutrino target will be carried out with respect to the ND280 flux at 2.5° angle, which is also the angle to Super-K, and is therefore selected as the reference flux for comparison.

3.2 Neutrino beam simulations with an extended target

3.2.1 Extended target motivation

A neutrino beam, as discussed in section 2.2.2, is generated when the accelerated protons from the primary beamline travel and interact with the carbon nuclei in the target. As a result, the more nuclei there are in the target, the larger the neutrino yield should be. Moreover, it is expected that the wrong-sign contamination, which comes mostly from particles that do not enter the magnetic fields of the horns, will decrease as the length of the target increases. A theoretically trivial solution on increasing the yield of the right-sign neutrinos is by extending the graphite target such that the target fills neck of the first magnetic horn. However, this solution is physically very difficult as the target is not rigid enough to remain straight over the full length of the horn.

The current graphite target is tested such that the current length is constrained to prevent deformation due to gravity. In the design of the target, as shown in Fig. 2.5, the target rod is attached to the magnetic horn via a support structure at the upstream end of the first magnetic horn. If the length of the target rod is extended, the lack of support on the other side may cause the pivot point of the rod to be around the support. This means that the gravitational force acting on the far end of the rod will have a greater impact, which will cause a deformation to the rod if the rod is extended far enough.

Another constraint on the target is the deformation of the materials due to fluctuating temperatures. When protons interact with the target to create secondary hadrons, the amount of heat generated by radiation from the interaction is high enough for some of the materials to deform, or even melt. Therefore, a suitable material in reality must require a good heat resistance, and also a low density to maximise the yield of secondary hadrons escaping the target.

A solution proposed by our collaborators is to insert another target of some material into the downstream end of the first magnetic horn, and to fill most of the horn, leaving only a small air gap between the two targets. In the simulation, a 65 cm graphite rod is inserted from the downstream end of the first horn. A diagram of such a modification is shown in Fig. 3.5. A JNUBeam simulation was run after the modification, and the neutrino flux distributions for the FHC and the the RHC configurations were calculated, and the WSR was determined and compared to the current T2K value.

Since the new target at the downstream end of the first horn is not yet installed, there is freedom to choose the material used on the target. Besides graphite, which is the target material

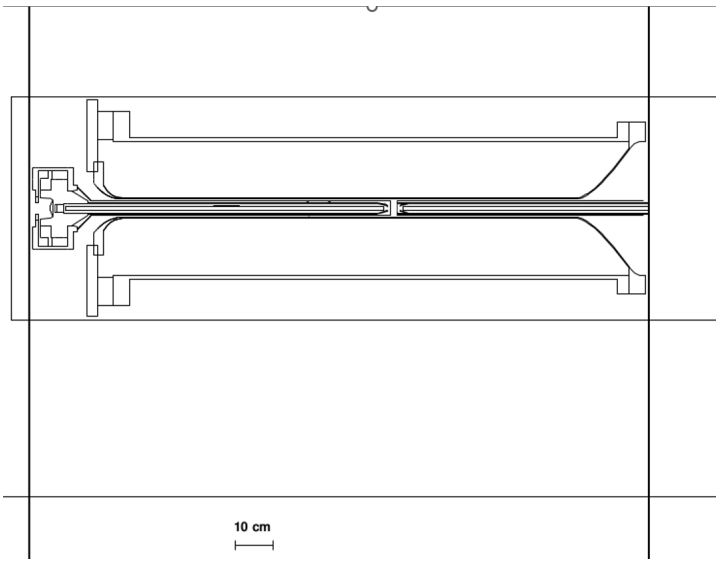

Figure 3.5: A JNUBeam generated graph of the side view of the first magnetic horn with an extra graphite rod inserting from the downstream horn.

used in T2K, other materials are considered. Silicon carbide (SiC) has similar properties to graphite but is about 50% denser, and is already in development for J-PARC Materials and Life-Science Facility (MLF) [58]. The high heat resistance alongside with its same neutron/proton ratio as graphite makes the material a good candidate for the target. Another material that the collaborators were interested in studying is boron carbide (B_4C), which is the compound with the highest density for the longest radiation length. One other material to be considered is a metal with a higher atomic number (Z) and atomic mass (A) value. In this thesis, titanium is chosen simply because this material is already used in the construction of the target. With an atomic number $Z = 22$, this material is used to determine whether a higher-Z material improves the performance of this target, excluding any physical limitations that titanium may have.

As part of the study of the material properties of the extra target, we looked at changing the atomic number Z and the density, to understand the effects of these two parameters independently. For this reason, we tried out different materials and density, such as titanium with nominal and half its density, or nickel (with an atomic number $Z = 28$) at half its density, such that the nickel has a similar density compared to titanium with nominal density. A variable density target can be achieved by containing pellets of the material and packing them with more or less spacing between pellets to achieve the required density. One other experimental modification is a graphite rod with a changing density.

Another possible direction for upgrading the target is by changing the shape of the target, and by changing the shape of the rod while still allowing the target to be able to be inserted in the downstream section of the horn, therefore achieving a graphite target with changing density. For simplicity, the graphite target used in this experiment is a combination of a tube and a rod with half the radius of the original target that, when combined, forms the same shape as a regular

graphite target. However, the graphite tube has half of the density of carbon, which creates a simple graphite target with changing density.

All of the tests on materials and the experimental simulations are performed with FHC and RHC. The goal is to discover the best material that has the most beneficial impact to the wrong-sign contamination. The simulations of the extended target with different materials, aims to determine the correlation between atomic number and density with the wrong-sign contamination.

3.2.2 Results of extended target simulations in FHC configuration

For the forward horn current, similar plots to Fig. 3.2 are produced and compared with an extra graphite target inserted at the downstream end of the first horn. Fig. 3.6 demonstrates the superposition between Fig. 3.2 and a similar plot, generated with the same method but with an extra graphite target downstream of the first magnetic horn. It is shown that the yield of the right-sign flux increases while the yield of the wrong-sign flux decreases. This is an expected result, and proves that inserting an extra graphite target at the downstream end of the original target does improve the performance of the beam by both increasing the right-sign yield and decreasing the wrong-sign contamination. The extra material in the target means that more π^+ and π^- are created. The extra π^+ created are then focused in the second and third horn (for FHC) and the π^- are defocused (and vice versa for RHC). So, the net effect is that there is an increase in right-sign pions and a decrease in wrong-sign pions. A comparison of the WSR with and without the extra graphite target is demonstrated on the left in Fig. 3.7. It is shown that the extra downstream target lowers the WSR in every bin, with a better effect for high energies above 1 GeV. On the right of Fig. 3.7 there is the ratio of the two WSR (RWSR) plots, where,

$$\mathrm{RWSR} = \frac{\mathrm{WSR_{Target}}}{\mathrm{WSR_{T2K}}}. \tag{3.2}$$

Equation 3.2 is valid for energy-dependent fluxes and the WSRs shown in the figures, and also the integrated flux WSRs that are shown in tables 3.1 and 3.2. The RWSR is a figure of merit that identifies the decrease in the WSR from the extended target, based on the simulation results from the current T2K setting demonstrated in Fig. 3.2. However, as shown in table 3.2, the existence of an extra target also increases the right-sign yield. This improvement is also included into the final figure of merit, by introducing the right-sign ratio (RSR) that is defined as:

$$\mathrm{RSR} = \frac{\int \nu_{\mathrm{RS(material)}}(E)dE}{\int \nu_{\mathrm{RS(T2K)}}(E)dE}. \tag{3.3}$$

By dividing RWSR with respect to RSR, the effect of the increase of the right-sign fluxes is included and thus the final ratio (FR) is used to compare the total improvement from the extra targets with different materials with respect to the current T2K horn setting without any extra

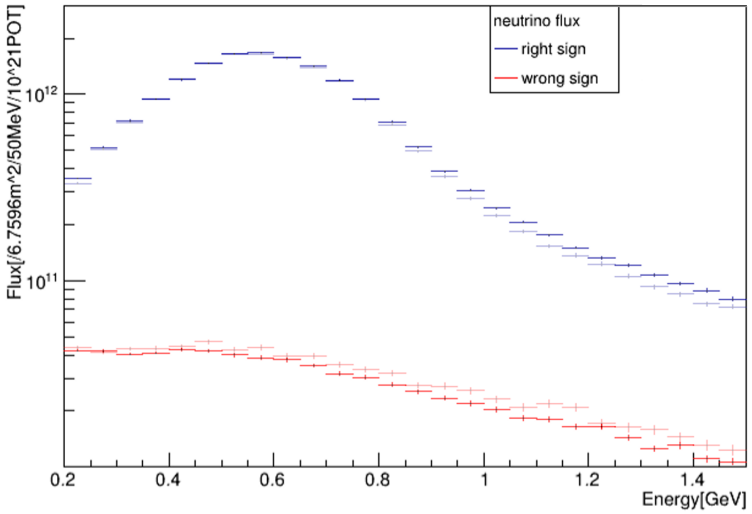

Figure 3.6: A comparison between the neutrino fluxes shown in Fig. 3.2, and a similar plot that is produced with an extra graphite target downstream with the FHC neutrino beam configuration. The lighter points are the fluxes from the current T2K target and the darker points are the fluxes from the configuration that includes an extended graphite target.

targets, that is,

$$\mathrm{FR} = \frac{\mathrm{RWSR}}{\mathrm{RSR}}, \tag{3.4}$$

and its value should be minimized for optimizing the target design.

The simulation result of the materials (graphite, silicon carbide, boron carbide and titanium) are shown with the figures-of-merit mentioned above in table 3.2, and their WSR plots with respect to the current T2K beam setting, alongside with the RWSR plots are shown in Fig. 3.7 and Fig. 3.8. The goal is to make the FR figure-of-merit as small as possible, thus reducing the wrong-sign contamination and increasing the right-sign flux. From table 3.2, while considering the increase of right-sign flux and the decrease of wrong-sign contamination, the extra graphite target improves the comprehensive performance by 10%, while silicon carbide, boron carbide and titanium improves the performance by 15%, 12% and 20% respectively.

If only simulated results are considered, titanium has the best performance as a high Z and high density element, and silicon carbide follows. However, titanium has low heat conductivity, which makes it difficult to make a solid target out of this material to withstand high thermal shock. A lower density titanium target is possible, if it is made out of pellets. However, silicon carbide has excellent heat conductivity and has the best performance out of the remaining materials. So, even though titanium has the best performance, silicon carbide shows the best compromise between good material properties to build a solid extra target out of the four considered, while still giving a 15% improvement in performance for FHC.

Besides the four materials demonstrated above, changes to the density of certain elements are performed to investigate the correlation between the atomic number and the density, and the

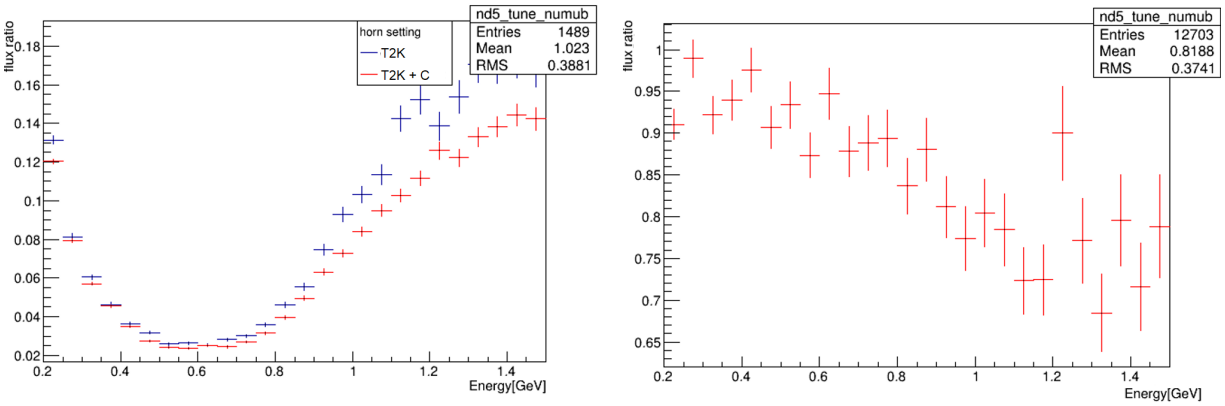

Figure 3.7: The WSR plots of the neutrino flux generated with (red data points) and without (blue data points) the downstream graphite target on the left, and the ratio of the two WSRs, the modified setting over the current T2K setting on the right for the FHC neutrino beam configuration.

wrong-sign ratios and figures-of-merit for comparison w.r.t the current T2K horn settings (FHC)				
Materials	Graphite	Silicon carbide	Boron carbide	Titanium
Density (g/cm^3)	1.806	3.16	2.52	4.54
RS integrated flux ($/6.7596\,m^2/10^{21}$ POT)	1.7224×10^{13}	1.7131×10^{13}	1.7124×10^{13}	1.666×10^{13}
WS integrated flux ($/6.7596\,m^2/10^{21}$ POT)	7.2813×10^{11}	6.8363×10^{11}	6.9959×10^{11}	6.0863×10^{11}
wrong-sign ratio	0.0423	0.0339	0.0409	0.0365
Ratio of WSR	0.933	0.881	0.902	0.807
right-sign ratio	1.0369	1.0312	1.0308	1.0027
Final ratio	0.9003	0.8546	0.8752	0.8046

Table 3.2: Table of wrong-sign ratios and other figures-of-merit used to compare the effect of an extended target with different materials with respect to the nominal T2K target.

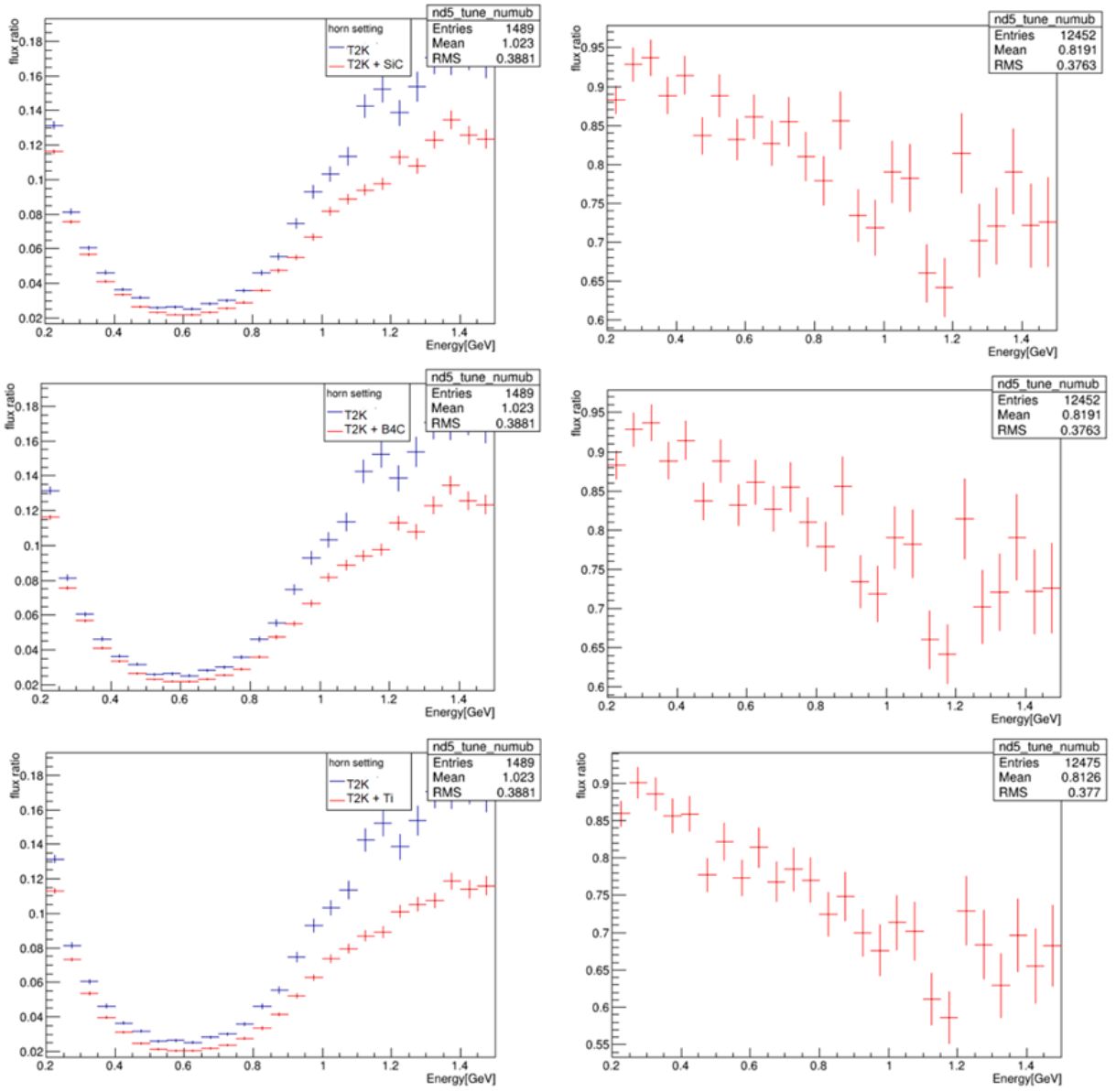

Figure 3.8: The WSR plots (left) and RWSR (right) plots for silicon carbide (top), boron carbide (middle) and titanium (bottom) respectively for the FHC neutrino beam configuration.

performance of the extra targets made by these modifications. Fig. 3.9 and table 3.3 show the figures-of-merit for the extra extended target materials considered. The simulations show that, when comparing to the titanium listed in table 3.2, decreasing the density (titanium with half of the density) raises the final ratio, meaning that for the same material, the performance is better as the density goes up. However, increasing the atomic number (nickel with half of the density to match the density of titanium) also raises the final ratio, which shows that for elements with similar density, it may be better to pick a material with lower atomic number.

Another extended target simulation that was carried out was to construct a graphite target that has an outer region and an inner region, where the outer region is made of graphite with half of the density. This is a simple way to simulate a graphite target with modified geometry, such as a spiral shaped rod that has a lower mean density on the outer region of the target. The results of such simulations are also shown in Fig. 3.9 and table 3.3. The result follows the previous analysis of the effect of density on the performance of the extra target. The two-densities graphite target performs worse than the extended, normal density graphite target, gaining only 4% improvement from 10%. A summary of all the final ratios for all the materials considered that make up the extended target discussed is shown in Fig. 3.10.

An interesting result is that the nickel target and the graphite target with two-densities have a RSR < 1, which means these two extra targets will decrease the yield of right sign neutrinos. This is an example of why simulations have to be conducted with different materials of interest before deciding the material to be used in the upgrade. There are two competing effects: a higher density material increases the production of pions, but if the density is too high, the pions cannot escape the target. While the density of the nickel target is halved such that the density of the target is close to the titanium target in table 3.2, the high atomic mass alongside the high density cause the pions to be absorbed, thus lowering the right-sign neutrino yield. The carbon target has the opposite issue compared to the nickel target where the density of the carbon target is too low. In this case, not enough neutrinos are produced through such a low density target and thus the target may have negligible effect on neutrino production. The slight difference on the RS flux is probably due to statistical fluctuations. These two examples show that the material selection for the extra target is not trivial, as a material with a density either too high or too low may both produce unintended RS flux yields.

In reality, the extra target shown in Fig. 3.5 needs a supporting structure at the downstream part of the horn to hold the extra target and provide coolants for the target. As a result, a simple titanium disk with a thickness of 4 mm is constructed in the simulation as a simplified version of the structure, shown in Fig. 3.11. The thickness would be sufficient to hold this target but it has not been engineered. The point of the study is to see what is the effect of the holder on the target performance, to demonstrate any loss in performance that arises from such a structure. It is expected that the material in the supporting structure for the target will reduce the performance of the extra target.

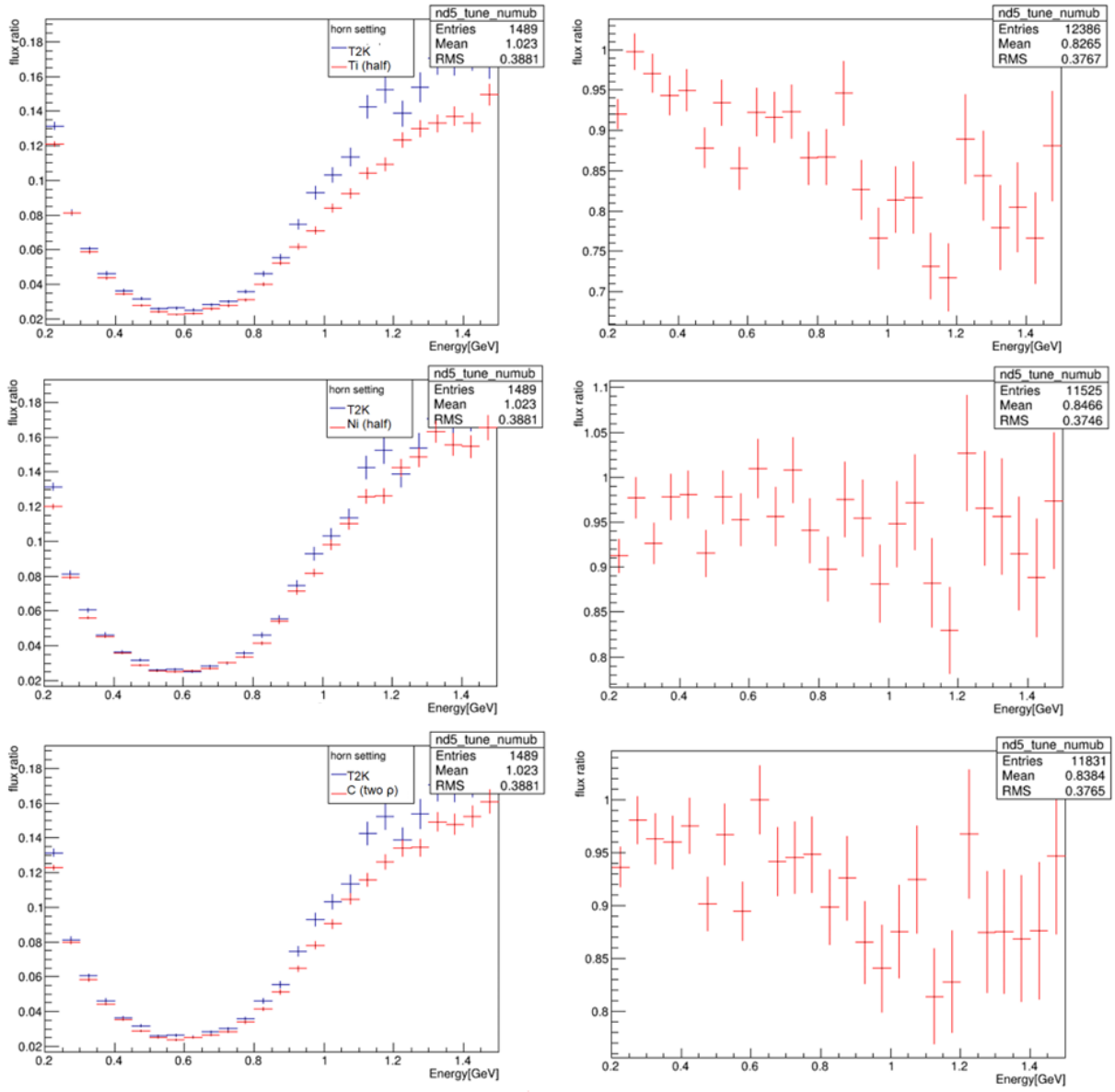

Figure 3.9: The WSR plots (left) and RWSR plots (right) for titanium with half the density (top), nickel with half the density (middle) and graphite with a target containing two densities (bottom) respectively for the FHC neutrino beam configuration.

wrong-sign ratios and figures-of-merit for comparison w.r.t the current T2K horn settings (FHC)			
Materials	Titanium	Nickel	Graphite (two densities)
Density (g/cm^3)	2.27	4.454	1.806 and 0.903
RS integrated flux ($/6.7596\,m^2/10^{21}$ POT)	1.7182×10^{13}	1.6446×10^{13}	1.6570×10^{13}
WS integrated flux ($/6.7596\,m^2/10^{21}$ POT)	7.1061×10^{11}	7.3323×10^{11}	7.1957×10^{11}
wrong-sign ratio	0.0414	0.0446	0.0434
Ratio of WSR	0.913	0.985	0.959
right-sign ratio	1.0343	0.9900	0.9975
Final ratio	0.8830	0.9945	0.9614

Table 3.3: Table of wrong-sign ratios and other figures-of-merit used to compare the effect of an extended target with different materials of varying densities with respect to the nominal T2K target.

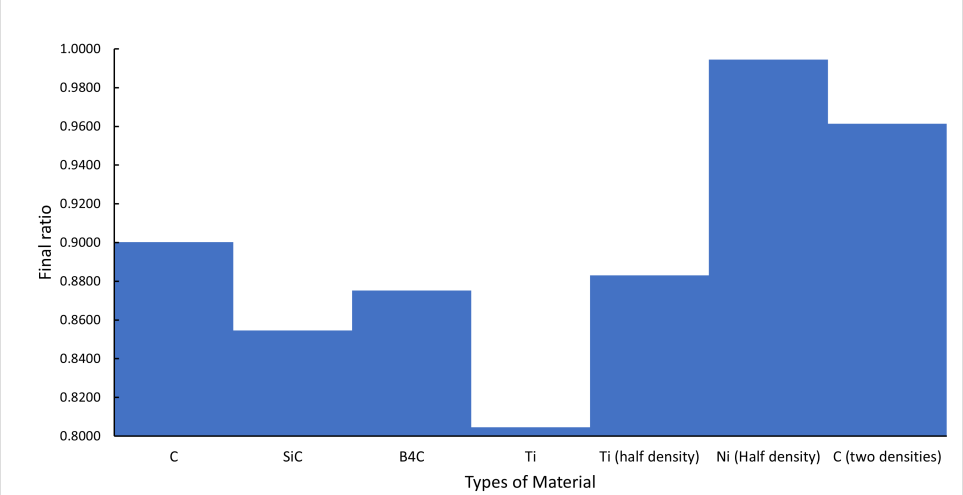

Figure 3.10: The final ratio comparison of the extra target made with different materials for the FHC neutrino beam configuration.

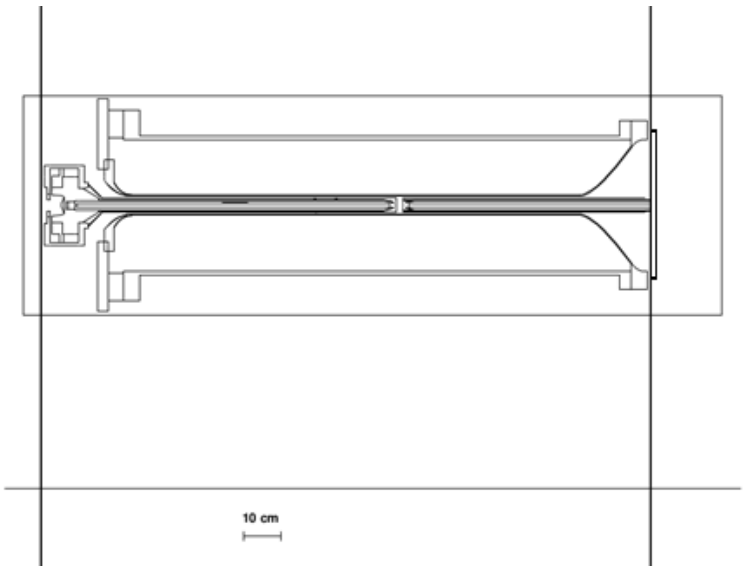

Figure 3.11: The side view of the first magnetic horn with the extra graphite target and a titanium disk representing the support structure. The scale of the disk is exaggerated for ease of understanding.

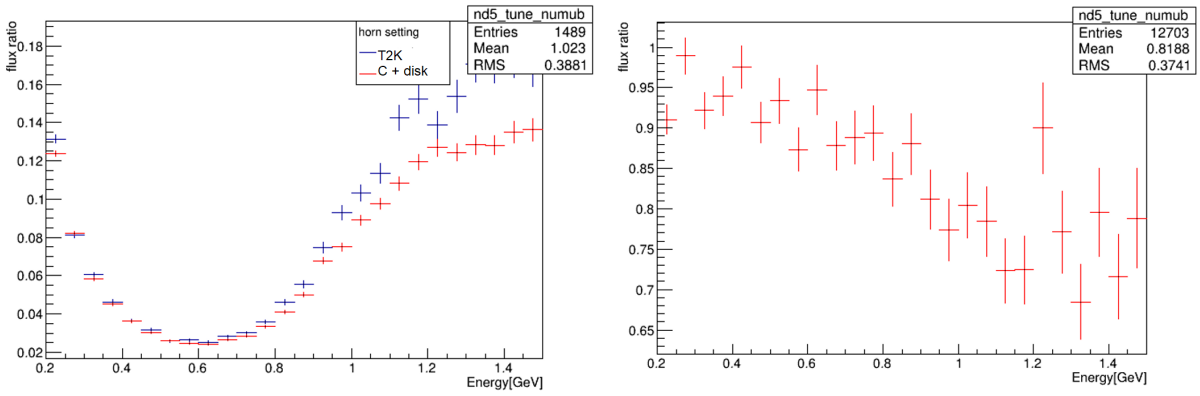

Figure 3.12: The WSR plots (left) and RWSR plots (right) for the FHC neutrino beam configuration with an extra graphite target and an extra titanium disk to simulate the target holder.

The simulated WSR and RWSR plots, as well as the figures-of-merit are shown in Fig. 3.12 and table 3.4. The final ratio of the target with a support disk is lower than the final ratio of just the graphite target shown in table 3.2. This suggests that for FHC, the existence of any support structures lower the effectiveness of the extra target inserted at the downstream end of the horn. It is important, when designing the extra target for the T2K upgrade, that the amount of material used to build the support structure should be minimized and that the support structure is taken into account when evaluating a realistic design.

3.2.3 Results of extended target simulations in RHC configuration

The simulations and analyses made in section 3.2.2 are also carried out with the RHC configuration, where the antineutrino fluxes are the right-sign fluxes. The figures of merit for the four

wrong-sign ratios and figures-of-merit w.r.t the current T2K horn settings (FHC)	
Materials	Graphite with titanium support
RS integrated flux ($/6.7596\,\mathrm{m}^2/50\,\mathrm{MeV}/10^{21}\,\mathrm{POT}$)	1.686×10^{13}
WS integrated flux ($/6.7596\,\mathrm{m}^2/50\,\mathrm{MeV}/10^{21}\,\mathrm{POT}$)	7.200×10^{11}
wrong-sign ratio	0.0427
Ratio of WSR	0.9432
right-sign ratio	1.01
Final ratio	0.9294

Table 3.4: Table of wrong-sign ratios and other figures-of-merit used to compare the effect of an extended graphite target with an extra titanium support for the FHC neutrino beam configuration.

materials are demonstrated in Fig. 3.13 and table 3.5, and for the extra extended target materials considered, the figures of merit are shown in table 3.6.

From the summary plot on the final ratio of materials with RHC in Fig. 3.14, and comparing this summary to Fig. 3.10 that shows the final ratio of materials with FHC, the general conclusion is that the trend in the FHC and RHC results for each material seem to be quite consistent. However, from the summaries, it is shown that the extra target downstream has a better effect on improving the performance of the beam in RHC. What are shown in Fig. 3.10 and table 3.3 is that the titanium target, with a relatively low atomic number (compared with nickel) has the best performance on reducing the wrong-sign contamination and increasing the right-sign yield, regardless of the direction of the current in the magnetic horn. However, as discussed in section 3.2.2, the thermal properties of titanium preclude building a solid titanium target. Meanwhile, silicon carbide, with a low density and high heat conductivity, shows the best performance excluding titanium, which makes silicon carbide the best realistic material candidate, with 15% improvement in FHC and 19% improvement in RHC.

The extra support structure also has the same effect for RHC compared with the effect for FHC. A design for the support part of the target is recommended to use as little material as possible, as the material in the target support will increase the final ratio, decreasing the performance of the extra target. All of the simulation results and details of the analysis, alongside with recommendations made based on these results, have been given to our engineering collaborators, who are responsible for evaluating, designing and installing such a neutrino target update in the future.

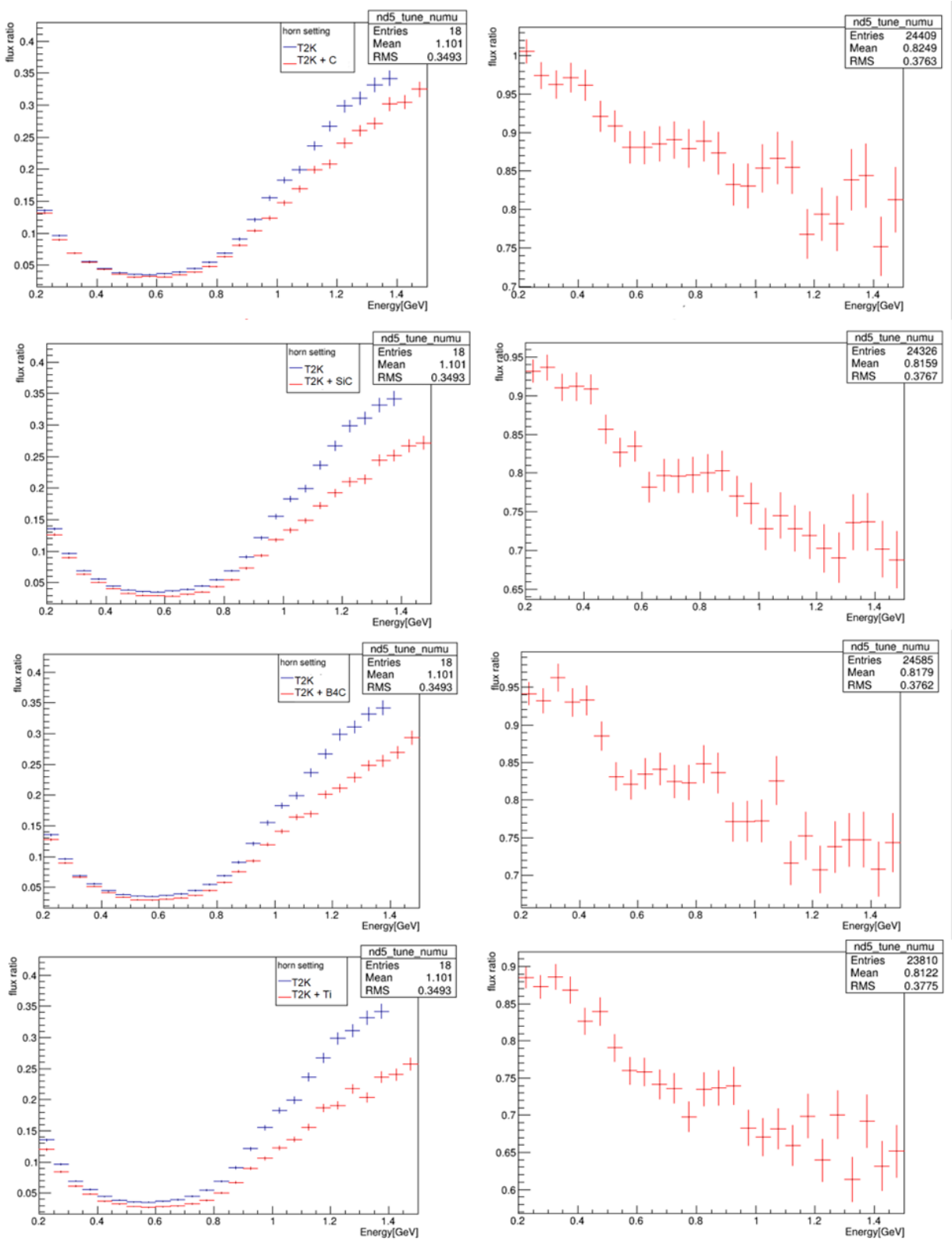

Figure 3.13: The WSR plots (left) and RWSR plots (right) for graphite (top), silicon carbide (second row), boron carbide (third row) and titanium (bottom) respectively for the RHC neutrino beam configuration.

wrong-sign ratios and figures-of-merit for comparison w.r.t the current T2K horn settings (RHC)				
Materials	Graphite	Silicon carbide	Boron carbide	Titanium
Density (g/cm^3)	1.806	3.16	2.52	4.54
RS integrated flux ($/6.7596\,m^2/50\,MeV/10^{21}\,POT$)	1.421×10^{13}	1.419×10^{13}	1.422×10^{13}	1.377×10^{13}
WS integrated flux ($/6.7596\,m^2/50\,MeV/10^{21}\,POT$)	8.686×10^{11}	7.970×10^{11}	8.217×10^{11}	7.156×10^{11}
wrong-sign ratio	0.0611	0.0562	0.0578	0.0520
Ratio of WSR	0.9162	0.8400	0.8640	0.7773
right-sign ratio	1.037	1.0354	1.03079	1.005
Final ratio	0.8817	0.8112	0.8325	0.7735

Table 3.5: Table of wrong-sign ratios and other figures-of-merit used to compare the effect of an extended target with different materials with respect to the nominal T2K target for the RHC neutrino beam configuration.

wrong-sign ratios and figures-of-merit for comparison w.r.t the current T2K horn settings (RHC)			
Materials	Titanium	Nickel	Graphite (two densities)
Density (g/cm^3)	2.27	4.454	1.806 and 0.903
RS integrated flux ($/6.7596\,m^2/50\,MeV/10^{21}\,POT$)	1.420×10^{13}	1.355×10^{13}	1.3670×10^{13}
WS integrated flux ($/6.7596\,m^2/50\,MeV/10^{21}\,POT$)	8.443×10^{11}	8.929×10^{11}	8.7277×10^{11}
wrong-sign ratio	0.0594	0.0659	0.0638
Ratio of WSR	0.889	0.986	0.949
right-sign ratio	1.0361	0.9886	1.0006
Final ratio	0.8582	0.9970	0.9483

Table 3.6: Table of wrong-sign ratios and other figures-of-merit used to compare the effect of an extended target with different materials of varying densities with respect to the nominal T2K target for the RHC neutrino beam configuration.

wrong-sign ratios and figures-of-merit w.r.t the current T2K horn settings (RHC)	
Materials	Graphite with titanium disk
RS integrated flux ($/6.7596\,m^2/50\,MeV/10^{21}\,POT$)	1.3926×10^{13}
WS integrated flux ($/6.7596\,m^2/50\,MeV/10^{21}\,POT$)	8.578×10^{11}
wrong-sign ratio	0.06143
Ratio of WSR	0.9187
right-sign ratio	1.019
Final ratio	0.9015

Table 3.7: Table of wrong-sign ratios and other figures-of-merit used to compare the effect of an extended graphite target with an extra titanium disk for the RHC neutrino beam configuration.

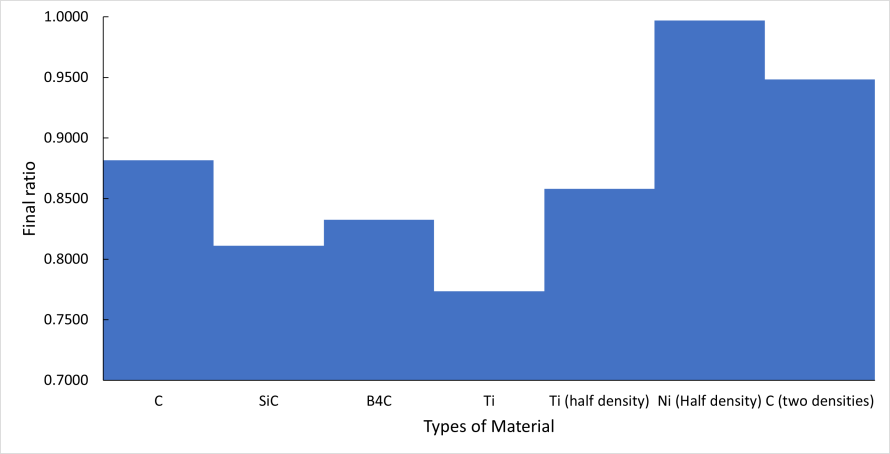

Figure 3.14: The final ratio comparison of the extra target made with different materials for the RHC neutrino beam configuration.

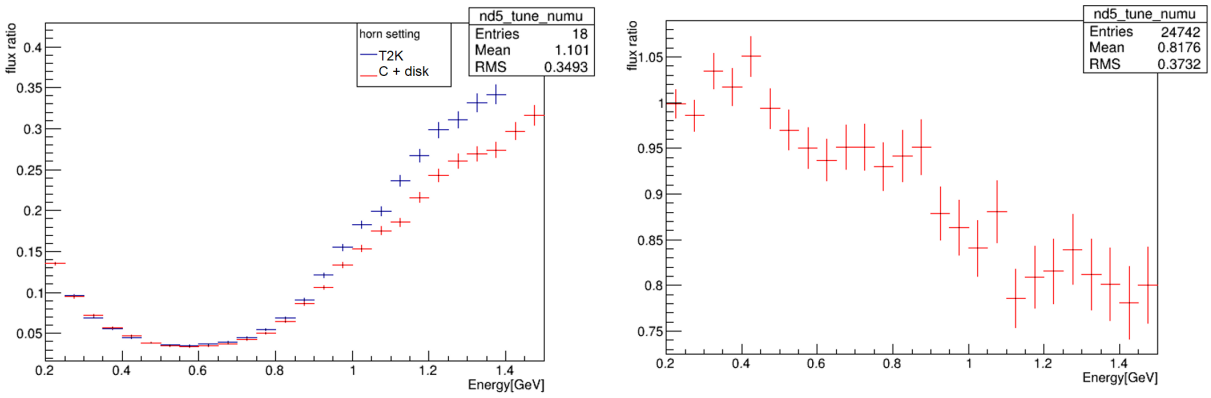

Figure 3.15: The WSR plots (left) and RWSR plots (right) for the RHC neutrino beam configuration with an extra graphite target and an extra titanium disk to simulate the target holder.

Chapter 4

Neutrino interactions in BabyMIND

4.1 Motivation for measuring neutrino interactions in the iron of BabyMIND

The only way a detector distinguishes incoming neutrinos from antineutrinos is by detecting the product of the neutrino interactions. As stated in section 1.3.4, since the majority of the neutrinos and antineutrinos produced from the T2K beamline have a relatively low energy, the neutrino interactions that T2K expect are CCQE and CCRES interactions, implying that the muon from the interaction is negative from neutrinos and positive for antineutrinos. As a result, a detector that is able to distinguish the charge of the muons produced in neutrino interactions is necessary to understand more about neutrino and antineutrino interactions that the T2K beamline generates.

Combining the ability of BabyMIND that it can constrain positively and negatively charged tracks with the fact that the neutrinos reach BabyMIND with an off-axis angle of 1.5° on WAGASCI and BabyMIND, the BabyMIND detector allows the measure of wrong-sign contamination of the neutrino beam observed at an off-axis angle of 1.5°, which can then can be compared to the simulation values. This comparison can increase the understanding of the neutrino beam generated from the beamline to BabyMIND, and also allows possible improvements on the simulation code by identifying the differences between simulations and experimental results.

To distinguish neutrino and antineutrino interactions, the BabyMIND detector is built to allow a strong magnetic field with a strength of 1.5 T to flow inside the iron component of the detector. As a consequence, neutrino interactions, which produce negative muons, have their dominant track bend downwards and antineutrinos produce positive muons, which bend upwards in the center of BabyMIND. To introduce such a magnetic field in the detector, iron plates are used as the interaction target in BabyMIND, with a horizontal induced magnetic field with a strength of 1.5 T, as shown in Fig. 2.12.

As BabyMIND is built as a magnetized detector, iron is the optimal material for the target

plates in BabyMIND, similar to the SMRDs, and is different from the hydrocarbon and water used in the proton module and WAGASCI. Therefore, BabyMIND also provides an opportunity for the T2K experiment to compare neutrino interactions, mainly CCQE interactions and their corresponding cross-sections, as a function of the atomic number and nuclear mass of the three materials.

Another important contribution from BabyMIND is the increase of data yield as a result of the relatively high mass. For the first module of iron plates in BabyMIND, where most of the neutrino interactions entering BabyMIND will appear to start, the dimensions are $350 \times 200 \times 9\,\mathrm{cm}^3 = 6.30 \times 10^5\,\mathrm{cm}^3$. As the density of iron is $7.874\,\mathrm{g/cm}^3$, the total mass of the first iron module is $4.96 \times 10^6\,\mathrm{g} = 4960\,\mathrm{kg}$. Comparing this to the mass of WAGASCI, the dimensions of the two WAGASCI modules combined are $127.6 \times 120.4 \times 51\,\mathrm{cm}^3 \times 2 = 1.57 \times 10^6\,\mathrm{cm}^3$. As the density of the hydrocarbon is $1.032\,\mathrm{g/cm}^3$, and the density of water is $1\,\mathrm{g/cm}^3$, the mass of the WAGASCI modules combined is around 1600 kg, which is less than the mass of the first iron module in BabyMIND. As a result, it is expected that the BabyMIND detector can increase the yield of CCQE neutrino interactions, thus providing more data to be analyzed.

The data recorded from BabyMIND has to be reconstructed by track reconstruction code, using the position of the muons recorded by the scintillators. The track reconstruction can analyze the data, and reconstruct the information of the clusters of hits, the interaction vertices, and the reconstructed tracks based on different algorithms. Different algorithms will affect the final result of the reconstruction, thus choosing and implementing the suitable algorithm is essential for track reconstruction, and is being investigated by different researchers in the T2K project.

The information that is reconstructed from the tracks, mainly the muon momenta, can then be used in equation 1.26 to extract the energy of the neutrino in the CCQE interaction. With the neutrino energy extracted, it is possible to extract the cross-section information of the interaction as a function of neutrino energy. In this chapter, we will not extract the neutrino cross section, but instead we will measure the neutrino yields deduced from muon momenta, using the existing reconstruction, and compare the yields for neutrino interactions and antineutrino interactions.

4.2 Simulation of neutrino interactions in iron

The simulations of neutrino interactions are performed using the NEUT package [59], which is a neutrino-nucleus scattering simulation package written and maintained by the researchers in the Super-Kamiokande, T2K and Hyper-Kamiokande experiments. The NEUT software is capable of simulating neutrino interactions from 100 MeV to a few TeV, and calculate the initial and final state nuclear effects for materials from boron to lead. As NEUT calculates neutrino-nucleus scattering, the re-scattering of hadrons from neutrino interactions can be handled by NEUT, and low energy pion scattering and pion production can be simulated by NEUT. The

Monte-Carlo neutrino interaction simulation code that is used in this thesis is written based on NEUT, and is developed by researchers in T2K.

The Monte-Carlo (MC) simulations can create true information of the neutrino interactions. From simple mono-energetic, narrow (pencil) beams to realistic beam flux distributions, the MC simulation can simulate the interactions and give information on the tracks, such as the positions of all the hits when the tracks pass through the iron and scintillator plates, the directions of motion, and the momenta of the tracks right after the neutrino interactions. The information is considered to be 'true' information since this is a simulation of neutrino interactions in the experiment, where most of the information of these true events is impossible to retrieve, and is only available in simulations. The MC code can receive inputs from the FLUKA flux files that contain neutrino beam flux outputs similar to the T2K beamline in reality, or specify a pencil beam with various settings such as the momentum of the pencil beam and the incident angle of the neutrinos. The simulation code is also capable of selecting the interaction to occur only at a specific detector.

For the interest of this thesis, the neutrino interactions that are investigated are the interactions that happen inside BabyMIND, which represents the interaction between neutrinos and the iron nuclei. In the code, while selecting BabyMIND as the detector of interest, the location in which the neutrinos interact with the iron nucleus is randomly distributed across all iron plates. However, we want to extract as much information about the muon tracks in BabyMIND as possible, so we select a fiducial volume in which neutrino interactions only occur in the first three iron plates (the first iron module) of BabyMIND, and thus in this thesis the MC code is modified to force the neutrino interactions that occur inside BabyMIND to be randomly generated only in the first three iron plates.

Fig. 4.1 shows some of the information extracted from the true muon tracks generated from the MC code. From Fig. 4.1, the simulated true muon momentum peaks at $500\,\mathrm{MeV/c}$ and the true muon-neutrino energy plot has a wide peak at approximately $600-700\,\mathrm{MeV}$. This truth information is able to be extracted due to the fact that the interaction is simulated by code, and is available to the user. For real data, a reconstruction method is necessary to allow the hits generated from the MC to be reconstructed into clusters, then to be reconstructed into interaction vertices, and finally to be reconstructed into tracks that may differ from the true tracks.

4.3 Reconstruction of muons in BabyMIND

The track reconstruction code is written specifically for the T2K experiment by the researchers in the project. The reconstruction process starts from the hits that are generated in the MC code. These hits will be seeded and divided into different clusters using the cellular automaton based (CAT) algorithm [60]. The hits are collected into clusters that are contained by three-dimensional cells in space. Each of the cells contains states of 0 (nothing in the cell) or 1 (track

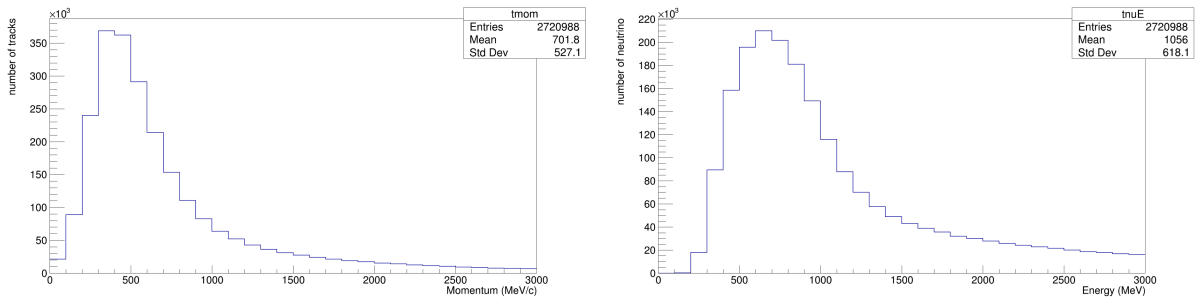

Figure 4.1: The true muon momentum spectrum (left) and the true muon-neutrino energy spectrum (right) from 0 to 3000 MeV/c muon momenta, generated with the JNUBeam neutrino beam simulation and the NEUT neutrino interaction package.

segments in the cell), and track segments are created inside a cell by connecting neighbouring hits that can maximize the smoothness and length of the track segments. After the construction of track segments, the cellular automaton algorithm is performed, where the automaton looks for neighbours of the cells. If a cell has a leftward neighbour that contains the same number of states as the states in the cell, then the number of states in the cell is increased by one. This forward iterative process continues until no more neighbours with the same states can be found. After the forward interative process, it is expected that the cells have higher states towards the right side of the space. The automaton then performs a backward pass that starts from the cell with the highest states, and looks for the leftward neighbours to find the optimized neighbour to form a candidate track, which now should span over cells with an ascending order of states starting from the leftmost of the track [61].

This seeding process gives a direction for the code to know which clusters belong to the same track, and thus is the first step of the reconstruction process. After seeding, the clusters are then reconstructed into interaction vertices, where the positions of the neutrino interactions are reconstructed. With the interaction positions reconstructed, tracks can be reconstructed to obtain the momenta and directions of the reconstructed tracks. As positions of the hits are the only known variables that are known in reconstruction and in the actual experiment, different strategies are proposed on how to reconstruct the momenta and energies of the tracks. Two of the main directions for reconstruction in BabyMIND are reconstruction by range and reconstruction by curvature.

To understand the relationship between momentum and the travel distance of the track, the Bethe-Bloch function is introduced as follows [62, 63],

$$-\frac{dE}{dx} = Kz^2\frac{Z}{A}\frac{1}{\beta^2}\left[\frac{1}{2}ln\frac{2m_ec^2\beta^2\gamma^2T_{max}}{I^2} - \beta^2 - \frac{\delta}{2}\right]. \tag{4.1}$$

The Bethe-Bloch (BB) equation consists of variables that remain constant, such as the mass of the electron m_e and $K = 4\pi N_A r_e^2 m_e c^2$, a variable that depends on Avogadro's constant N_A,

the electron radius r_e and m_e. Some other variables are material-dependent, such as the atomic number, Z, and atomic mass, A of the material. The mean excitation energy, I, is also material-dependent. For the interest of this research, where the BB equation is used on muon tracks, the charge of the incident particle z is also a constant as only charge of muon is considered. As a result, the only independent variables that are not constants are the relativistic terms $\beta\gamma = \frac{v\gamma}{c}$, T_{max}, the maximum possible kinetic energy loss in a single collison, which is a function of $\beta\gamma$ and the mass of muon and electron (constants), and the mean rate of energy loss $-\frac{dE}{dx}$.

The Bethe-Bloch equation describes the relationship between the energy loss of the particle travelling through a material, also known as the stopping power, and the velocity of the particle. Fig. 4.2 shows the relationship between the stopping power and the $\beta\gamma$, which is interchangeable with momentum or kinetic energy, of μ^+ on copper. Although our material of interest for this thesis is iron, equation 4.1 shows that the change of material simply acts as a scaling of the overall trend of the stopping power as a function of $\beta\gamma$. The $\beta\gamma$ range of interest in BabyMIND should be between 0.1 and 100, which corresponds to muon momenta of $10\,\mathrm{MeV/c}$ to $10\,\mathrm{GeV/c}$. For momenta below the minimum ionization value, there is a vast increase in stopping power as the momentum of the muon decreases. Meanwhile, at higher momentum, above the minimum ionization value, the stopping power increases only by a slight number from 0.1 to $10\,\mathrm{GeV/c}$. This suggested that the change of the muon stopping power is more sensitive at low momentum, i.e. when the muon is about to stop.

While reconstructing the tracks by the range travelled is one of the options, the reconstruction can also be done by investigating the curvature of the motion inside the magnetic field. As BabyMIND is a magnetized detector, the muons passing through the magnetized iron will have curvatures based on the momentum of the muons. Investigating the curvatures can then be used to reconstruct the momentum of the muons, and then obtain the neutrino energies. However, the complexity of reconstructing momentum by curvature is high due to the geometry of BabyMIND. Due to the scintillators in between magnetized iron plates, the magnetic field inside BabyMIND is not uniform in z, and thus instead of smooth curves, tracks inside BabyMIND are composed of multiple segments of curves in the iron plates, and multiple segments of straight line in the scintillators. This makes the reconstruction difficult as the curvature is changing. In this thesis, the method that is used to reconstruct tracks is reconstructing momentum by range, using the Bethe-Bloch equation in equation 4.1.

The implementation of the Bethe-Bloch equation into the track reconstruction is not trivial, as the equation has three variables that are not a property of the target material. These are dE, the change of energy we wish to find, dx, the change of position, and $\beta\gamma$, which is a relativistic velocity term that depends on the speed of the track. For reconstruction, dx is the only variable that is known, and thus it is not possible to just apply the BB equation forward, starting from the interaction vertex. However, the value of $\beta\gamma$ can be constrained in one scenario, which is when the track stops. In this case, $\beta\gamma = 0$. The strategy of reconstruction using the BB equation is to

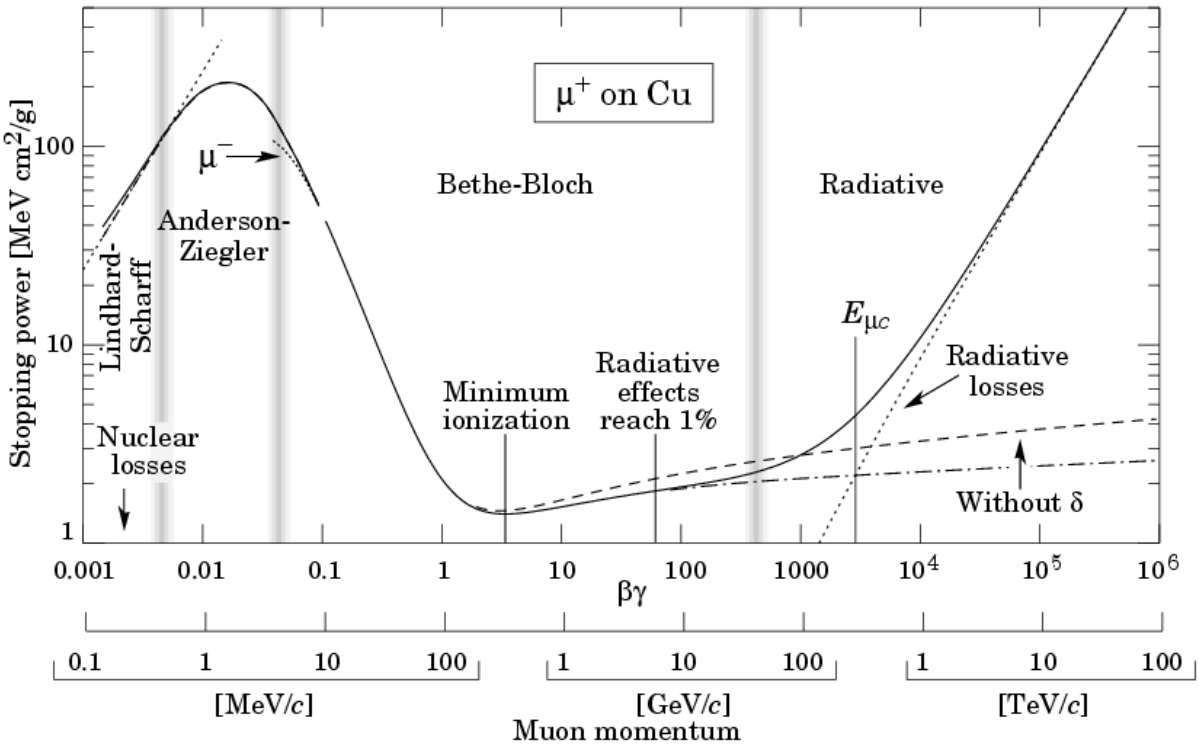

Figure 4.2: A plot of the stopper power over the $\beta\gamma$, or the momentum (interchangeable), for μ^+ on copper [63]

start from the last hit of the track and reconstruct backwards. However, the information of the previous hit is also necessary to start the first step of the BB calculation.

From here onward, assumptions are made to estimate the position of the stopping point for the tracks, and the $\beta\gamma$ value of the track just before it stops. For the position of the stopping point, the assumption is that the particle stops in the middle point in the iron plate between the scintillator of the last hit and the next scintillator, if there are iron plates in between the two scintillators, and stops in the center of the scintillator if there is no iron plates downstream of that scintillator. This method assumes that the position where the track stops inside an iron module is randomly distributed. A BB calculation is then performed backwards starting from the stopping point. As the stopping power is sensitive at low muon momentum, the BB calculation is done recursively every half of the iron plate if the track stops in iron, or 20 times inside the scintillator to ensure that the sensitivity of the stopping power at low momentum has a smaller effect to the reconstruction. The $\beta\gamma$ value of the first step, and the relationship between the stopping power and the kinetic energy for muons in iron and in polystyrene (the material of the scintillators) is retrieved from tables created by Groom, Mokhov and Striganov in 2001 [62].

Since the kinetic energy $KE = \sqrt{m_0^2 + p^2} - m_0$, and the momentum of muons are directly related to $\beta\gamma$, as shown in Fig. 4.2, by using the tables, we can assume the stopping power of lowest available kinetic energy in the table at 10 MeV is the stopping power to use in the first step. The energy loss at any given step is the multiplication of the total energy loss rate,

with units of $\mathrm{MeVcm}^2/\mathrm{g}$, and the density per unit area, $X = \rho dx$ where ρ is the density of the material, in this given step. The sum of all the energy losses from the first step to a given step is then converted into the $\beta\gamma$ value for the next step. This recursive process, once it covers all the hits in the track, extracts the total energy loss of the track, and thus the momentum of the track is obtained.

To test and verify the Bethe-Bloch equation algorithm, simple cases are investigated before reconstructing the MC results that are generated by the T2K beam flux distributions. The reconstructions are done on pencil beams with various muon momenta, from $0\,\mathrm{MeV/c}$ to $2000\,\mathrm{MeV/c}$ for every $100\,\mathrm{MeV/c}$ step. Two types of pencil beams are used in this investigation. Two configurations of the beam are simulated. One of the beams is parallel with the z-axis with a zero off-axis angle, and with the magnetic field in the iron plates turned off. The other beam has an off-axis angle of 30°, and magnetic field turned on to match the MC results using the T2K flux data. Examples of the reconstructed muon momenta of the pencil beams, alongside with the comparison to the true muon momenta with the residual plots (true minus reconstructed) of such beams are shown in Fig. 4.3 and Fig. 4.4, and when all the results from different true momenta are combined together, migration matrices for the two beams are formed in Fig. 4.5 and Fig. 4.6.

The small peaks from the residual plot of Fig. 4.3 is due to the structure of BabyMIND and the location of the scintillator, that caused the reconstruction from hits collected in the scintillator to have discrete characteristics, with a small portion of muons creating hits in the next scintillator plane. This means that the fraction of hits in the next plane increases as the momentum increases, since the fraction of muons that punches through to the next scintillator is larger. Hence, we have double peaks with varying heights in momentum and residual.

The width of the distribution for the 700 MeV/c muons at 30 degrees is broader because of the opening angle, so the amount of iron traversed between scintillator planes is larger. However, when the beam has a true momentum of $1300\,\mathrm{MeV/c}$, it is not a discrete peak anymore due to the fact that the beam is entering BabyMIND with an angle with a high enough energy that the beam reaches that side of the BabyMIND and escapes, causing an underestimation of the true momentum of the beam.

From both of the individual plots and the migration matrix, it is shown that the true muon tracks at low energies are not reconstructed. This is due to the limitation of reconstructing momentum by range and the fact that the low-momentum muons do not make enough scintillator hits to produce a track due to the high density of the iron. For low momentum muons below $300\,\mathrm{MeV/c}$, there is not enough momentum for the muons to travel through enough layers of iron and scintillator to result in a reconstructible track. As a result, the information at low energies is lost. Another limitation from the pencil beam reconstruction is that the reconstructed momentum cannot increase beyond the point where the true momentum increases high enough that the muon crosses the length of BabyMIND and exits the detector.

For the beam without angle, the limit of true momentum before the reconstructed momentum becomes constant is $1600\,\mathrm{MeV/c}$, and for the beam with a 30° angle, the limit is $1200\,\mathrm{MeV/c}$. This is due to the fact that tracks with high energies pass through the whole detector, leaving hits across all the plates, thus all the true tracks with a momentum passing the limit of the detector are all reconstructed with similar momentum values, as the reconstruction code assumes that the muon stops at the last scintillator.

The reason that the limit for the beam at a non-zero angle is lower is because the beam escapes not at the end of BabyMIND, but at the sides, causing the length of tracks inside BabyMIND to be smaller, and the limit for reconstruction lower compared to the beam with zero angle. The efficiency of the reconstruction in both cases, obtained from dividing the number of reconstructed tracks with the number of true tracks (10000 for all pencil beams), for the two configurations are shown in Fig. 4.7. These two plots show the efficiency of the BB reconstruction in BabyMIND, supporting the fact that low energies are not reconstructed.

The mean values of all the reconstructed momentum spectra for the two types of beam configurations are shown in Fig. 4.8, with the standard deviation of each of the reconstructed momentum as the error. The red line across the two plots represent the function $y = x$, which, in the relationship between true and reconstructed momentum, represents the ideal scenario where all the momenta are perfectly reconstructed. As $y = x$ lies in between the error bars between energies around $400\,\mathrm{MeV}$ and the upper limit of the reconstructed momenta, the BB reconstruction is shown to be a suitable reconstruction tool in this region, and can be used to reconstruct tracks from the MC simulation results.

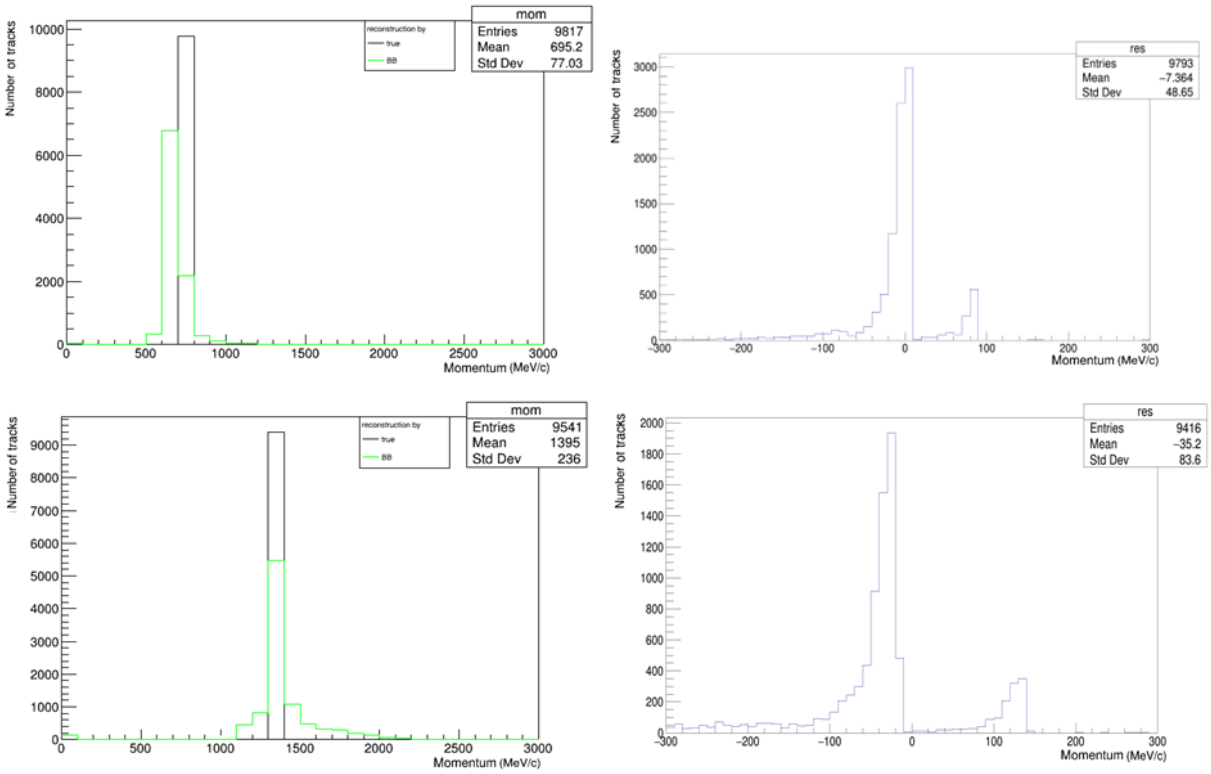

Figure 4.3: Some example plots of the pencil beam with neutrinos travelling parallel to the z-axis into BabyMIND without magnetic field. Plots on the left are a comparison between the true momentum (black) and the reconstructed momentum (green), and on the right are the residual plots, from subtracting the true momentum with the reconstructed momentum for each track. The beam has a momentum of 700 MeV/c on the top and 1300 MeV/c (above the limit where the muon will exit the detector) at the bottom.

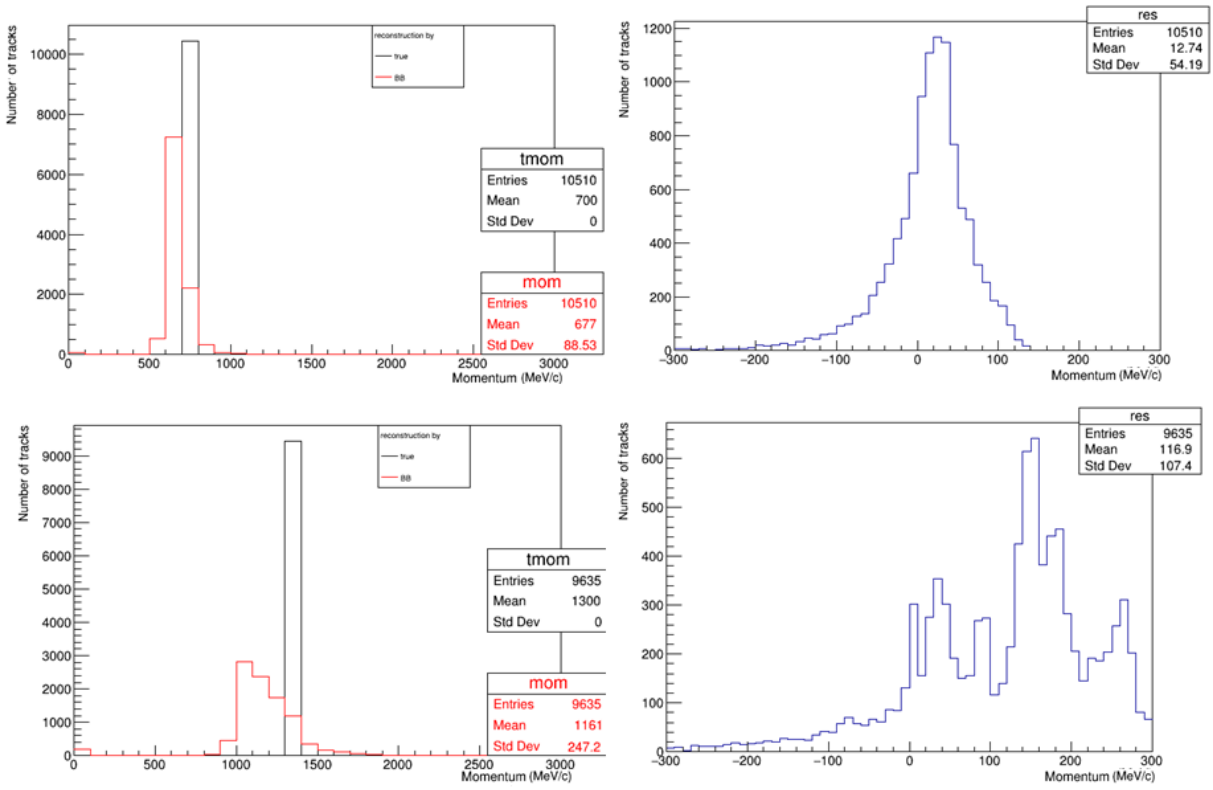

Figure 4.4: Some example plots of the pencil beam with neutrinos travelling with incident angle of 30° into BabyMIND with magnetic field. Plots on the left are a comparison between the true momentum (black) and the reconstructed momentum (red), and on the right are the residual plots, from subtracting the true momentum with the reconstructed momentum for each track. The beam has a momentum of 700 MeV/c on the top and 1300 MeV/c at the bottom (above the limit where the muon will exit the detector).

The reconstruction of the MC results are necessary before reconstructing the experimental data. Simulating the reconstructed tracks from MC results, which aim to provide realistic simulations of the T2K beams passing through BabyMIND, is the foundation for the construction of the migration matrix that represents the correspondence between a true track and its reconstructed counterpart. As a result, multiple constraints are made for the reconstruction of the MC results that mimic the conditions that the experimental data should have. In experiments, many of the neutrinos from the beam have to undergo interactions already with upstream detectors such as the WAGASCI detectors and the proton module. As a result, it is expected that most of the muon tracks detected come from outside of BabyMIND.

A new set of simulations were carried out, using the JNUBeam neutrino flux for BabyMIND and the NEUT neutrino event generator to simulate muon neutrino and antineutrino CCQE interactions in the iron of the first three iron plates of BabyMIND. To focus on the muon tracks that originate inside BabyMIND, all the tracks with a hit at the first scintillator plane (the scintillator without any iron plates in front) are vetoed out.

Another condition that is implemented in the reconstruction is the incident $x-y$ position. As shown in Fig. 2.12, the magnetic field at the left and right sides is not uniform as this part of the iron plate acts as a flux return to bend the magnetic field from the middle section to the top and bottom of the iron plates. The top and bottom magnetic fields also have an opposite direction compared to the center part. As a result, another condition is to veto out every track that starts with an x-position above one meter from the center or with a y-position above half of a meter from the center of the $x-y$ plane of BabyMIND. All selection conditions for reconstructed tracks in this thesis are listed in table 4.1. These two conditions ensure that all the tracks that are reconstructed originate inside the center part of BabyMIND, where the magnetic field has a $-x$ direction.

The comparison of all the true tracks generated in MC simulations and all the reconstructed tracks after applying such conditions and the Bethe-Bloch muon-by-range algorithm is shown in Fig. 4.9, which shows that for the range of momenta between 0 and 2000 MeV/c, only 29.0% of the true tracks are reconstructed after the veto process, with a peak at around 1500 MeV/c. With such results, a migration matrix on muon momentum between all the true tracks that were reconstructed and their corresponding reconstructed tracks is created and shown in Fig. 4.10.

The matrix shows that the reconstructed momenta are proportional to the true momenta. Examples of projections of all the reconstructed momenta within selected true momentum bin is shown in Fig. 4.11. As the projection of the reconstructed momenta, unlike the reconstructed momenta from pencil beams, are biased, a similar plot to Fig. 4.8 is constructed in Fig. 4.12, but with the mode of the projections instead of the mean value to represent the migration matrix better. The error bars used in Fig. 4.12 are asymmetric, with the root-mean-square (R.M.S.) value for the reconstructed momenta in each true momentum bin below and above the peaks as the bottom and top error bars respectively. The red line is the ideal case for reconstruction $y = x$,

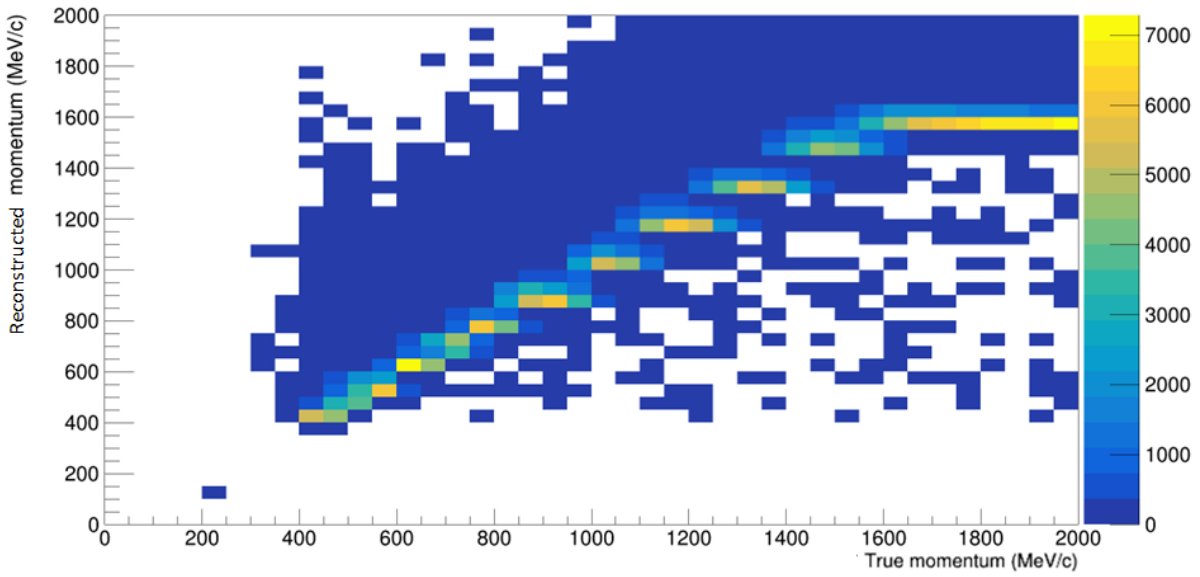

Figure 4.5: The migration matrix of the pencil beam without the incident angle and the magnetic field.

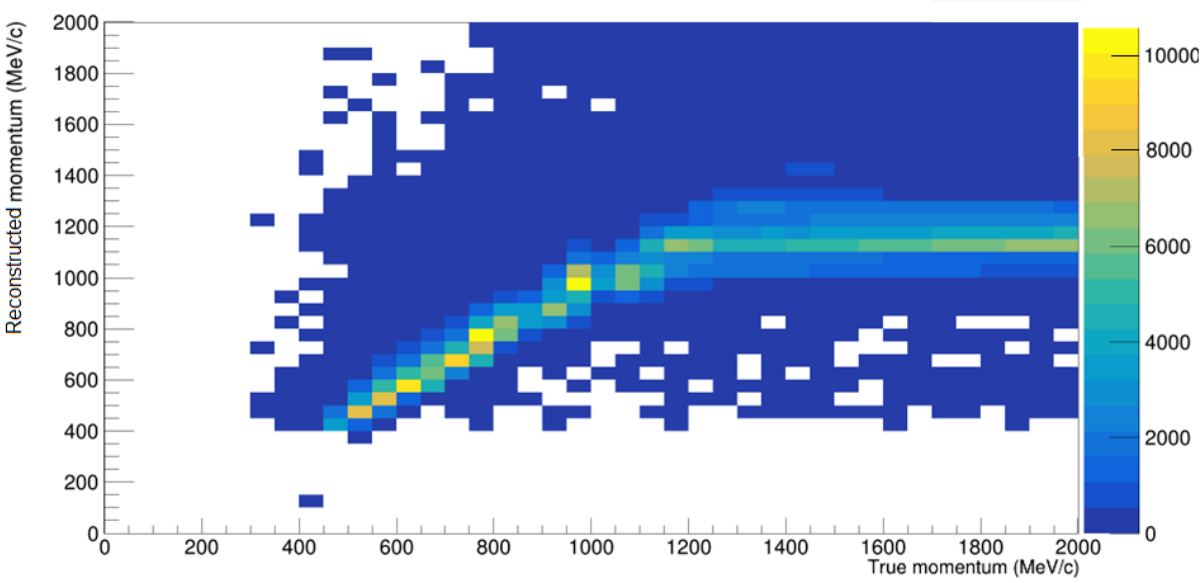

Figure 4.6: The migration matrix of the pencil beam with the incident angle and the magnetic field.

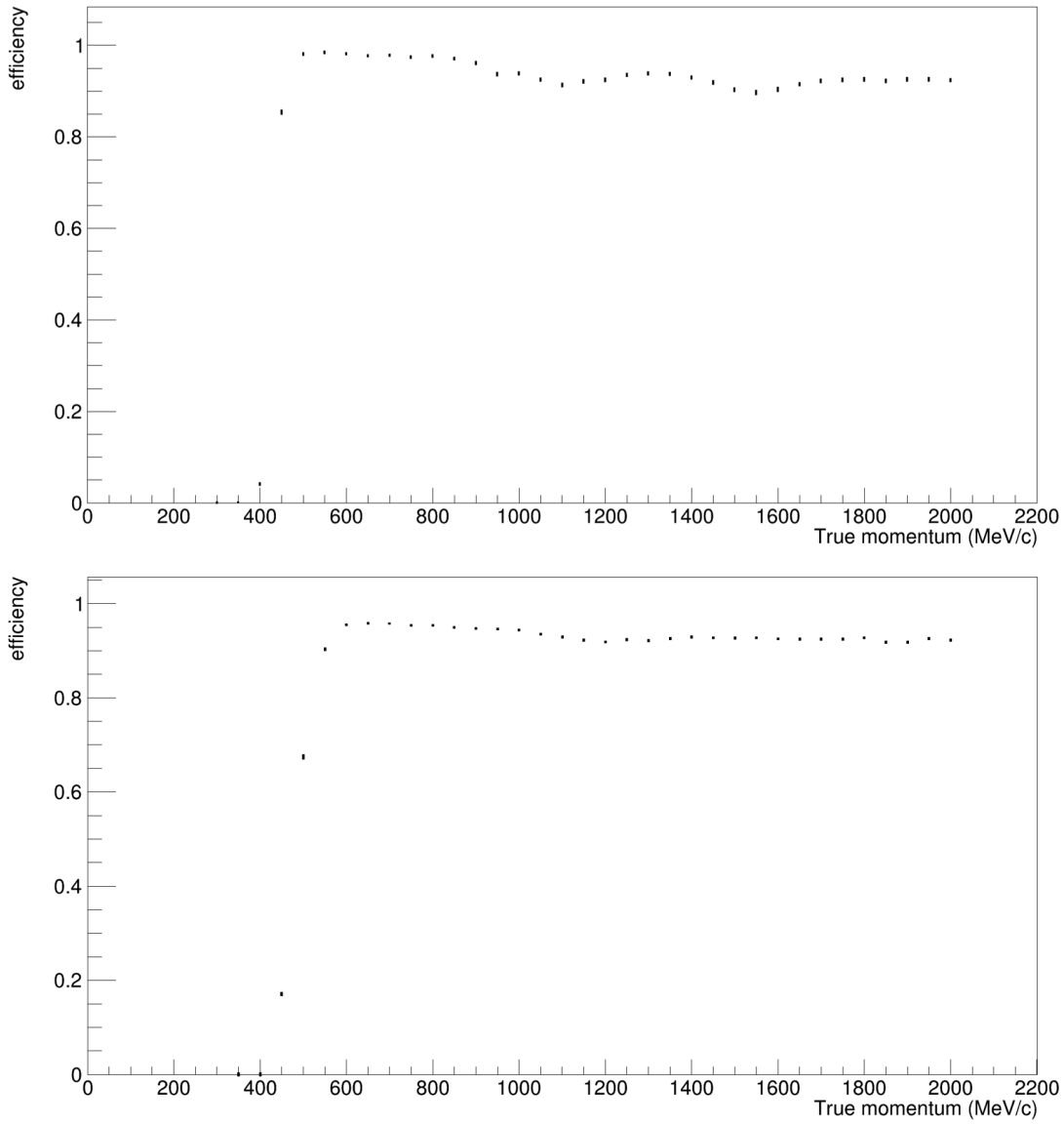

Figure 4.7: The efficiency plot for the pencil beam without the incident angle and the magnetic field (top) and with the incident angle and the magnetic field (bottom). The width of the data dots represent the statistical uncertainties.

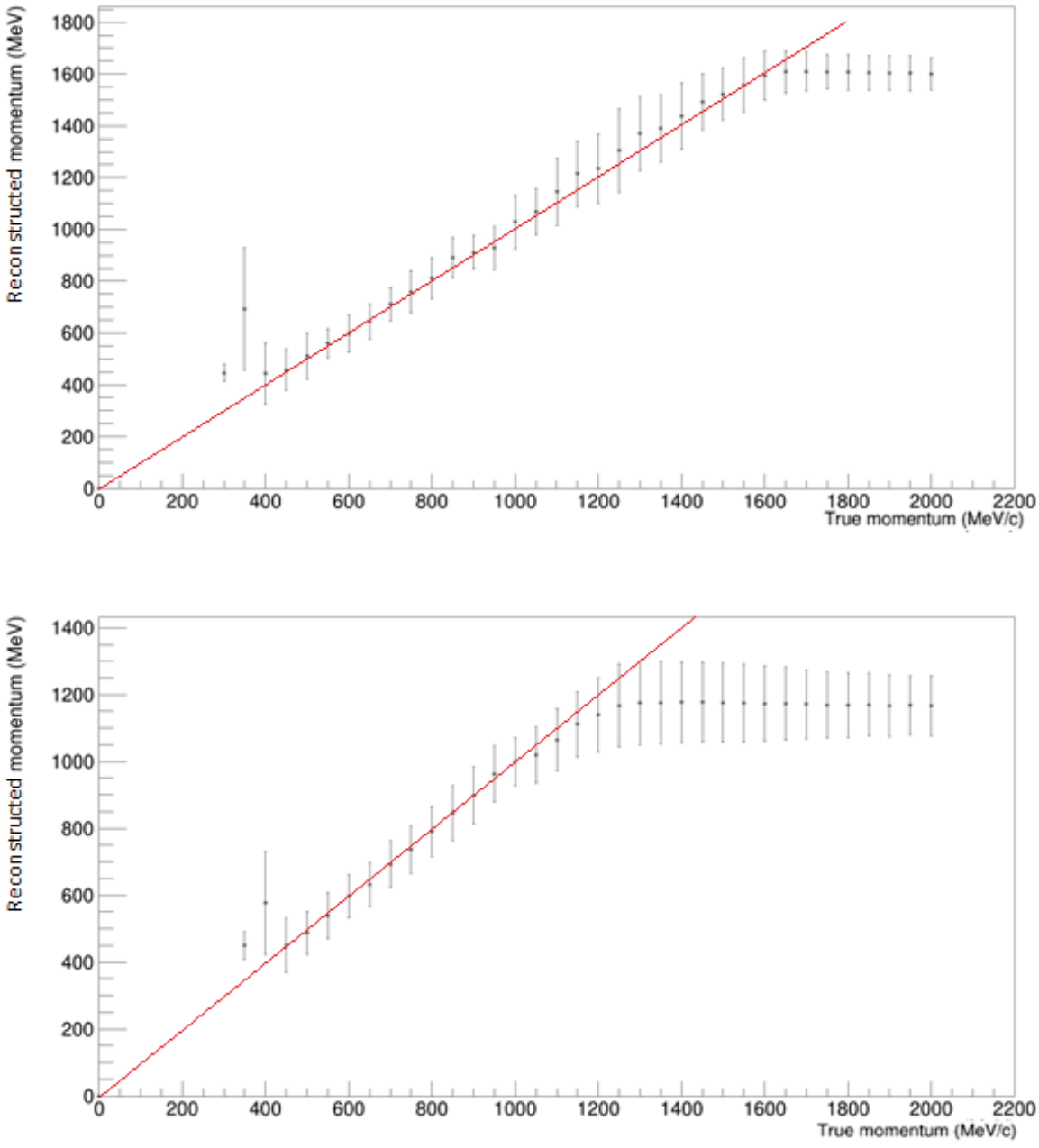

Figure 4.8: The mean values of the reconstructed momentum for each of the true momenta, with the error bars the standard deviations for reconstructed momentum from each of the true momenta. The pencil beams without the incident angle and the magnetic field are at the top and the beams with the 30° incident angle and the magnetic field are at the bottom.

Selection conditions for reconstructed tracks		remaining tracks
Relative x-position (mm)	$-1000 < x < 1000$	76.8%
Relative y-position (mm)	$-500 < y < 500$	42.6%
Scintillator plate indices for the first hit	≥ 2	33.4%
Number of tracks in an event	1 (the longest track)	29.0%

Table 4.1: Table of the selection conditions for reconstructed tracks. The scintillator plate indices start at 1 (the first scintillator plate) and end at 18 (the last scintillator plate). The relative positions are relative to the center of the $x-y$ plane in BabyMIND. The percentage of remaining tracks are cumulative when conditions are applied from the top to bottom in the table.

and it shows that the migration matrix is reasonable for true momentum between 400 MeV/c and 1700 MeV/c, which agrees with the analysis on the pencil beam simulations, but has much larger uncertainties than for the pencil beam simulations.

The migration matrix is a representation of the correlation of the momenta between the true muon tracks and their corresponding reconstructions. After renormalizing the 40×40 matrix in Fig. 4.10, each true momentum bin between 0 and 2000 MeV/c can be written as a vector with a dimension of 40. A matrix multiplication of the true momentum vector on the matrix results in a reconstructed momentum vector with the same dimensions. As a result, to convert reconstruction momentum vector back to true momentum vector, which is the goal of reconstructing experimental data, the inverse of the migration matrix is necessary. However, the inverse of such a complex, large matrix is not a trivial problem.

Although the ROOT package provides the Invert() function for matrix inversion, the zeros at low reconstructed momentum in the matrix causes the matrix to be singular. Even if constraints were applied and the zero values are vetoed out, the Invert() algorithm results in physically impossible negative values in the matrix elements that causes negative values in the product vector. As a result, a more sophisticated matrix inversion algorithm is necessary to be able to unfold the true momenta from the reconstructed momenta. The package used to do the matrix calculations is the RooUnfold package, a package designed for different unfolding algorithms [64]. The unfolding process is the reverse process from the reconstructed information back to the true information, given a trained example of the forward process.

The algorithm used in the thesis makes use of the iterative Bayes' theorem by d'Agostini [65]. The algorithm uses Bayes' theorem, where,

$$P(C_i|E) = \frac{P(E|C_i) \cdot P(C_i)}{\sum_{l=1}^{n_C} P(E|C_l) \cdot P(C_l)}. \tag{4.2}$$

For the interest of this thesis, E is the reconstructed information or the observed information in the experiment, and C_i is the true information. The Bayes' algorithm utilizes equation 4.2 by first making an initial estimation on the expected number of events and the distribution for the true information. While the true muon momenta and number of true tracks are known from

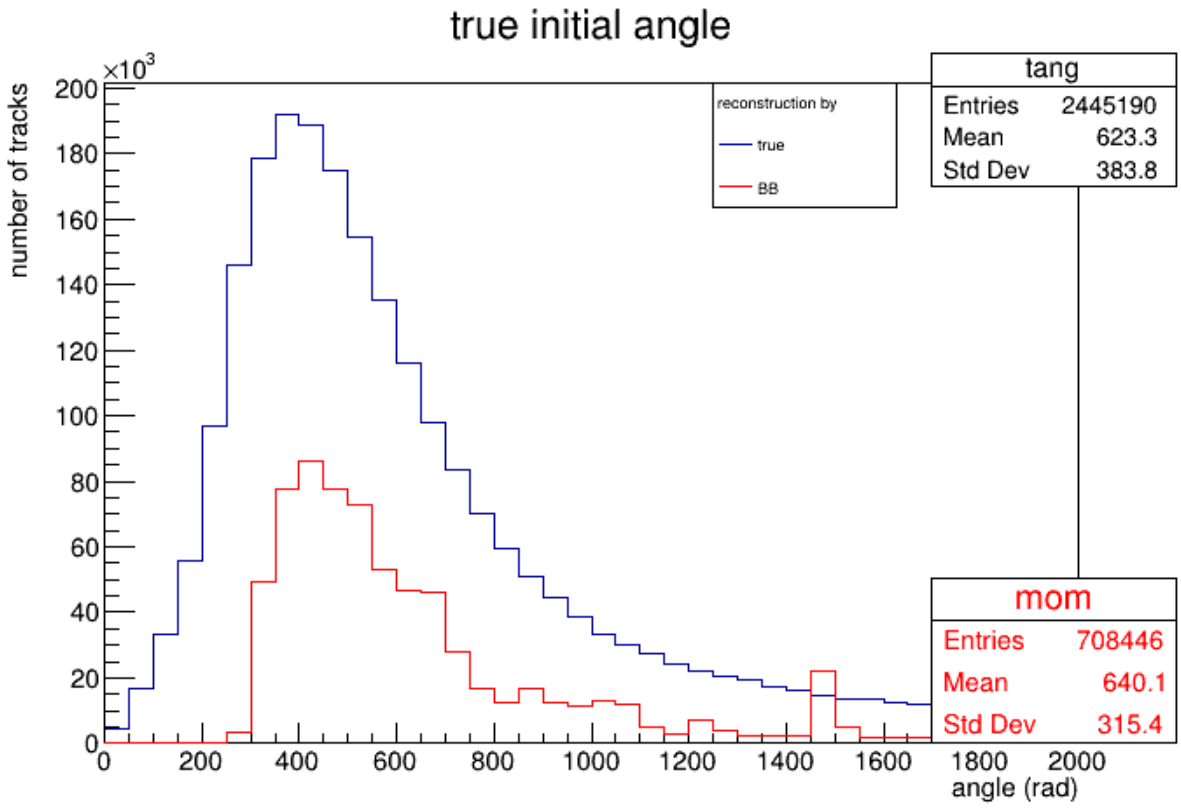

Figure 4.9: A comparison of momenta with a range of $0-2000\,\mathrm{MeV/c}$ between all the true tracks (blue) and their corresponding reconstructions using the Bethe-Bloch (BB) muon-by-range algorithm (red) discussed in the text.

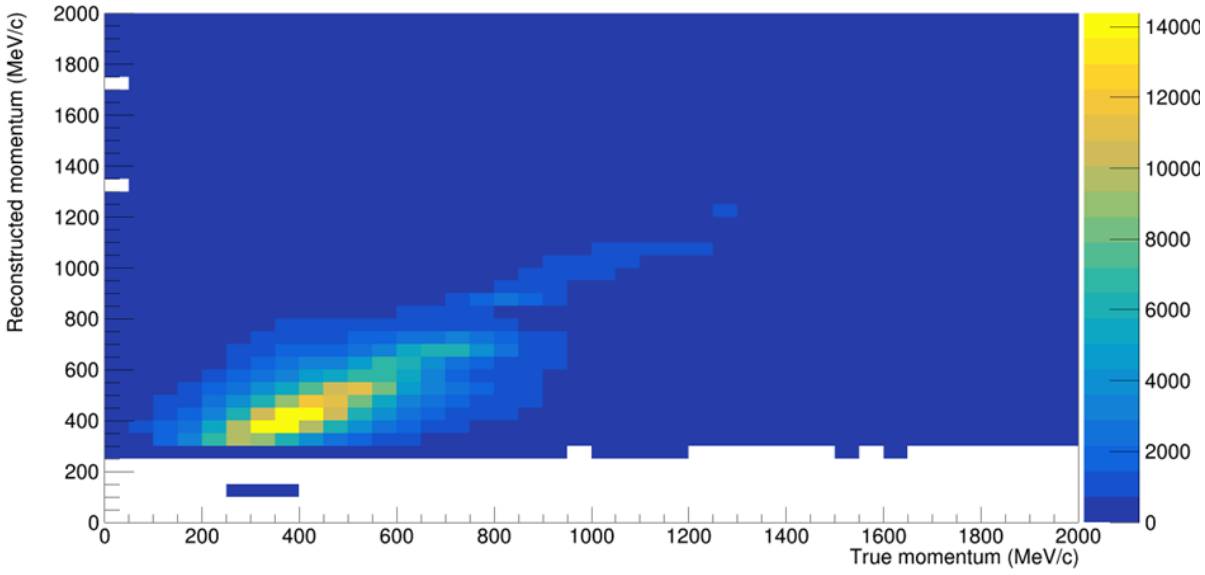

Figure 4.10: The migration matrix between true momenta from the muon tracks generated from the CCQE neutrino interaction simulations that were reconstructed and the reconstructed momenta from the reconstruction of these true tracks, with a bin size of $50\,\mathrm{MeV/c}$.

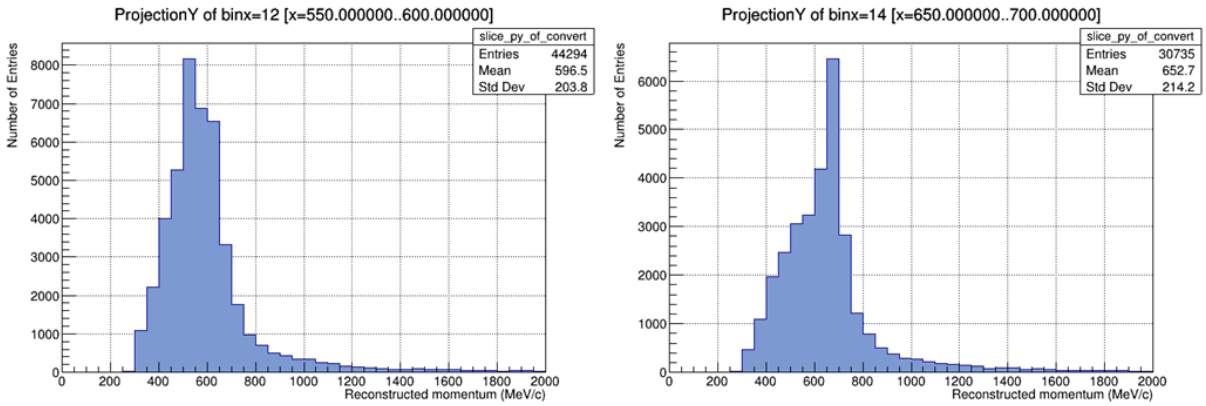

Figure 4.11: Examples of the projections of the reconstructed momenta with a true momentum range of $550-600\,\mathrm{MeV/c}$ (left) and $650-700\,\mathrm{MeV/c}$ (right).

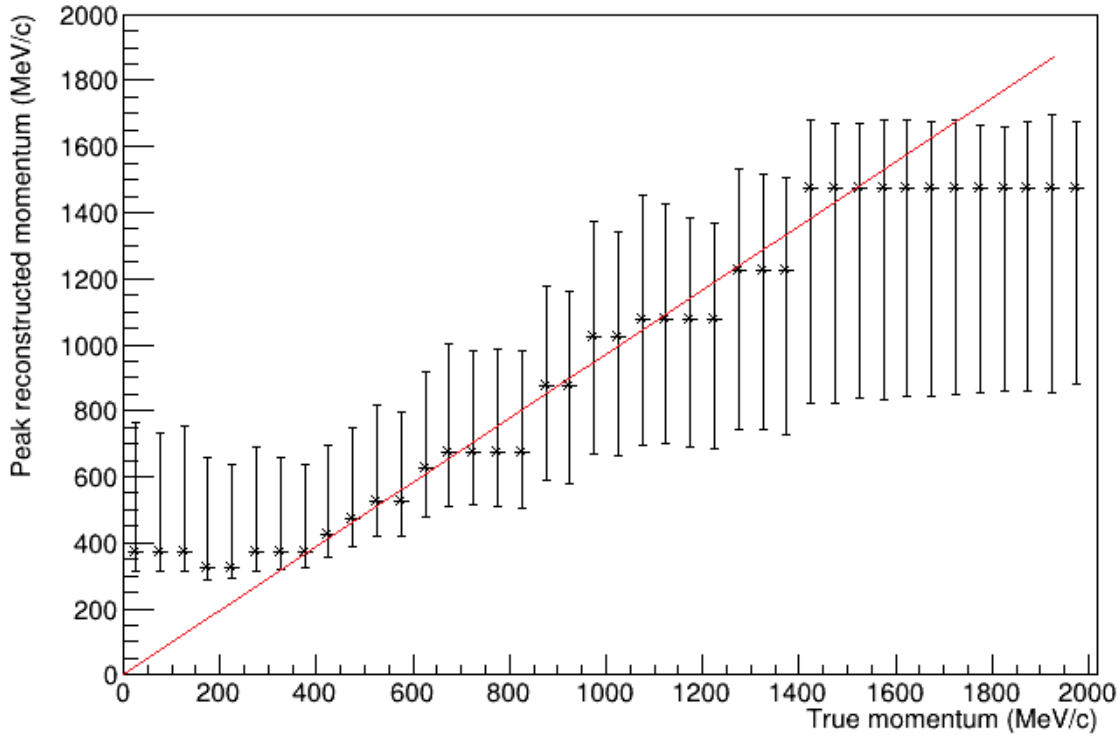

Figure 4.12: The peak value of the reconstructed momentum for CCQE neutrino interactions in the first three iron plates of BabyMIND, for each of the true muon momenta, with the error bars below and above the data point being the root-mean-square (R.M.S.) below and above the peak respectively.

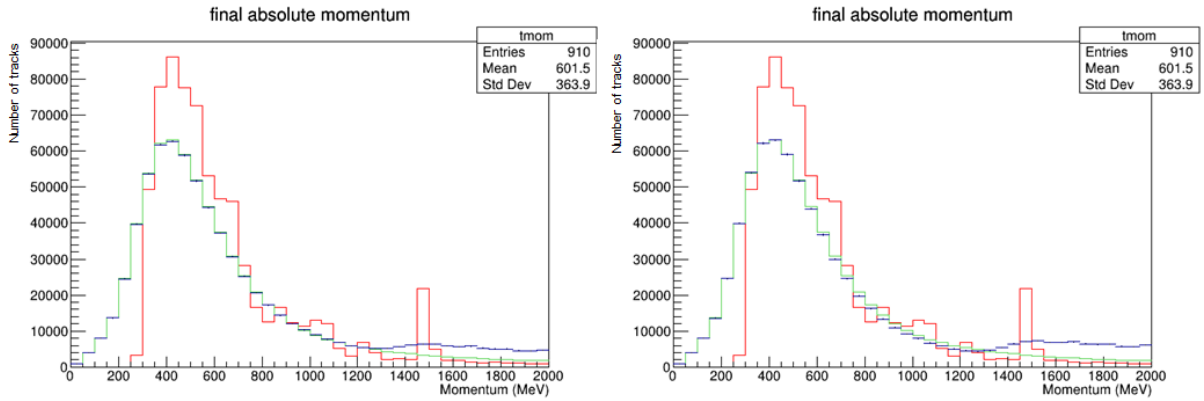

Figure 4.13: The unfolded momentum (blue) with the true momentum from MC simulations (green) and the reconstructed momentum from BB calculations (red) for four (left) and ten (right) iterations.

the MC simulations, the true momenta and number for tracks in experiment is unknown. As a result, the initial estimations of the true momenta and number of tracks in the experiment are the corresponding ones generated with the MC simulations, while the migration matrix acts as the correlation factor between true and reconstructed tracks.

With the matrix, estimations can be made according to the correlations given by the matrix. The result of the initial estimations will be the input to the next iteration, and a χ^2 value between the estimations and the actual data is calculated. The χ^2 value decreases as the number of iterations increases. As a result, the unfolding process on the MC reconstructed momentum is performed to test the performance for different number of iterations. The comparison on results between four and ten iterations is shown in Fig. 4.13. The number of true tracks is 708,446, and the number of unfolded tracks is 708,486, a minor difference due to Bayes' theorem being a iterative process. However, for the momentum range of 0 to 2000 MeV/c, the number of true tracks and unfolded tracks are 672,959 and 708,244 respectively. As a result, while the total number of the tracks are close when considering all the tracks, more tracks are unfolded towards the $1200-2000\,\mathrm{MeV/c}$ range compared with the true track momentum distribution. This is possibly caused by the reconstructed peak at 1500 MeV/c, where the unfolding algorithm wants to accommodate the peak caused by the tracks escaping BabyMIND.

Although the χ^2 value for four iterations ($\chi^2 = 2828$) is larger than that for ten iterations ($\chi^2 = 2556$), Fig. 4.13 shows that the unfolded momentum (blue) is further away from the true momentum (green) at both the low and high energies. As the χ^2 value is calculated bin-by-bin, ignoring the correlations between the true and reconstructed momenta (the migration matrix), the χ^2 calculated by RooUnfold is not an accurate representation of the real χ^2. For this reason, in the following process of data analysis, only four iterations of the Bayes' algorithm is used.

4.4 Neutrino interactions in BabyMIND

The T2K experiment has a total of 11 runs of data to date, and the most recent long run is run 10, in which the data was collected between November 2019 and February 2020. Since the Covid pandemic, a short run was held during March and April of 2021 as run 11. The number of protons-on-target (POTs) for run 10 is 2.35×10^{20}, and the number of POTs for run 11 is 1.00×10^{20}. This thesis uses both the data collected in BabyMIND from run 10 and run 11 to apply the BB reconstruction code, and the Bayes' unfolding algorithm to obtain the estimated true muon momenta for the right-sign and wrong sign muons from neutrino and antineutrino CCQE interactions respectively.

The selection process of reconstructed tracks is the same as what is described in table 4.1, where all the reconstructed tracks with hits in the first scintillator planes, and tracks that originate at the outer ring of BabyMIND are vetoed out, and the fiducial volume selection of neutrino interactions in the first three iron plates of BabyMIND is carried out, as shown in table 4.1.

After the veto and selection process, the muon tracks are separated into right-sign (μ^-) and wrong-sign (μ^+) tracks, as the data collected in run 10 and 11 are under the forward-horn-current (FHC) beam configuration. The separation can be carried out by the direction of motion for the reconstructed tracks, with the right-sign tracks travelling downwards and the wrong-sign travelling upwards due to the existence of the magnetic field in the iron plates. This is done by looking at the position of the muons at the start and the end of the tracks. If the tracks have a higher y-position when they stop compared to when they are generated, the tracks are determined to be bending upward, and the opposite applies for the tracks bending downward.

The reconstructed momentum distribution for the right-sign and wrong-sign tracks are shown in Fig. 4.14. The peak at $1400\,\mathrm{MeV/c}$ is due to the limitation of the BB algorithm that all the tracks that escapes from the back of BabyMIND are treated as stopping at the last scintillator plate. Based on the reconstruction, the wrong-sign ratio (WSR) plot for the muon tracks generated in BabyMIND is generated in Fig. 4.15. The total WSR for a momentum range of 0 to $2000\,\mathrm{MeV/c}$ is 3.73%, and the wrong-sign contamination is higher for higher energies (up to 18%).

With the right-sign and wrong-sign reconstructed momenta obtained, the estimated true momenta for both of the samples can be unfolded. The reconstructed momenta in Fig. 4.14 has been fed into the Bayes' unfolding algorithm, and the estimated true muon momenta for right-sign and wrong-sign are shown in Fig. 4.16, with the WSR plot from the unfolded momentum shown in Fig. 4.17. The unfolded number of μ^- tracks (right-sign) in $0-2000\,\mathrm{MeV/c}$ is 31,789, and the number of μ^+ tracks (wrong-sign) is 1,227, giving the total WSR of 3.86% in this momentum range, with a higher WSR at high momentum of about 12%. The unfolded right-sign momentum has a peak at $300\,\mathrm{MeV/c}$ and the unfolded wrong-sign momentum has a peak at $400\,\mathrm{MeV/c}$.

Comparing the unfolded momentum with the true momentum generated by MC simulations,

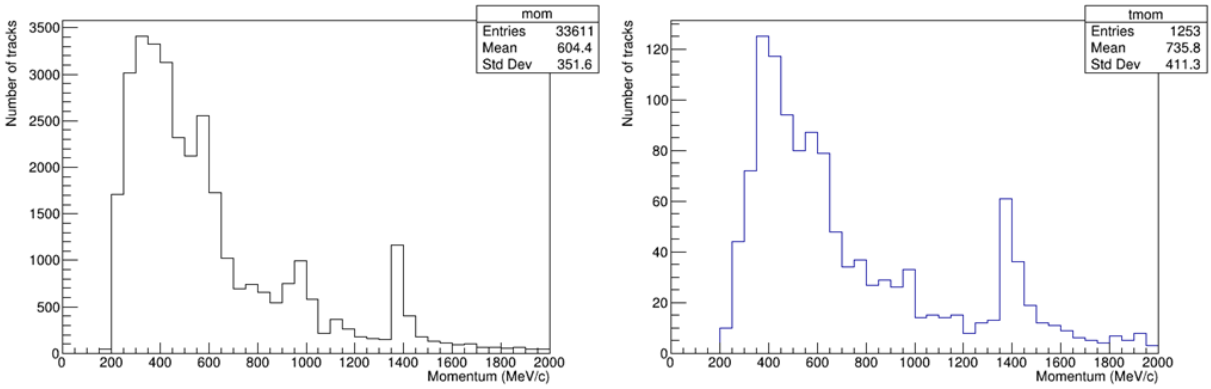

Figure 4.14: The reconstructed momenta for right-sign tracks (left) and wrong-sign tracks (right).

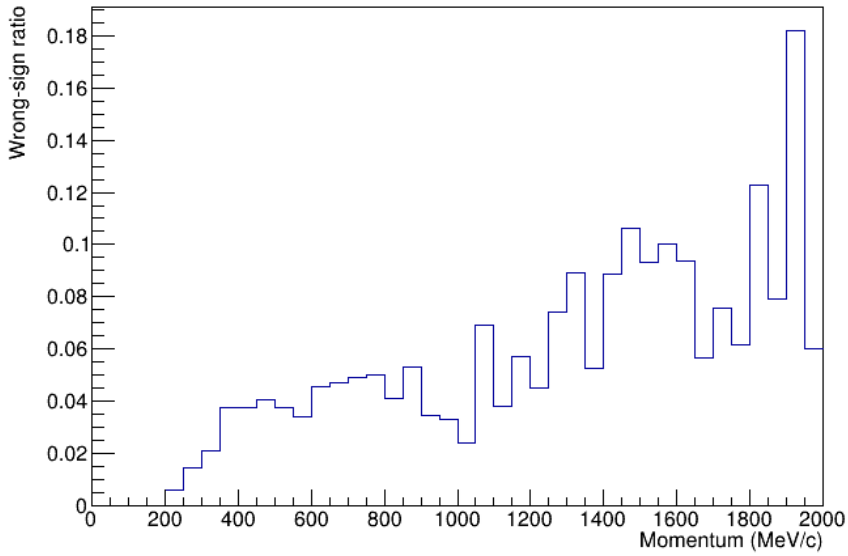

Figure 4.15: The wrong-sign to right-sign ratio (WSR) plot for reconstructed momenta from BabyMIND run 10 and run 11 data.

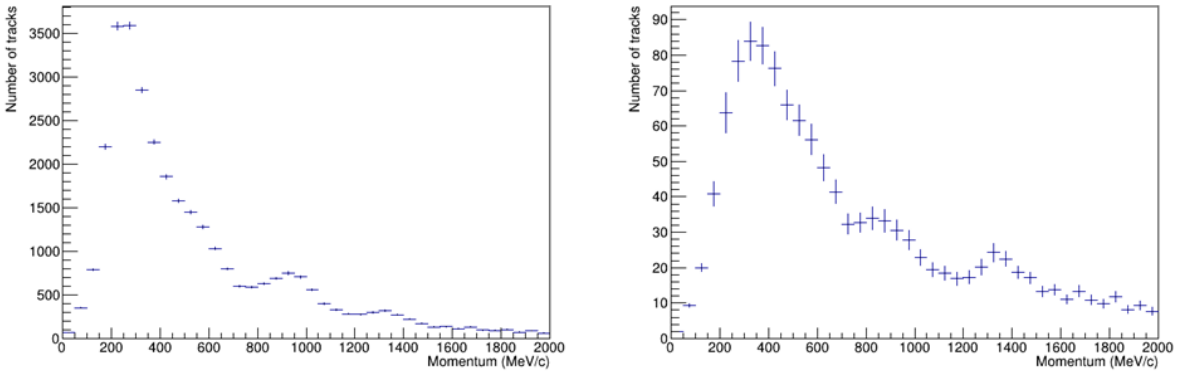

Figure 4.16: The unfolded momenta for right-sign tracks (left) and wrong-sign tracks (right). The error bars are generated by the unfolding algorithm and are statistical.

the position of the peak and the mean are both lower for the unfolded right-sign momentum, suggesting that the unfolding process could still be improved. There are also some bumpy features in the spectrum that could be the result of the neutrinos reconstructed around 1400 MeV/c, since these neutrinos escape the detector and are not well reconstructed. A truncation below 1400 MeV/c would need to be carried out to remove neutrinos with a momentum that cannot be reconstructed.

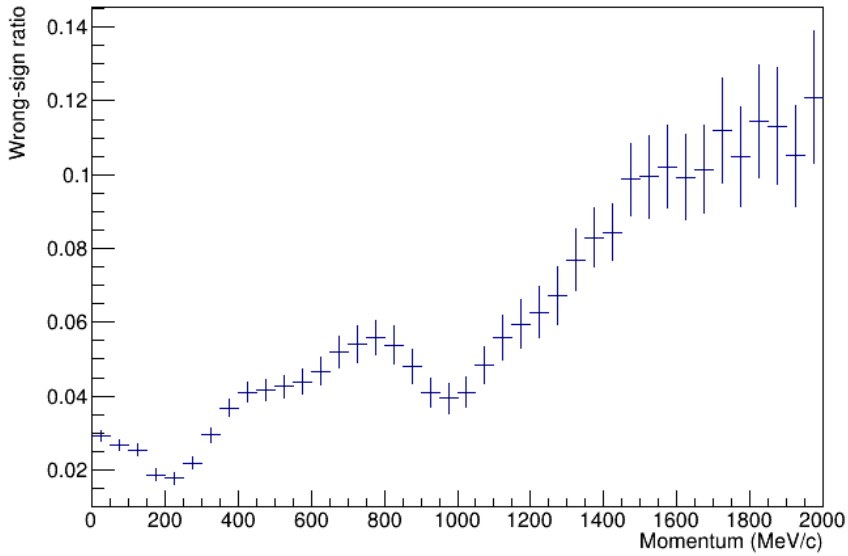

Figure 4.17: The wrong-sign to right-sign ratio (WSR) plot for unfolded momenta from run 10 and run 11 data.

Chapter 5

Conclusions

This thesis summarises two studies that have been performed in the context of the T2K neutrino oscillation experiment. While T2K has already been very successful, and discovered the appearance of electron neutrinos from a muon-neutrino beam over a long baseline, to measure θ_{13} in a long baseline experiment for the first time, and has been successful in showing hints of CP violations from the comparison of neutrino and antineutrino oscillations, more data is required to perform more significant measurements. An upgrade of the T2K detector and the beamline is underway to improve such results.

One possibility as part of the upgrade of T2K, which could be useful for the Hyper-K experiment as well, is to improve the neutrino target in the first horn, by adding a secondary target to the end of the horn, in order to increase the right-sign neutrino flux and decrease the wrong-sign flux. The first study of this thesis included simulations of the neutrino beam in T2K using JNUBeam, with a modified geometry of the first magnetic horn in the secondary beamline of T2K in the simulation. An extra target is inserted at the downstream end of the first magnetic horn as a simulation for a potential future beamline upgrade in T2K. Extra targets of different materials such as graphite, silicon carbide, boron carbide and titanium were tested for their effect on increasing the right-sign neutrino flux yield and decreasing the wrong-sign contamination. The suggestion from the simulation is that while titanium is the best performing material for the extra target at the downstream end, other physical properties, such as its thermal performance and radiation hardness, may prevent the use of titanium as an optimal material for the target.

Meanwhile, silicon carbide performs better than all other materials considered, excluding titanium. Combining with the fact that silicon carbide is a well-understood target material with great resistance to heat, it is the optimal material to use as the new target for the upgrade. This thesis also investigated the effect of materials with similar atomic mass but with varying density, and materials with similar densities with different atomic mass. Results show that decreasing the density of a material normally results in worse performances than the unmodified material. Simulations with a simple support structure for the target were also performed, and shows that the materials used to build the support structure should be as light and unobstrusive as possible,

as the existence of the extra support decreases the performance of the neutrino beam.

This thesis also reports on the Monte-Carlo simulations, the reconstruction algorithms and the unfolding algorithms of neutrino events in the BabyMIND detector. Monte-Carlo simulations were carried out with various pencil beam configurations and with the official T2K neutrino beam flux generated using the JNUBeam neutrino beam simulation package and the interactions simulated in BabyMIND using the NEUT neutrino event generator. The true momenta of the muon tracks from the neutrino interactions with the iron nuclei in the BabyMIND iron plates are extracted and muon momentum reconstruction by range is performed on the true tracks for both pencil beams and T2K flux data using the Bethe-Bloch equation and knowledge of the material inside BabyMIND. The reconstructed results from pencil beams validate the effectiveness of the Bethe-Bloch reconstruction algorithm, and the reconstructed results from the Monte-Carlo simulation of the T2K flux provide a basis for the unfolding of the run 10 and run 11 data recorded from BabyMIND between 2019 and 2021.

The migration matrix from the reconstructed momenta from the simulation acts as the correlation factor for the algorithm, as the basis for an iterative algorithm that utilises Bayes' theorem to initially guess and improve agreement between the reconstructed and the true unfolded muon momenta. Only four iterations are required in the unfolding process to achieve good agreement, and the wrong-sign ratio (the ratio of muon antineutrino to muon neutrino events) for both the reconstructed momentum and the unfolded momentum for experimental data is retrieved, with ratios of 3.73% and 3.86% respectively, between the range of 0 and 2000 $\mathrm{MeV/c}$.

These algorithms, and further developments, can be carried out in the future to extract neutrino and antineutrino cross-sections in BabyMIND, by carrying out the reconstruction and unfolding of muon tracks. The method of unfolding may also be optimized with a more sophisticated treatment of the singular regions below 300 $\mathrm{MeV/c}$ and above 1400 $\mathrm{MeV/c}$. Furthermore, another future development could include developing an algorithm to reconstruct charged tracks in BabyMIND by using the curvature of the tracks in the magnetic fields in the iron plates of BabyMIND. This could be used to perform a comparison between the two track momentum reconstruction methods, by range and by curvature, and to extend the range of momenta that can be measured at high momenta, beyond the capabilities of the muon reconstruction by range in BabyMIND.

Appendix A

Derivation of the CCQE muon neutrino energy formalism

To derive the formalism displayed in equation 1.25, a simple two-body interaction is considered between ν_μ and neutron, denoted N in this case. A Feynman diagram of the interaction, and the interaction in general for a two-body system involving a lepton and a neutron is demonstrated in Fig. 1.2. The product of such interaction is a muon, μ, and a proton, p. As the momentum and energy is conserved before and after the interaction, a set of two equations can be constructed:

$$E_\nu + E_N = E_\mu + E_p, \tag{A.1}$$

$$\mathbf{p}_\nu + \mathbf{p}_N = \mathbf{p}_\mu + \mathbf{p}_p. \tag{A.2}$$

Since $E^2 = |\mathbf{p}|^2 + m^2$ with relativistic units, it is possible to express $\mathbf{p}_p$ as follows:

$$\begin{aligned} |\mathbf{p}_p|^2 &= (\mathbf{p}_\nu + \mathbf{p}_N - \mathbf{p}_\mu)^2 \\ &= |\mathbf{p}_\nu|^2 + |\mathbf{p}_N|^2 + |\mathbf{p}_\mu|^2 - 2\mathbf{p}_\nu \cdot \mathbf{p}_\mu + 2\mathbf{p}_\nu \cdot \mathbf{p}_N - 2\mathbf{p}_N \cdot \mathbf{p}_\mu. \end{aligned} \tag{A.3}$$

Assuming that the neutrino mass can be neglected, $|\mathbf{p}_\nu| = E_\nu$, and thus with the fact that $\mathbf{a} \cdot \mathbf{b} = |\mathbf{a}||\mathbf{b}| cos\theta$, where θ is the angle between the vector $\mathbf{a}$ and $\mathbf{b}$, equation A.3 becomes:

$$|\mathbf{p}_p|^2 = E_\nu^2 + |\mathbf{p}_N|^2 + |\mathbf{p}_\mu|^2 - 2E_\nu|\mathbf{p}_\mu|\cos\theta_\mu + 2E_\nu|\mathbf{p}_N|\cos\theta_N - 2\mathbf{p}_N \cdot \mathbf{p}_\mu. \tag{A.4}$$

The angle θ_μ is the angle between the direction of motion of ν_μ and the direction of motion of the muon, and the same applies to the angle θ_N with ν_μ and the neutron. By rearranging and squaring equation A.1, the equation becomes:

$$\begin{aligned} |\mathbf{p}_p|^2 &= (E_\nu + E_N - E_\mu) - m_p^2 \\ &= E_\nu^2 + E_N^2 + E_\mu^2 - 2E_\nu E_\mu + 2E_\nu E_N - 2E_N E_\mu - m_p^2. \end{aligned} \tag{A.5}$$

E_ν can now be solved by substituting equation A.5 into equation A.4 and rearranging:

$$\begin{aligned} 2E_\nu(E_N - E_\mu + |\mathbf{p}_\mu|\cos\theta_\mu - |\mathbf{p}_N|\cos\theta_N) &= m_P^2 - m_\mu^2 - E_N^2 + 2E_\mu E_N - 2\mathbf{p}_\mu \cdot \mathbf{p}_N + |\mathbf{p}_N|^2, \\ E_\nu &= \frac{m_P^2 - m_\mu^2 - E_N^2 + 2E_\mu E_N - 2\mathbf{p}_\mu \cdot \mathbf{p}_N + |\mathbf{p}_N|^2}{2(E_N - E_\mu + |\mathbf{p}_\mu|\cos\theta_\mu - |\mathbf{p}_N|\cos\theta_N)}. \end{aligned} \tag{A.6}$$

Thus the equation 1.25 is obtained.

Bibliography

[1] E. Noether. Invariante variationsprobleme. *Nachrichten von der Gesellschaft der Wissenschaften zu Göttingen, Mathematisch-Physikalische Klasse*, 1918:235–257, 1918. URL http://eudml.org/doc/59024.

[2] S. Mukhi and P. Roy. Developments in high energy theory. *Pramana - Journal of Physics*, 73, 05 2009. doi: 10.1007/s12043-009-0093-9.

[3] A. D. Sakharov. Violation of CP Invariance, C asymmetry, and baryon asymmetry of the universe. *Pisma Zh. Eksp. Teor. Fiz.*, 5:32–35, 1967. doi: 10.1070/PU1991v034n05ABEH002497.

[4] T. D. Lee and Chen-Ning Yang. Question of Parity Conservation in Weak Interactions. *Phys. Rev.*, 104:254–258, 1956. doi: 10.1103/PhysRev.104.254.

[5] C. S. Wu, E. Ambler, R. W. Hayward, D. D. Hoppes, and R. P. Hudson. Experimental test of parity conservation in beta decay. *Phys. Rev.*, 105:1413–1415, Feb 1957. doi: 10.1103/PhysRev.105.1413. URL https://link.aps.org/doi/10.1103/PhysRev.105.1413.

[6] J. H. Christenson, J. W. Cronin, V. L. Fitch, and R. Turlay. Evidence for the 2π Decay of the K_2^0 Meson. *Phys. Rev. Lett.*, 13:138–140, Jul 1964. doi: 10.1103/PhysRevLett.13.138. URL https://link.aps.org/doi/10.1103/PhysRevLett.13.138.

[7] L. M. Brown. The idea of the neutrino. *Phys. Today*, 31N9:23–28, 1978. doi: 10.1063/1.2995181.

[8] C. L. Cowan, F. Reines, F. B. Harrison, H. W. Kruse, and A. D. McGuire. Detection of the free neutrino: A Confirmation. *Science*, 124:103–104, 1956. doi: 10.1126/science.124.3212.103.

[9] G. Danby, J-M. Gaillard, K. Goulianos, L. M. Lederman, N. Mistry, M. Schwartz, and J. Steinberger. Observation of high-energy neutrino reactions and the existence of two kinds of neutrinos. *Phys. Rev. Lett.*, 9:36–44, Jul 1962. doi: 10.1103/PhysRevLett.9.36. URL https://link.aps.org/doi/10.1103/PhysRevLett.9.36.

[10] K. Kodama et al. Observation of tau neutrino interactions. *Physics Letters B*, 504(3):218–224, apr 2001. doi: 10.1016/s0370-2693(01)00307-0. URL https://doi.org/10.1016%2Fs0370-2693%2801%2900307-0.

[11] S. Dell'Oro, S. Marcocci, M. Viel, and F. Vissani. Neutrinoless double beta decay: 2015 review. *Adv. High Energy Phys.*, 2016:2162659, 2016. doi: 10.1155/2016/2162659.

[12] M. Aker et al. Direct neutrino-mass measurement with sub-electronvolt sensitivity. *Nature Phys.*, 18(2):160–166, 2022. doi: 10.1038/s41567-021-01463-1.

[13] B. Pontecorvo. Inverse beta processes and nonconservation of lepton charge. *Zh. Eksp. Teor. Fiz.*, 34:247, 1957.

[14] Z. Maki, M. Nakagawa, and S. Sakata. Remarks on the unified model of elementary particles. *Prog. Theor. Phys.*, 28:870–880, 1962. doi: 10.1143/PTP.28.870.

[15] S. M. Bilenky. Bruno Pontecorvo and the neutrino. *Usp. Fiz. Nauk*, 184(5):531–538, 2014. doi: 10.3367/UFNe.0184.201405g.0531.

[16] R. L. Workman et al. Review of Particle Physics. *PTEP*, 2022:083C01, 2022. doi: 10.1093/ptep/ptac097. https://pdg.lbl.gov/2022/reviews/rpp2022-rev-neutrino-mixing.pdf. Review on Neutrino Masses, Mixing, and Oscillations.

[17] B. T. Cleveland et al. Measurement of the solar electron neutrino flux with the Homestake chlorine detector. *Astrophys. J.*, 496:505–526, 1998. doi: 10.1086/305343.

[18] Q. R. Ahmad et al. Measurement of the rate of $\nu_e + d \rightarrow p + p + e^-$ interactions produced by ^{8}B solar neutrinos at the Sudbury Neutrino Observatory. *Phys. Rev. Lett.*, 87:071301, 2001. doi: 10.1103/PhysRevLett.87.071301.

[19] S. P. Mikheyev and A. Yu. Smirnov. Resonance Amplification of Oscillations in Matter and Spectroscopy of Solar Neutrinos. *Sov. J. Nucl. Phys.*, 42:913–917, 1985.

[20] L. Wolfenstein. Neutrino Oscillations in Matter. *Phys. Rev. D*, 17:2369–2374, 1978. doi: 10.1103/PhysRevD.17.2369.

[21] Y. Fukuda et al. Evidence for oscillation of atmospheric neutrinos. *Phys. Rev. Lett.*, 81: 1562–1567, 1998. doi: 10.1103/PhysRevLett.81.1562.

[22] F. P. An et al. Observation of electron-antineutrino disappearance at Daya Bay. *Phys. Rev. Lett.*, 108:171803, 2012. doi: 10.1103/PhysRevLett.108.171803.

[23] J. K. Ahn et al. Observation of Reactor Electron Antineutrino Disappearance in the RENO Experiment. *Phys. Rev. Lett.*, 108:191802, 2012. doi: 10.1103/PhysRevLett.108.191802.

[24] K. Abe et al. T2K measurements of muon neutrino and antineutrino disappearance using 3.13×10^{21} protons on target. *Phys. Rev. D*, 103(1):L011101, 2021. doi: 10.1103/PhysRevD.103.L011101.

[25] M. A. Acero et al. First Measurement of Neutrino Oscillation Parameters using Neutrinos and Antineutrinos by NOvA. *Phys. Rev. Lett.*, 123(15):151803, 2019. doi: 10.1103/PhysRevLett.123.151803.

[26] P. Adamson et al. Combined analysis of ν_μ disappearance and $\nu_\mu \rightarrow \nu_e$ appearance in MINOS using accelerator and atmospheric neutrinos. *Phys. Rev. Lett.*, 112:191801, 2014. doi: 10.1103/PhysRevLett.112.191801.

[27] M. H. Ahn et al. Measurement of Neutrino Oscillation by the K2K Experiment. *Phys. Rev. D*, 74:072003, 2006. doi: 10.1103/PhysRevD.74.072003.

[28] P. F. de Salas et al. 2020 global reassessment of the neutrino oscillation picture. *JHEP*, 02: 071, 2021. doi: 10.1007/JHEP02(2021)071.

[29] K. Abe et al. Search for Electron Antineutrino Appearance in a Long-baseline Muon Antineutrino Beam. *Phys. Rev. Lett.*, 124(16):161802, 2020. doi: 10.1103/PhysRevLett.124.161802.

[30] C. H. Llewellyn Smith. Neutrino reactions at accelerator energies. *Physics Reports*, 3(5): 261–379, 1972. ISSN 0370-1573. doi: https://doi.org/10.1016/0370-1573(72)90010-5. https://www.sciencedirect.com/science/article/pii/0370157372900105.

[31] G. P. Zeller. Low-energy neutrino cross-sections: Comparison of various Monte Carlo predictions to experimental data. In *2nd International Workshop on Neutrino-Nucleus Interactions in the Few GeV Region (NuInt 02) Irvine, California, December 12-15, 2002*, 2003.

[32] Howard Scott Budd, A. Bodek, and J. Arrington. Modeling quasielastic form-factors for electron and neutrino scattering. In *2nd International Workshop on Neutrino-Nucleus Interactions in the Few GeV Region*, 8 2003.

[33] H. S. Budd, A. Bodek, and J. Arrington. Vector and axial form-factors applied to neutrino quasielastic scattering. *Nucl. Phys. Proc. Suppl.*, 139:90–95, 2005. doi: 10.1016/j.nuclphysbps.2004.11.181. [,90(2004)].

[34] F. de M. Blaszczyk. *T2K off-axis near detector ν_μ flux measurement and absolute momentum scale calibration of the off-axis near detector tracker*. PhD thesis, Université de Paris, 2011.

[35] V Lyubushkin et al. A Study of quasi-elastic muon neutrino and antineutrino scattering in the NOMAD experiment. *Eur. Phys. J. C*, 63:355–381, 2009. doi: 10.1140/epjc/s10052-009-1113-0.

[36] A. A. Aguilar-Arevalo et al. First Measurement of the Muon Neutrino Charged Current Quasielastic Double Differential Cross Section. *Phys. Rev. D*, 81:092005, 2010. doi: 10.1103/PhysRevD.81.092005.

[37] J. A. Formaggio and G. P. Zeller. From eV to EeV: Neutrino Cross Sections Across Energy Scales. *Rev. Mod. Phys.*, 84:1307–1341, 2012. doi: 10.1103/RevModPhys.84.1307.

[38] K. Abe et al. The T2K Experiment. *Nucl. Instrum. Meth.*, A659:106–135, 2011. doi: 10.1016/j.nima.2011.06.067.

[39] K. Abe et al. Observation of Electron Neutrino Appearance in a Muon Neutrino Beam. *Phys. Rev. Lett.*, 112:061802, 2014. doi: 10.1103/PhysRevLett.112.061802.

[40] High-intensity Proton Accelerator Project Team. *Accelerator technical design report for high-intensity proton accelerator facility project, J-PARC*. CERN, 2003. URL `https://cds.cern.ch/record/747209`.

[41] S. Nagamiya. KEK/JAERI Joint Project on high-intensity proton accelerators. *Nuclear instruments & methods in physics research. Section A, Accelerators, spectrometers, detectors and associated equipment*, 503(1):34–40, 2003.

[42] A. K. Ichikawa. Design concept of the magnetic horn system for the T2K neutrino beam. *Nucl. Instrum. Meth. A*, 690:27–33, 2012. doi: 10.1016/j.nima.2012.06.045.

[43] S. van der Meer. A Directive Device for Charged Particles and Its use in an Enhanced Neutrino Beam. Technical Report CERN-61-07, CERN, 2 1961.

[44] K. Abe et al. T2K neutrino flux prediction. *Phys. Rev. D*, 87(1):012001, 2013. doi: 10.1103/PhysRevD.87.012001. [Addendum: Phys.Rev.D 87, 019902 (2013)].

[45] T. Ovsiannikova et al. The new experiment WAGASCI for water to hydrocarbon neutrino cross section measurement using the J-PARC beam. *J. Phys. Conf. Ser.*, 675(1):012030, 2016. doi: 10.1088/1742-6596/675/1/012030.

[46] G. Pintaudi. T2K-WAGASCI: First physics run of the WAGASCI-BabyMIND detector with full setup. *PoS*, LeptonPhoton2019:142, 2019. doi: 10.22323/1.367.0142.

[47] H. Oshima et al. Study of neutrino charged current interactions on iron in the NINJA experiment. *J. Phys. Conf. Ser.*, 1468(1):012128, 2020. doi: 10.1088/1742-6596/1468/1/012128.

[48] K. Abe et al. Measurement of the muon neutrino charged-current single π^+ production on hydrocarbon using the T2K off-axis near detector ND280. *Phys. Rev. D*, 101(1):012007, 2020. doi: 10.1103/PhysRevD.101.012007.

[49] K. Abe et al. Measurements of $\overline{\nu}_\mu$ and $\overline{\nu}_\mu + \nu_\mu$ charged-current cross-sections without detected pions or protons on water and hydrocarbon at a mean anti-neutrino energy of 0.86 GeV. *PTEP*, 2021(4):043C01, 2021. doi: 10.1093/ptep/ptab014.

[50] M. Antonova et al. Baby MIND: A Magnetized Segmented Neutrino Detector for the WAGASCI Experiment. *JINST*, 12(07):C07028, 2017. doi: 10.1088/1748-0221/12/07/C07028.

[51] O. Basille et al. Baby MIND Readout Electronics Architecture for Accelerator Neutrino Particle Physics Detectors Employing Silicon Photomultipliers. *JPS Conf. Proc.*, 27:011011, 2019. doi: 10.7566/JPSCP.27.011011.

[52] T. Matsubara. Application of MPPC for T2K near Detector Upgrade. *JPS Conf. Proc.*, 27: 011006, 2019. doi: 10.7566/JPSCP.27.011006.

[53] K. Matsushita. Design and Performance of MPPC-array Readout System for the WAGASCI Neutrino Detector. *JPS Conf. Proc.*, 27:012019, 2019. doi: 10.7566/JPSCP.27.012019.

[54] K. Abe et al. Observation of Electron Neutrino Appearance in a Muon Neutrino Beam. *Phys. Rev. Lett.*, 112:061802, 2014. doi: 10.1103/PhysRevLett.112.061802.

[55] A. Ferrari, P. R. Sala, A. Fasso, and J. Ranft. FLUKA: A multi-particle transport code (Program version 2005). Technical Report CERN-2005-010, SLAC-R-773, INFN-TC-05-11, CERN-2005-10, CERN, 10 2005. https://doi.org/10.2172/877507.

[56] R. Brun, F. Bruyant, M. Maire, A. C. McPherson, and P. Zanarini. GEANT3 user's manual. Technical Report CERN-DD-EE-84-1, CERN, 9 1987. https://cds.cern.ch/record/1119728.

[57] N. Abgrall et al. Measurements of $\pi^\pm$, $K^\pm$ and proton double differential yields from the surface of the T2K replica target for incoming 31 GeV/c protons with the NA61/SHINE spectrometer at the CERN SPS. *Eur. Phys. J. C*, 79(2):100, 2019. doi: 10.1140/epjc/s10052-019-6583-0.

[58] Y. Nakatsugawa et al. Silicon Carbide Target for a Muon-Electron Conversion Search at J-PARC MLF. *JPS Conf. Proc.*, 8:025013, 2015. doi: 10.7566/JPSCP.8.025013.

[59] Y. Hayato and L. Pickering. The NEUT neutrino interaction simulation program library. *Eur. Phys. J. ST*, 230(24):4469–4481, 2021. doi: 10.1140/epjs/s11734-021-00287-7.

[60] M. Casolino and P. Picozza. A Cellular automaton to filter events in high-energy physics discrete calorimeter. *Nucl. Instrum. Meth. A*, 364:516–523, 1995. doi: 10.1016/0168-9002(95)00520-X.

[61] I. Abt, I. Kisel, S. Masciocchi, and D. Emelyanov. CATS: A cellular automaton for tracking in silicon for the HERA-B vertex detector. *Nucl. Instrum. Meth. A*, 489:389–405, 2002. doi: 10.1016/S0168-9002(02)00790-8.

[62] D. E. Groom, N. V. Mokhov, and S. I. Striganov. Muon stopping power and range tables 10-MeV to 100-TeV. *Atom. Data Nucl. Data Tabl.*, 78:183–356, 2001. doi: 10.1006/adnd.2001.0861.

[63] R. L. Workman et al. Review of Particle Physics. *PTEP*, 2022:083C01, 2022. doi: 10.1093/ptep/ptac097. https://pdg.lbl.gov/2022/reviews/rpp2022-rev-passage-particles-matter.pdf. Review on Passage of Particles through Matter.

[64] T. Adye. Unfolding algorithms and tests using RooUnfold. In *PHYSTAT 2011*, pages 313–318, Geneva, 2011. CERN. doi: 10.5170/CERN-2011-006.313.

[65] G. D'Agostini. A Multidimensional unfolding method based on Bayes' theorem. *Nucl. Instrum. Meth. A*, 362:487–498, 1995. doi: 10.1016/0168-9002(95)00274-X.